

Synthesis of Sulfide-based Solid Electrolytes for Application to All-Solid-State Lithium-Sulfur Batteries

by

Diane Houtarde

A thesis

presented to the University of Waterloo

in fulfillment of the

thesis requirement for the degree of

Master of Applied Science

in

Electrical and Computer Engineering-Nanotechnology

Waterloo, Ontario, Canada, 2015

© Diane Houtarde 2015

AUTHOR'S DECLARATION

I hereby declare that I am the sole author of this thesis. This is a true copy of the thesis, including any required final revisions, as accepted by my examiners.

I understand that my thesis may be made electronically available to the public.

Diane Houtarde

ABSTRACT

Lithium–sulfur batteries are a promising candidate to support the demand for high energy density storage systems. The active material is sulfur, which presents the advantages of being abundant on earth, thus inexpensive, and environmentally friendly. However the use of conventional organic liquid electrolytes in these batteries prevents them from being commercialized, because of many technical problems that have yet to be overcome. One of the major issues is the polysulfide shuttle which leads to fast decay of cell performance. A solution is to use all-solid-state batteries instead, thus removing the inherent hazards to liquid batteries such as flammability and leakages. The drawbacks for all-solid-state are the increase in resistance of the electrolytes, the deterioration of the electronic and ionic pathways at the solid/solid interfaces, and the expensive processes and designs for their manufacture. In this thesis, research is carried out in an attempt to find new superionic conductors for solid electrolytes, improve on known conductors, and investigate the performance of all-solid-state cells using different fabrication methods and morphologies.

In the first part of this thesis, the parameters influencing the synthesis of the well-known super-ionic conductor $\text{Li}_7\text{P}_3\text{S}_{11}$ are studied, in order to establish a more systematic method to produce this metastable phase at larger scales. Then, new crystal structures are uncovered in the $67.\text{Na}_2\text{S}-33.\text{P}_2\text{S}_5$ glass system. After thermal and spectroscopic analyses, it seems that these phases might be polymorphs of the known phase $\text{Na}_4\text{P}_2\text{S}_7$, although its crystal structure has never been reported before. Finally, a completely new phase, Li_2NaPS_4 , is synthesized and characterized by XRD, Raman spectroscopy, and electrochemical impedance spectroscopy.

In the second part, the performance of all-solid-state batteries is analyzed depending on the solid electrolyte used, and the composition and architecture of the composite cathode. First, two batteries are compared- using $\text{Li}_7\text{P}_3\text{S}_{11}$ and $\text{Li}_{10}\text{GeP}_2\text{S}_{12}$ (LGPS) solid electrolyte respectively. The $\text{Li}_{10}\text{GeP}_2\text{S}_{12}$ -based cell proved superior capacity, but poor cyclability and rate capability, and investigation showed that the material decomposes in side reactions providing extra capacity. Then in the composite cathode, two different carbons, Activated Carbon (AC) and KetjenBlack (KB), and two different ionic conductors, $\text{Li}_{1.5}\text{PS}_{3.25}$ and LGPS, are compared with each other respectively. At low cycling rate, the best performance is obtained for materials which achieve higher contact area (higher surface area for carbon: AC, and higher coating and ductility for solid electrolyte: $\text{Li}_{1.5}\text{PS}_{3.25}$).

However, for high rates and high rate change, conductivities are the most important characteristic to enable fast transfer of the carriers at the interface of the active material. Thus, better performance was observed for KB for the electronic conductors, and for LGPS for the ionic conductors.

ACKNOWLEDGEMENTS

I would like to express my sincere gratitude and appreciation to my supervisor Professor Linda F. Nazar, for her support, and for her guidance and instructions throughout my research project. Thanks to my other supervisor Professor William Wong in the ECE department, for accepting to co-supervise me and for his cooperation during the completion of my program.

I would like to thank all the sulfur group members with whom I participated in interesting and rewarding discussions: Dr Marine Cuisinier, Dr Xiao Liang, Connor Hart, Quan Pang, Takuto Kwok, and Erika Ramos. Special thanks and acknowledgements to my co-op students Kavish Kaup and Sarah McCaugherty for their help in the execution of my research work.

I would like to thank the research group members who have supported me in my experiments with generosity and kindness and who have made this experience more enjoyable: Particular thanks to Dr. Guerman Popov, Dr. Victor Duffort, and Dr. Dipan Kundu. Also thank you Dr. Momo Safari, Dr. Jaka Sunarso, Dr. Chun Xia, Dr. Shahrzad Vajargah, Elahe Pashiri, Robert Black, Xiaoqi Sun, Abhi Shyamsunder, Russel Fernandes, Parvin Adeli, Yverick Rangom, Brian Adams, He Huang, Meng Xu, and Niranjana Sudhakar.

I would like to thank Pr. Holger Kleinke and his student Nader Farahi for granting me and my students the access to his pulverisette 7 Fritsch when ours broke down. Thanks to Ralph Dickhout who has provided help and good humor when I needed to use the Differential Scanning Calorimetry instrument.

TABLE OF CONTENTS

List of figures	ix
List of tables	xi
Glossary.....	xii
1. Chapter 1 : Introduction.....	1
1.1 General overview on lithium rechargeable batteries	1
1.2 Lithium-Sulfur batteries	4
1.3 All-solid-state-batteries	7
1.4 Summary	16
1.5 Scope of this thesis	17
2. Chapter 2: Characterization methods and techniques	18
2.1 Powder X-Ray Diffraction	18
2.2 Thermogravimetric Analysis and Differential Scanning Calorimetry.....	20
2.3 Surface Area/pore size characterization	22
2.4 Scanning Electron Microscopy and Energy Dispersive X-ray Spectroscopy.....	22
2.5 Raman Spectroscopy	23
2.6 Electrochemical measurements	23
2.6.1 Solid-state cell design.....	23
2.6.2 Galvanostatic Cycling.....	25
2.6.3 Cyclic Voltammetry	25
2.6.3 Electrochemical Impedance Spectroscopy	25
3. Chapter 3: Synthesis and characterization of sulfide-based Solid Electrolytes.....	27

3.1 Introduction	27
3.2 $\text{Li}_2\text{S-P}_2\text{S}_5$ glasses	27
3.2.1 Synthesis of $\text{Li}_7\text{P}_3\text{S}_{11}$	28
3.2.2 Influence of synthesis parameters.....	29
3.2.3 Electrochemical characterization of $\text{Li}_7\text{P}_3\text{S}_{11}$	39
3.2.4 Conclusion and perspectives	42
3.3 $\text{Na}_2\text{S-P}_2\text{S}_5$ glasses	43
3.3.1 Introduction	43
3.3.2 70. Na_2S -30. P_2S_5 glasses	43
3.3.3 67. Na_2S -33. P_2S_5 glasses	46
3.3.4 Characterization of the unknown phases	51
3.3.5 Conclusions and perspectives.....	52
3.4 Na-Li hybrid glasses.....	54
3.4.1 Experimental.....	54
3.4.2 Results and discussion.....	54
3.4.3 Characterization of the unknown “phase A”	57
3.4.4 Conclusion and perspectives	60
3.5 Conclusions and perspectives	62
4. Chapter 4 : Applications to All-Solid-State-Batteries	64
4.1 Introduction	64
4.2 Experimental.....	65
4.3 Results and discussion.....	66
4.3.1 Comparison of solid electrolytes	66

4.3.2 Study of the cathode composition.....	71
4.4 Conclusions and perspectives.....	82
References	85

List of figures

Figure 1: Schema of the typical charge/discharge mechanisms in Li-S battery ⁴	5
Figure 2: Schematic diagram of (a) a thin film-type battery and (b) a bulk-type battery.	8
Figure 3: Comparison of activation energies for Li ₂ S-P ₂ S ₅ glasses and conventional liquid electrolytes. 12	
Figure 4: Charge-discharge curves of Li-In/Li ₄ Ti ₅ O ₁₂ all-solid-state cell. Open and solid circles overlap each other and represent charge and discharge capacities. Solid diamonds represent the Coulombic efficiency (Tatsumisago et al. 2011) ⁴⁶	13
Figure 5: Charge-discharge performance of (a) an all-solid-state cell [AB-S-SE/80Li ₂ S-20P ₂ S ₅ (SE) /Li-In] and (b) a LiCoO ₂ -based all-solid-state cell for comparison. The inset shows the cycle performance of the sulfur-based cell (Hayashi et al. ⁴⁷).	14
Figure 6: Different approaches to realize intimate contact between composites in the electrodes.	15
Figure 7: schematic illustration of Bragg's law.....	19
Figure 8: Schematic of a DSC instrument.	20
Figure 9: Features of a DSC curve.	21
Figure 10: Schematic illustration of an all-solid-state battery.....	24
Figure 11: Illustration of an all-solid-state battery cell.	24
Figure 12: Typical Nyquist plot of impedance measurement on a solid electrolyte.	26
Figure 13: XRD patterns of glasses milled at 400 rpm for 22 hours and of glasses milled at 900 rpm for 30 min.....	30
Figure 14: DSCs of Li ₂ S-P ₂ S ₅ glasses after milling at 900 rpm for 30 min and at 400 rpm for 22 h respectively.....	31
Figure 15: XRD patterns of 70-30 Li ₂ S-P ₂ S ₅ glasses after heat-treatment at 250°C, performed with identical conditions.....	32
Figure 16: XRD patterns of high-speed milled glasses after heat-treatment at 300°C (a) and at 330°C(c), and on low-speed milled glasses after heat-treatment at 325°C (b).	33
Figure 17: XRD patterns of identical samples that have been heat-treated at 250°C for different holding times.	34
Figure 18: XRD patterns of heat-treated glasses with (1) a slow heating rate and fast cooling rate, (2) a fast heating rate and a slow cooling rate, and (3) fast heating and cooling rates.	35
Figure 19: XRD patterns of samples after heat-treatment of 50 mg and 200 mg of glasses.....	36
Figure 20: XRD patterns of heat-treatments performed on (a) a powder sample and (b) a pelletized sample.....	37
Figure 21: XRD patterns of heat-treated glasses in (a) an inconel crucible and (b) a gold crucible.	38
Figure 22: XRD patterns of (a) 70.Li ₂ S-30.P ₂ S ₅ milled glasses, and of Li ₇ P ₃ S ₁₁ crystallized in a (b) powder-form, and (c) pellet-form.....	40
Figure 23: Nyquist plots of (a) Li ₂ S-P ₂ S ₅ glasses, (b) Li ₇ P ₃ S ₁₁ prepared in a powder-form and (c) Li ₇ P ₃ S ₁₁ prepared in a pellet form, measured at room temperature.	41
Figure 24: XRD patterns of 70-30 Na ₂ S-P ₂ S ₅ glasses milled at 400 rpm for 10 hours and 30 min respectively.....	44
Figure 25: DSC curve of the 70-30 Na ₂ S-P ₂ S ₅ glasses milled at 400 rpm for 30 min.	45

Figure 26: XRD patterns of 70. Na ₂ S-30.P ₂ S ₅ glasses heat-treated and quenched at 210°C, 250°C and 390°C respectively.	46
Figure 27: DSC curves of 67.Na ₂ S-33.P ₂ S ₅ glasses milled at 400 rpm.	47
Figure 28: XRD patterns of 67-33 glasses after heat-treatment at (a) 230°C, (b) 290°C, (c) 375°C, (d) 455°C, and (e) 470-300°C.	48
Figure 29: Raman spectra of the 67-33 Na glasses after heat-treatment at 375°C, 455°C, and 470-300°C.	49
Figure 30: LeBail fit of the XRD pattern of the unknown phase 1.	52
Figure 31: LeBail fit of the XRD pattern of the unknown phase 2.	52
Figure 32 : XRD patterns of Li ₇ P ₃ S ₁₁ glass-ceramics (Li gl), 70.Na ₂ S-30.P ₂ S ₅ glasses (Na gl), and mixtures of both in 90:10, 60:40, 50:50, and 40:60 weight ratios.	55
Figure 33 DSC of Li ₇ P ₃ S ₁₁ glass-ceramics, 70.Na ₂ S-30.P ₂ S ₅ glasses (Na gl), and mixtures of both in 90:10, 60:40, 50:50, and 40:60 weight ratios.	56
Figure 34 XRD patterns of the hybrid 60:40 Na-Li glasses heat-treated at 260°C, 330°C, and 375°C. ...	57
Figure 35: Polyhedral depiction of the unit cell of the Li ₂ NaPS ₄ structure. Purple tetrahedra: PS ₄ , yellow tetrahedra: NaS ₄ , green tetrahedra: LiS ₄	58
Figure 36: Space group and cell parameters of the Li ₂ NaPS ₄ structure.	59
Figure 37: Nyquist plot of Li ₂ NaPS ₄	60
Figure 38: SEM image and EDX analysis of Li ₂ NaPS ₄	61
Figure 39: Raman spectrum of Li ₂ NaPS ₄	62
Figure 40: Charge-discharge curves of (a) Li ₇ P ₃ S ₁₁ -based and (b) LGPS-based all-solid-state cells.	68
Figure 41: Cyclic voltammogram of (a) LGPS and (b) Li ₇ P ₃ S ₁₁ against Li-In at the first cycle.	69
Figure 42: Charge-discharge curves of a (SP-Li _{1.5} PS _{3.25})/(Li ₁₀ GeP ₂ S ₁₂)/(Li-In) cell.	70
Figure 43: XRD patterns of mechanically milled Ketjenblack-sulfur (KB-S) and Activated Carbon-sulfur (AC-S) composites.	73
Figure 44: XRD patterns of milled and annealed Ketjenblack-sulfur (KB-S) and Activated Carbon-sulfur (AC-S) composites.	73
Figure 45: XRD patterns of mechanically milled KB/S/Li _{1.5} PS _{3.25} and AC/S/Li _{1.5} PS _{3.25} composites.	73
Figure 46: TG curves of (a) KB-S composites and (b) AC-S composites, prepared by mechanical milling, and milling-annealing respectively.	75
Figure 47: TG curves of KB/S/Li _{1.5} PS _{3.25} and AC/S/Li _{1.5} PS _{3.25} composite cathodes.	76
Figure 48: DTA curves of (a) milled KB-S, (b) milled-annealed KB-S, (c) milled AC-S, (d) milled-annealed AC-S, (e) KB/S/Li _{1.5} PS _{3.25} , (f) AC/S/Li _{1.5} PS _{3.25} composites, and (g) Li _{1.5} PS _{3.25}	77
Figure 49: Charge-discharge voltage profile of an all-solid-state cell with an AC/S/Li _{1.5} PS _{3.25} cathode.	79
Figure 50: Specific discharge capacity in function of cycle number at different cycling rates for the KB-based cell and the AC-based cell.	80
Figure 51: XRD patterns of AC/S/Li _{1.5} PS _{3.25} and AC/S/Li ₁₀ GeP ₂ S ₁₂ composite cathodes.	81
Figure 52: Charge-discharge curves of cells prepared with (a) Li _{1.5} PS _{3.25} -based and (b) LGPS-based cathodes.	82

List of Tables

Table 1: Ionic conductivities at 25 °C of various inorganic solid electrolytes. Sulfide-based electrolytes are highlighted.	9
Table 2: Ionic conductivity of $\text{Li}_2\text{S-P}_2\text{S}_5$ glasses and glass-ceramics.	41
Table 3: Comparison of peaks frequencies and intensities of the Raman spectra of the heat-treated materials. w weak, m: medium, s: strong, v: very, b: broad, sh: shoulder, n.p. : not present.	50
Table 4: Comparison of the ionic conductivity of different sodium glasses and glass-ceramics	51
Table 5: Fitting parameters of the equivalent circuit.	60
Table 6: Ionic conductivities at room temperature of $\text{Li}_7\text{P}_3\text{S}_{11}$ and LGPS, in literature and as-used in all-solid-state cells.	67
Table 7: BET analysis of the different carbon composites.	78
Table 8: Ionic conductivities of $\text{Li}_{1.5}\text{PS}_{3.25}$ and LGPS.	81

Glossary

AC	Alternating current / Activated Carbon
BET	Brunauer-Emmett-Teller
CV	Cyclic voltammetry
DSC	Differential scanning calorimetry
EDX	Energy Dispersive X-ray spectroscopy
EIS	Electrochemical impedance spectroscopy
KB	KetjenBlack
Li-S	Lithium-sulfur
LISICON	LI SuperIonic CONductor
NASICON	NA SuperIonic CONductor
SEM	Scanning electron microscopy
TGA	Thermogravimetric analysis
XRD	X-ray diffraction

Chapter 1:

Introduction

1.1 General overview on lithium rechargeable batteries

With the development of the world's population, the economic growth, and the advances in technologies, the global demand for energy is increasing at an alarming rate. These energy needs can no longer rely on the burning of fossil fuels as the resulting emissions create serious environmental pollution and contribute to global warming. It is therefore essential to turn down our dependence on fossil fuels, which are besides unevenly distributed and becoming scarce, and to develop profitable and efficient renewable energies ¹.

Energies based on solar, wind, geothermal and nuclear sources were shown to be promising clean alternatives. However, these energies are not reliable, efficient and competitive enough to meet the industrial demand for high-energy density and storage capacity needed in electric devices and automobile motors at a large scale. Furthermore, they present the disadvantage of being stationary when the world is furiously calling for wireless technologies. Rechargeable batteries are the obvious solution since they provide storage of chemical energy in a portable device delivering energy as electrical energy with a very high conversion efficiency. However, several limitations such as cost, power, cycle life, safety and environmental friendliness have to be considered. Lithium-ion batteries in particular have invaded our laptops, cell-phones and portable telecom technologies, because they are low-cost, compact, and environmentally harmless. Yet these batteries are not suitable to meet the vehicle energy requirements, such as safety, rate capability and sufficient energy density to power an electric vehicle on a long run. Currently, lead-acid batteries are commonly used for hybrid gas-electric cars on the market, but do not provide enough power to be used without fossil fuels, and are toxic for the environment ².

1.1.1 Basic Concepts of Lithium rechargeable batteries

As seen before, the most promising candidate for applications to the auto industry is the Lithium-ion rechargeable battery. A rechargeable battery, also known as secondary battery, is able to be charged and discharged reversibly with the same capacity over a certain life-time. They are thus

much more efficient than primary batteries which are for one-time uses only, e.g. alkaline batteries found all over the consumer market. Typically, a practical rechargeable battery consists of several connected electrochemical cells in series and in parallel to meet the output requirements in voltage and current for a given application ³. That is why all of the research made for the development of these batteries are focused on the functioning and performance of a single electrochemical cell.

An electrochemical cell is composed of a positive (cathode) and a negative (anode) electrodes separated by an electronically insulating electrolyte, which can be liquid or solid. When in discharge, the two electrodes are connected via an exterior electric circuit, the difference in chemical potentials between the two active materials gives rise to the conduction of ions through the electrolyte, and oxidation and reduction half-reactions take place at the anode and cathode respectively. When the cell is charged, the reactions at the electrodes are reversed: oxidation occurs at the cathode and reduction at the anode. So that the transfer of electrons and ions occurs in the electrodes, both of them should be ionically and electronically conductive.

Several basic electrochemical concepts are needed to characterize the performance of an electrochemical cell. The next part will focus on defining them as they are going to be used in this thesis ⁴.

- The Potential (V) of a cell is determined by the redox potentials of the reactions occurring at the electrodes, which are defined by thermodynamics laws and intrinsic to each active material. The potential difference between cathode and anode is desired to be large as the output power is the product of the current by the voltage. Thus, the electrolyte has to be chosen carefully to be stable in the electrochemical potential window of the cell, to prevent its decomposition.
- The Discharge/Charge Voltage Profile is a plot of voltage as a function of specific capacity upon galvanostatic cycling, where a constant discharge/charge current is applied to the cell. In liquid batteries the profile will typically show intermediary redox reactions and the potential they correspond to. For instance a plateau represents a two-phase transition and a slope indicates a single-phase reaction. A minimum voltage difference between discharge and charge is wanted to maximize the energy efficiency, as it is characteristic of a low degree of polarization.
- The Specific Capacity (in mA.h/g) or volumetric capacity (in mA.h/cm³) is defined by the amount of charge (Q, in mA h) stored per mass or volume of electrode for one full

discharge/charge. In industry, batteries are more generally evaluated in terms of energy density, which is the product of capacity and voltage per mass (W.h/kg) or volume (W.h/L).

- The Capacity Retention characterizes the ability of the cell to get a reversible specific discharge/charge capacity over a defined number of cycles. It is usually expressed as a fraction or percentage of the 1st cycle, which is typically the highest in specific capacity achieved.
- Similarly, the Cycling Life means the capacity retention with prolonged life of a cell. This characteristic is critical for practical applications, but unfortunately it depends on many factors that are not always easily reproducible in laboratory experiments (e.g. rate changes, rest times and frequencies). In the lab, the cell is considered to have reached its cycle life, when upon galvanostatic cycling, the capacity has dropped to 80% of its initial capacity. High rate capability indicates the ability to maintain its capacity and degree of polarization upon increased rate.
- The Coulombic Efficiency, expressed in %, is the ratio of the discharge specific capacity to the charge specific capacity of the same cycle. It provides an interesting analysis over the number of cycles for prolonged galvanostatic cycling of a cell.

1.1.2 Intercalation and integration electrochemistry

Li metal as an anode in rechargeable batteries has attracted much interest due to the fact that it is the lightest (specific gravity = 0.53 g.cm⁻³) and most electropositive element of the periodic table after hydrogen. These properties are essential for the development of high energy density and high specific capacity devices.

There are two types of lithium battery systems, those that are based on intercalation electrochemistry, with electrodes that store/release Li⁺ ions through a topotactic intercalation process, and those based on integration electrochemistry, with cathodes in which Li⁺ ions react in a reversible way with the active material, enabling larger storage of the active species.

The first Li-ion batteries commercialized by SONY Corporation were composed of the layered structure of LiCoO₂ as a cathode (an intercalation-based active material discovered by Goodenough et al. in 1980⁵) and graphite as an anode, and they are still dominating the electronic device market. More recently, LiFePO₄ has proven to be more stable, thanks to the presence of PO₄³⁻ tetrahedra in its structure, and above all to render higher specific capacity (170 mA.h/g against 140

mA.h/g for LiCoO₂). Although the LiFePO₄-based batteries exhibit extremely small capacity decay even after thousands of cycles, their application to industry in a wide scale has been curbed since LiFePO₄ has a much lower electronic conductivity and thus requires more nanotechnology and coatings treatments prior to battery assembly.

Traditional Li ion batteries have enabled to keep up and contribute to the explosive development of portable electronic technologies, like cell-phones, computers and cameras. However, after several decades of research and practical optimization, these energy devices have reached their limits and cannot respond to the higher energy density demanded for electric vehicles. The physical storage capacity of intercalation-based mechanisms are too limited, and the electrochemical-stability windows of most electrolytes do not allow cycling of these batteries on a wider voltage window to get more storage capacity. Therefore, alternative materials that undergo an integration process by accommodating ions and electrons in electrode redox reactions are promising candidates to be the next energy source of the future. Two examples of this approach are Li-O₂ and Li-S batteries. Both systems are based on redox reactions between chalcogens and oxygen or sulfur, but although the latter are in the same group, the chemistries are very different.

Lithium-oxygen batteries using diatomic oxygen as the active cathode material were discovered most recently and have a remarkable theoretical specific energy of 900 Wh kg⁻¹. Upon discharge, the lithium anode is oxidized and releases Li⁺ ions in the liquid electrolyte, and through the carbon positive electrode, atmospheric O₂ is diffused and dissolved in the liquid electrolyte where the reduction reaction takes place following the equation: $2\text{Li}^+ + \text{O}_2 + 2\text{e}^- \leftrightarrow \text{Li}_2\text{O}_2$. This novel system presents some major drawbacks such as irreversible side reactions of the intermediate O²⁻ anion, causing very fast capacity decay, and the electrochemistry and mechanisms need further investigation and understanding in order to design functional working electrodes ⁶.

This thesis examines the electrochemistry of Li-S batteries, which will be discussed in detail in the following section.

1.2 Lithium-sulfur batteries

1.2.1 Basic principles of Li-S batteries

The Li-S battery system has a theoretical specific capacity of 1672 mA.h/g, which is about 6 times the capacity of conventional Li-ion batteries. Moreover, sulfur presents the advantage of being

environmentally friendly and one of the most abundant elements on earth, making it a very inexpensive material.

A traditional Li-S cell consists of a lithium metal anode and a sulfur-composite positive electrode separated by an organic liquid electrolyte. During discharge, the lithium metal is oxidized and releases Li^+ ions and electrons. The electrons are transferred to the cathode via the external electrical circuit, which generates a current. The Li^+ ions are transferred from the anode to the cathode through the ionically conductive. At the positive electrode elemental sulfur (in the form of cyclo- S_8 molecules) is reduced, following the overall reaction equation $\text{S}_8 + 16\text{e}^- + 16\text{Li}^+ \leftrightarrow 8\text{Li}_2\text{S}$. Lithium sulfide is the final product after the formation and subsequent reaction of intermediate lithium polysulfide species⁷. The reverse reactions occur when the cell is charged. **Figure 1** illustrates the behavior of each species upon functioning of the cell.

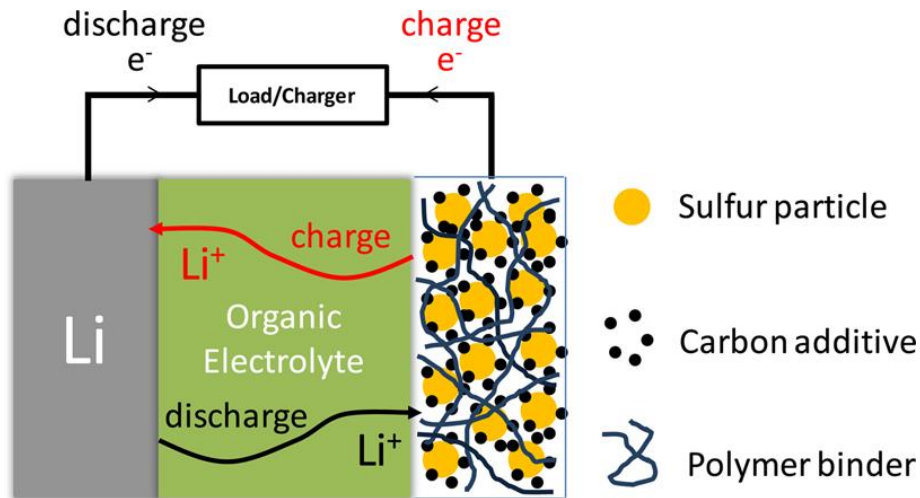


Figure 1: Schema of the typical charge/discharge mechanisms in Li-S battery⁴.

1.2.2 Challenges of Li-S batteries

Despite being the center of intensive research since the early 1950's, Li-S battery technology still faces many technical problems that prevent its commercialization. Alternative anode materials need to be investigated to resolve safety issues associated with the reactivity of a pure lithium metal anode. Additionally, Li-S batteries generally show short cycle life, low rate capability, and low Coulombic efficiency. The fundamental problems causing this poor performance can be divided into three categories: the physical properties of sulfur and its species, lithium deposition, and polysulfide solubility and shuttle.

1.2.2.1 Physical properties of S₈/Li₂S

At the positive electrode where reduction occurs, sulfur reacts with electrons from the external circuit, and with Li⁺ ions transferred from the lithium anode through the electrolyte. However, sulfur possesses very low ionic and electronic conductivities (5×10^{-30} S/cm and 10^{-17} S/cm respectively)⁸, so the transfer of the charged species is very difficult. This results in poor activation and use of the sulfur, and thus in poor battery performance. To overcome this problem carbon additives are used as hosts due to their very high electronic conductivity and light weight¹⁰, yet the overall energy density is consequently reduced. The same problem applies to other sulfur species, products from the discharge reaction, so when Li₂S is deposited on the cathode surface, the conversion back to sulfur might be even more difficult and the polarization increasingly larger upon cycling. Another important issue is the volumetric expansion/contraction occurring during the transformation of sulfur (density = 2.03 g.cm⁻³) into lithium sulfide (density = 1.67 g.cm⁻³) and vice versa. This 80% change in volume can seriously deteriorate the structural integrity of the cathode, leading to fast capacity fading⁹. This problem is usually alleviated by the use of a binder, at the expense of the overall energy density.

1.2.2.2 Lithium anode issues

Lithium metal reacts violently with water or oxygen. Despite this reactivity it is still used in current state-of-the-art Li-S devices, limiting their commercialization at an industrial level. In particular, the application of current Li-S batteries to vehicle technology is very unsafe. In the circumstance of a collision the battery may explode or burst into flames. Novel anode materials to couple with sulfur composite cathodes with high energy density are needed to push the technology forward towards realistic applications. In addition, there is dendrite formation at the anode surface when lithium is deposited during the cell charge. This may give rise to growth of lithium metal through the electrolyte and the separator, causing short-circuit when it reaches the cathode⁶. This significantly reduces cycle life. For future laboratory research and industrial applications the lithium metal anode needs to either be protected, or replaced by a material without these inherent problems.

1.2.2.3 Polysulfides shuttle

One of the biggest issues with current Li-S batteries is the lithium polysulfides (LiPS) shuttle. It arises from the dissolution of intermediate polysulfide species Li₂S_n (n ≥ 2) in liquid electrolytes. The polysulfides are readily soluble in glyme-based electrolytes due to their long hydrophilic chain,

and are able to diffuse through the separator to reach the anode. The LiPS are reduced at the anode, forming a solid interface layer of $\text{Li}_2\text{S}/\text{Li}_2\text{S}_2$ which then blocks the transfer of lithium ions to the liquid electrolyte. As a result, when more incoming long-chain polysulfides reach the anode, they react with the solid interface layer, becoming short-chain LiPS. In high concentrations the short-chain LiPS diffuse back towards the cathode and become oxidized back to long-chain LiPS. This parasitic process causes self-discharge and loss of active material, resulting in poor capacity retention over cycling⁴. A lot of research has been performed on cathode materials and cathode architecture, and on electrolytes in order to chemically or physically trap these polysulfides. The search for the perfect host is still ongoing, but these studies are not in the scope of this thesis. Instead, a completely novel approach using solid electrolytes will be discussed.

1.3 All-solid-state batteries

1.3.1 Basic concepts in all-solid-state batteries

As seen previously, conventional lithium liquid batteries, although widely used and extensively studied, have major drawbacks, such as leakage risks, flammability, and expensive sealing agents, that prevent them from being commercialized or applied to electric vehicles in an industrial range. The use of all-solid-state batteries avoids these issues¹⁰. Furthermore, the weight and volume of a solid battery can easily be reduced, and thus larger energy outputs and better efficiencies can be achieved. With the development of microelectronics and integrated circuits, the demand for long cycle life, light-weight, and high energy density batteries is increasing. All-solid-state batteries are good candidates to fulfill these needs¹¹. Currently, lithium solid-state batteries still face issues such as lower power density and higher ionic resistance compared with liquid cells (at room temperature), in addition to expensive fabrication costs¹².

A solid-state cell consists of an anode and a cathode, as for a liquid electrolyte battery, but it employs a solid electrolyte. Such a substitution allows for simplified architectures of the electrodes¹³, however it has its own sets of constraints inherent to solid-state. Solid-state batteries usually have a higher resistance at ambient temperature than liquid cells, due to lower ionic conductivities of solid electrolytes. Solid cells tend to last longer because they are not as sensitive to shocks, leakages, and extreme temperatures as liquid cells. However, they undergo additional stresses at solid-solid interfaces between the electrodes and electrolyte, or even within the composite cathode itself, which can reduce performance and longevity¹⁴. The main difference in the design of the solid cells lies in

the cathodes which are typically composed of active material (e.g. metal oxides such as LiCoO_2 for lithium ion batteries), with an ionic conductor (solid electrolyte) and an electronic conductor (typically carbon when using an insulating active material) ¹⁴⁻¹⁵.

There are two types of solid state batteries: thin film type (**Figure 2a**) and bulk-type (**Figure 2b**). The main difference between the two categories comes down to the thickness of the electrolyte; in thin film batteries, the thickness is a few hundreds of nanometers, whereas in bulk-type solid state batteries it is several hundreds of micrometers. Correspondingly different processes are used to manufacture each type. Thin film solid-state electrolytes are usually fabricated by nanotechnology processes such as pulsed laser deposition, plasma sintering, chemical vapor deposition,... Bulk solid-state electrolytes are prepared by mechanical milling, annealing, compaction and heat-treating. Thin film batteries are mainly used in microelectronics for portable devices. Bulk-types are more promising for vehicles applications as they can be stacked, used in series, and provide significantly higher power and energy density. This thesis focuses on bulk-type batteries.

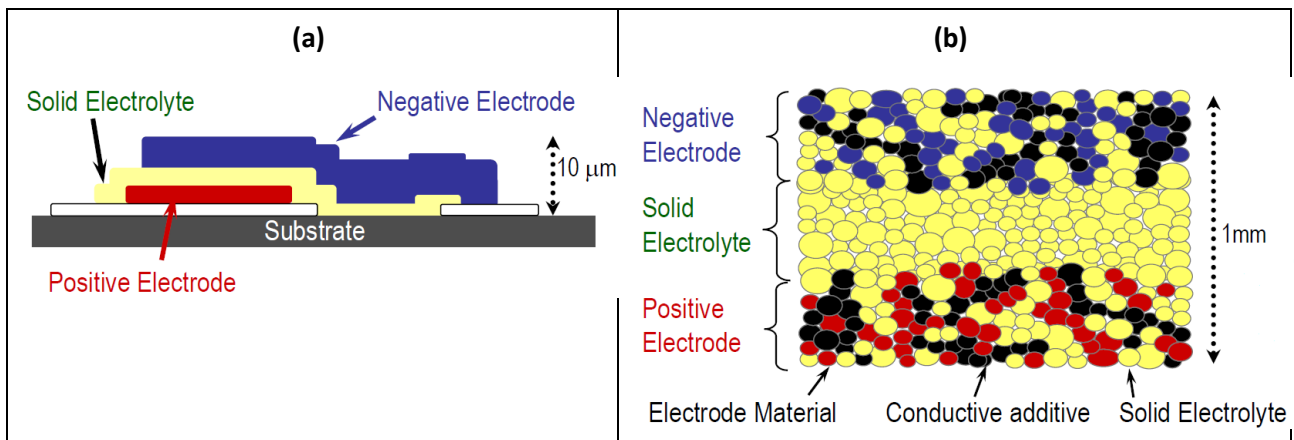


Figure 2: Schematic diagram of (a) a thin film-type battery and (b) a bulk-type battery.

For years, the potential supplantation of Li-ion technology by all-solid-state batteries has relied on finding a solid electrolyte which has high ionic conductivity, very low electronic conductivity, good chemical and thermal stability and a wide electrochemical window ¹⁶. Thus, intensive research has been carried out in the hunt for suitable solid electrolytes.

1.3.1 Development of superionicconducting solid electrolytes

Solid ionic conductors for battery applications include a large variety of materials such as gel, organic polymer, organic–inorganic hybrids, and inorganic materials. In this overview, the focus is on inorganic solid electrolytes which can be divided into three categories: crystalline, glass, and glass–ceramic. **Table 1** shows the ionic conductivities of some of the most common inorganic solid electrolytes, at room temperature.

Composition	Conductivity at 25°C (S/cm)	Category	Reference
$\text{La}_{0.51}\text{Li}_{0.34}\text{TiO}_{2.94}$ (LTT)	1.4×10^{-3}	Crystal (perovskite)	Ito et al. ¹⁷
$\text{Li}_{1.3}\text{Al}_{0.3}\text{Ti}_{1.7}(\text{PO}_4)_3$	7×10^{-4}	Crystal (NASICON)	Aono et al. ¹⁸
$\text{Li}_{14}\text{ZnGe}_4\text{O}_{16}$	1×10^{-6}	Crystal (LISICON)	Hong et al. ¹⁹
$\text{Li}_{3.4}\text{Si}_{0.4}\text{P}_{0.6}\text{S}_4$	6.4×10^{-4}	Crystal (thio-LISICON)	Kanno et al. ²⁰
$\text{Li}_{3.25}\text{Ge}_{0.25}\text{P}_{0.75}\text{S}_4$	2.2×10^{-3}	Crystal (thio-LISICON)	Kanno et al. ²¹
$\text{Li}_7\text{La}_3\text{Zr}_2\text{O}_{12}$	3×10^{-4}	Crystal (garnet)	Murugan et al. ²²
$\text{Li}_{10}\text{GeP}_2\text{S}_{12}$ (LGPS)	1.2×10^{-2}	Crystal	Kamaya et al. ³¹
$\text{Li}_{1.07}\text{Al}_{0.69}\text{Ti}_{1.46}(\text{PO}_4)_3$ (LATP)	1.3×10^{-3}	Glass-ceramic	Fu et al. ²³⁻²⁴
$\text{Li}_{1.5}\text{Al}_{0.5}\text{Ge}_{1.5}(\text{PO}_4)_3$ (LAGP)	4.0×10^{-4}	Glass-ceramic	Fu et al. ²³⁻²⁴
$\text{Li}_7\text{P}_3\text{S}_{11}$	1.1×10^{-2}	Glass-ceramic	Seino et al. ²⁵
$\text{Li}_{3.25}\text{P}_{0.95}\text{S}_4$	1.3×10^{-3}	Glass-ceramic	Mizuno et al. ⁴¹
$\text{Li}_{2.9}\text{PO}_{3.3}\text{N}_{0.46}$	3.3×10^{-6}	Amorphous (thin film)	Yu et al. ³⁴
$\text{Li}_{3.6}\text{Si}_{0.6}\text{P}_{0.4}\text{O}_4$	5.0×10^{-6}	Amorphous (thin film)	Kanehori et al. ²⁶
$30\text{Li}_2\text{S} \cdot 26\text{B}_2\text{S}_3 \cdot 44\text{LiI}$	1.7×10^{-3}	Glass	Wada et al. ³⁸
$50\text{Li}_2\text{S} \cdot 17\text{P}_2\text{S}_5 \cdot 33\text{LiBH}_4$	1.6×10^{-3}	Glass	Yamauchi et al. ³⁹
$63\text{Li}_2\text{S} \cdot 36\text{SiS}_2 \cdot 1\text{Li}_3\text{PO}_4$	1.5×10^{-3}	Glass	Aotani et al. ⁴⁰
$70\text{Li}_2\text{S} \cdot 30\text{P}_2\text{S}_5$	1.6×10^{-4}	Glass	Zhang et al. ³⁶

Table 1: Ionic conductivities at 25 °C of various inorganic solid electrolytes. Sulfide-based electrolytes are highlighted.

1.3.1.1 Inorganic crystalline ceramics electrolytes

Ceramics are typically oxides and are characterized by a high hardness and good stability in air. Four different kinds of superionic conducting oxide (SCO) electrolytes can be identified, according to their structure type.

The perovskite $\text{Li}_{0.5-3x}\text{La}_{0.5+x}\text{TiO}_3$ (LLT) materials have a high number of vacancies in the lithium lattice, resulting in a high bulk conductivity ($>10^{-3}$ S/cm for $x\sim 0.3$)²⁷. However grain boundary resistance is very high and increases the total resistance by two orders of magnitude²⁸ and high-temperature sintering is necessary for practical use. Furthermore, Ti is easily reduced by lithium metal, so these electrolytes are not applicable to lithium batteries.

The NASICON (Na SuperIonic CONductor) structures are of the type $\text{NaA}_2^{\text{IV}}(\text{PO}_4)_3$ with $\text{A}^{\text{IV}}=\text{Ge}$, Zr, or Ti. Among them, $\text{Li}_{1+x}\text{Al}_x\text{Ti}_{2-x}(\text{PO}_4)_3$ (LATP) and $\text{Li}_{1+x}\text{Al}_x\text{Ge}_{2-x}(\text{PO}_4)_3$ (LAGP) have very good ionic conductivities ($> 10^{-3}$ S/cm)²⁹ thanks to the substitution of Ti^{4+} or Ge^{4+} ions by smaller Al^{3+} ions decreasing the unit cell dimensions and enhancing the ionic conductivity by three order of magnitudes. However, similar to LLT materials, NASICON electrolytes contain Ti or Ge, and are thus unstable against lithium metal³⁰.

The LISICON (Lithium SuperIonic CONductor) structure (discovered by Hong in 1978) has a relatively low ionic conductivity (about 10^{-6} S/cm for $\text{Li}_{14}\text{ZnGe}_4\text{O}_{16}$) and reacts with lithium metal and CO_2 . Replacement of the oxide ions by larger sulfide ions in the framework gives rise to the thio-LISICON family of electrolytes. This family contains materials such as $\text{Li}_{3.25}\text{Ge}_{0.25}\text{P}_{0.75}\text{S}_4$ which has high ionic conductivity of 2.2×10^{-3} S/cm, and most recently $\text{Li}_{10}\text{GeP}_2\text{S}_{12}$ (LGPS), which has the extremely high ionic conductivity of 1.2×10^{-2} S/cm³¹.

Garnet crystal structures present the advantage of having high ionic conductivity (3×10^{-4} S/cm for $\text{Li}_7\text{La}_3\text{Zr}_2\text{O}_{12}$ (LLZ)³²) and high chemical stability against the lithium anode. The framework is composed of La^{3+} , Zr^{4+} , and Al^{3+} (to stabilize the structure) cations, which are not redox active at low potentials vs Li^+/Li ³³. However, to achieve the structure of garnet, high temperature sintering is necessary, which considerably complicates the battery fabrication process³³.

1.3.1.2 Inorganic glass solid electrolytes

Glassy (amorphous) materials are ductile and have very low grain boundary resistance, so high temperature is not needed for cell assembly.

Oxide amorphous materials usually have low ionic conductivities, but those with especially high Li^+ concentration like $\text{Li}_{2.9}\text{PO}_{3.3}\text{N}_{0.46}$ (LIPON) show an acceptable ionic conductivity of about 10^{-6} S/cm³⁴. In addition, these oxide glasses have very good stability in the atmosphere and against lithium metal. However, this type of electrolyte is only used in thin film batteries in order to reduce their resistance (which is proportional to thickness).

Sulfide glasses generally show high conductivities and low activation energies, owing to the weaker bonding of lithium with sulfur anions³⁵ compared to oxide anions. In particular, in the $\text{Li}_2\text{S}-\text{P}_2\text{S}_5$ system glasses typically have an ionic conductivity of over 10^{-4} S/cm at room temperature³⁶. However, they react with H_2O to generate H_2S gas, thus they are not stable in air³⁷. Addition of lithium salts such as lithium halides³⁸, lithium borohydride³⁹ and lithium ortho-oxosalts⁴⁰ can further increase their ionic conductivity by an order of magnitude, and increase their chemical stability in the atmosphere.

1.3.1.3 Inorganic glass-ceramic solid electrolytes

Glass ceramics are partially crystalline materials prepared by crystallization of amorphous glasses. They usually have higher ionic conductivities as their grain boundary resistance is low due to the presence of the amorphous phase, and their bulk conductivity is high (superionic crystals are often formed from the precursor glasses). High temperature or metastable phases can be crystallized from supercooled liquid after glass transition temperature. $\text{Li}_7\text{P}_3\text{S}_{11}$ or $\text{Li}_{3.25}\text{P}_{0.95}\text{S}_4$ are good examples of materials, with ionic conductivities above 10^{-3} S/cm⁴¹⁻⁴². Sulfide glass-ceramics possess wide electrochemical windows (up to 10 V), however, they are still reactive to atmosphere, which complicates handling in the fabrication process. Similar to the $\text{Li}_2\text{S}-\text{P}_2\text{S}_5$ glasses, several approaches can be adopted to limit their hydrolysis by water in air, such as partial substitution by oxides (Li_2O , P_2O_5)⁴³ or addition of metal oxides (Fe_2O_3 , ZnO , Bi_2O_3) which react spontaneously with H_2S , limiting the emission of H_2S gas³⁸⁻³⁹⁻⁴⁰.

1.3.1.4 Conclusion

After two decades of research, solid electrolytes that have high ionic conductivity and very low activation energy have been discovered, resulting in overall higher conductivity than liquid organic electrolytes, as shown by **Figure 3**. Sulfide electrolytes in particular have attracted great attention due to their high Li^+ ion conductivity, mechanical properties, wide selection of composition, and wide electrochemical windows. Despite their chemical reactivity with atmosphere, they are still

one of the most promising candidates for application to all-solid-state batteries, and the search for new and more stable sulfide-based ion conductors is more than ever at the order of the day.

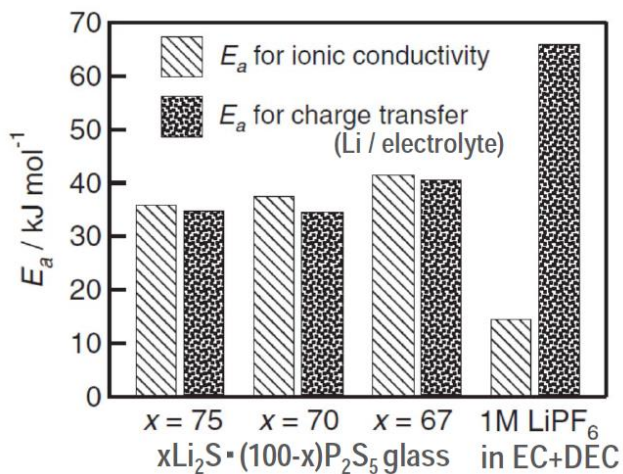


Figure 3: Comparison of activation energies for $\text{Li}_2\text{S}-\text{P}_2\text{S}_5$ glasses and conventional liquid electrolytes⁴⁴.

1.3.2 All-solid-state batteries

1.3.2.1 All-solid-state battery performance

Bulk-type all-solid-state batteries are composed of three layers (see **Figure 2b**: the composite cathode as a working electrode, the solid electrolyte, and the Li-In anode as a counter electrode. The first all-solid-state battery was first developed for Li-ion batteries, with a $\text{Li}_2\text{S}-\text{SiS}_2-\text{Li}_3\text{PO}_4$ glass for electrolyte⁴⁵. Since then, cells with other sulfide electrolytes have been investigated and more recent research has been focusing on cells using high sulfur loadings as active material.

A typical charge-discharge cycle for a lithium-ion-based all-solid-state cell is shown in **Figure 4**. The cell is composed of ($\text{Li}_4\text{Ti}_5\text{O}_{12} / \text{Li}_2\text{S}-\text{P}_2\text{S}_5$ glass /vapor grown carbon fiber (VGCF)) in a (38/58/4) weight ratio as the working electrode, $\text{Li}_2\text{S}-\text{P}_2\text{S}_5$ glass as solid electrolyte, and Li-In as the negative electrode. The current density was held constant at 12.7 mA/cm^2 . The cell exhibits remarkable stability of the initial capacity of 140 mAh/g for 700 cycles⁴⁶.

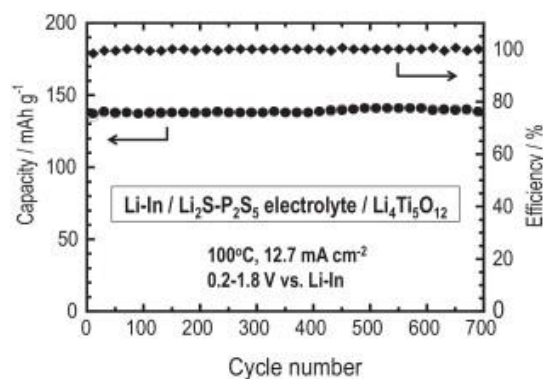


Figure 4: Charge-discharge curves of Li-In/Li₄Ti₅O₁₂ all-solid-state cell. Open and solid circles overlap each other and represent charge and discharge capacities. Solid diamonds represent the Coulombic efficiency (Tatsumisago et al. 2011)⁴⁶.

All-solid-state batteries are usually characterized by a long cycle life and better resistance at high temperature. Li-ion all-solid-state cells have already invaded the market and present fewer safety concerns than conventional liquid batteries, however they are limited by their theoretical maximum capacity and energy density. Several active materials, such as TiS₂, Mo₆S₈, FeS, and Ni₃S₂, have been investigated in performances of batteries, yet sulfur still has one of the largest theoretical capacities, as discussed in the previous sections on conventional liquid batteries. **Figure 5** below compares the cycling performance of a LiCoO₂-based cell with a sulfur-based all-solid-state battery. The sulfur cell exhibits a capacity of over 1500 mAh/g, more than 15 times larger than the capacity generated by the LiCoO₂-based cell. The sulfur battery retains 1000 mAh/g over 200 cycles at a current density of 0.64 mA/cm², which almost meets the demand of battery applications with large energy density and long cycle life⁴⁷.

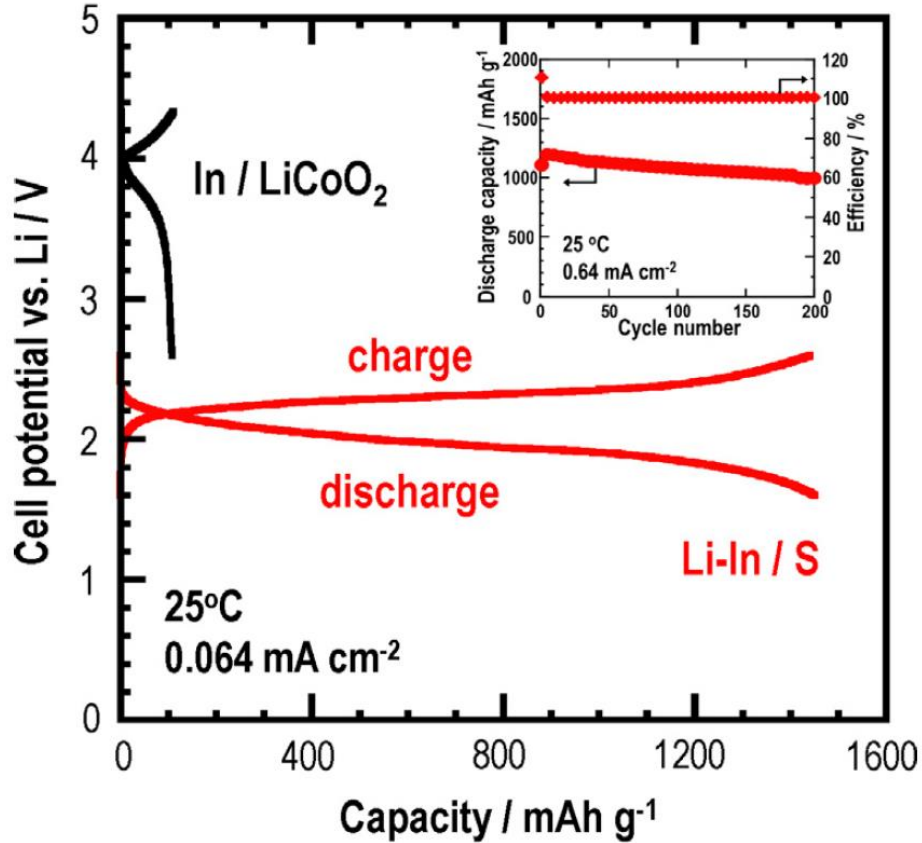


Figure 5: Charge-discharge performance of (a) an all-solid-state cell [AB-S-SE/80Li₂S-20P₂S₅ (SE) /Li-In] and (b) a LiCoO₂-based all-solid-state cell for comparison. The inset shows the cycle performance of the sulfur-based cell (Hayashi et al.⁴⁷).

1.3.2.2 Current approaches for the formation of intimate contacts

Changing from liquid to solid-state results in longer cycle life, as the phenomenon of polysulfide shuttle is completely averted. However, some issues still remain that are inherent to the sulfur materials, as well as new issues due to the solid-state nature of the materials.

Sulfur and sulfides are ionic and electronic insulators, thus, the cathode needs to be a mixture of active material (sulfur), an ionic conductor (solid electrolyte) and an electronic conductor (typically carbon-based), which results in a decrease in power density. Volume expansion upon formation of Li₂S can be problematic for contact between the different solid components in the cathode. This can be prevented by using of glassy solid electrolytes which act as a binder due to their ductility, and by using appropriate mixing and deposition processes for the cathode fabrication.

Since charge-transfer reactions occur at the interfaces, an intimate contact at the solid/solid interfaces must be made between electrodes and electrolyte on one hand, and between the different composites of the cathode on the other hand. Different methods have been developed to enhance contact surface area within the composite cathode and are schematically presented in **Figure 6**.

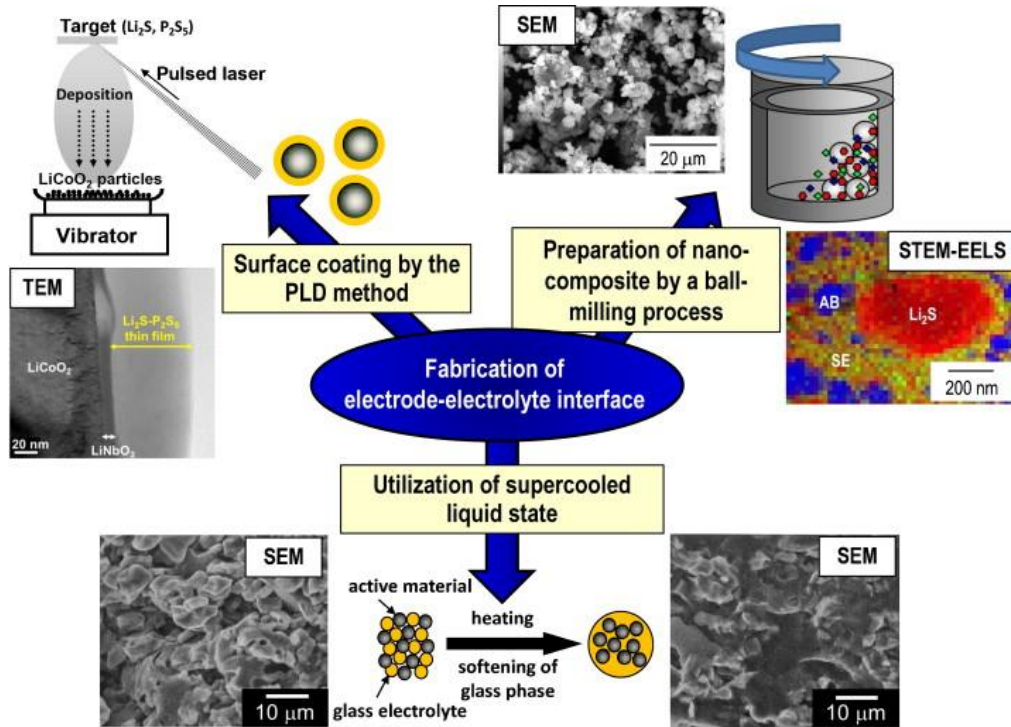


Figure 6: Different approaches to realize intimate contact between composites in the electrodes⁴⁷.

One way to produce good contact between electrolyte and active material in the cathode is the use of mechanical milling to reduce the size of the materials to the nanoscale. This increases the contact area⁴⁸ and results in active material and carbon embedded in a matrix of solid electrolyte, as shown in the STEM-EELS image in **Figure 6**. Another approach is to coat active material particles (e.g. LiCoO_2) with solid electrolyte by pulsed laser deposition⁴⁹. A thin film of 70 nm in thickness was achieved (see TEM image in **Figure 6**) with high adhesion to the particles. Finally, another method is to use the glassy nature of the sulfide solid electrolytes. A mixture of active material and solid electrolyte is heated to the supercooled liquid state temperature (glass transition temperature) of the glasses. The softening of the electrolyte creates an amorphous matrix in which the active material is embedded, reducing the grain boundaries and increasing the contact areas. The last two techniques are more difficult to apply to sulfur as an active material, as it has a relatively low melting point (160°C), but nano particles of Li_2S can be used as a starting active material to circumvent this

problem. All of these methods result in larger charge-discharge capacities and better cyclability thanks to better activation and utilization of the active material by increasing of contact. Some of the best results are obtained with a combination of supercooled state and milling treatment⁵⁰.

At the electrolyte-anode interface, contact area can be improved by forming a thin film of indium at the surface of the solid electrolyte pellet by a vacuum-evaporation process. This contributes to a better reversibility of the Li deposition and dissolution processes, limiting dendrite growths⁵¹.

Better contact within the solid electrolyte can be obtained by hot pressing. It has been shown that hot pressing increases the density of the solid electrolyte, enabling better ion transfer and conductivity, higher resistance to lithium dendrite growth, and better interface contact with the electrodes⁵²⁻⁵³.

1.4 Summary

Li-S batteries were first introduced by Ulam et al. in 1962, and despite their high theoretical specific capacity of 1672 mAh/g, their practical application has been hindered by many technical issues, preventing them from invading industrial markets. One solution to meet the world's demand for energy is all-solid-state Li-S batteries which have a higher energy density and higher capacity retention than liquid batteries, as the polysulfide shuttle responsible for fast cell decay is completely inhibited. Furthermore, for electric vehicle applications, stacked solid batteries are convenient and safe, and decrease the risk of leakage, flammability, and explosion.

The search for solid electrolyte materials that are ionically conductive enough to match the performance of liquid organic electrolytes started two decades ago and is still ongoing. For bulk-type batteries, sulfide-based electrolytes are promising candidates, owing to their high ionic conductivity, mechanical properties, and wide electrochemical window. The materials $\text{Li}_{10}\text{GeP}_2\text{S}_{12}$ (crystalline) and $\text{Li}_7\text{P}_3\text{S}_{11}$ (glass-ceramics) in particular have attracted much attention due to their high ionic conductivity $\geq 10^{-2}$ S/cm. The only drawback is their chemical reactivity in air, which would result in expensive processes in industrial manufacturing. At the laboratory scale, various methods to enhance contact surface areas between electrode and electrolyte have been developed. However, much research on the architecture, morphology, distribution and size of the composites in the positive electrode need to be carried out to achieve favorable electrochemical and ionic pathways at a larger

scale. Rapid degradation of the lithium anodes by the growth of dendrites is still a major problem, and only a better understanding of electrode/electrolyte interfaces and of the lithium deposition process can mitigate this issue with an adapted tailoring of the microstructures. New solid electrolytes with higher Li^+ ion conductivity and chemical stability are needed for upscaling. Finally, as only 25 weight % is typically used in most solid-state batteries, higher sulfur loadings (at least 50%) in the composite cathode would be necessary to increase power density.

1.5 Scope of this thesis

This thesis will be focused on the synthesis of sulfide-based solid electrolytes and their application to all-solid-state batteries. **Chapter 1** gave a general introduction on the energy demand and need for high energy density rechargeable batteries. **Chapter 2** describes the characterization methods and techniques used in this thesis. **Chapter 3** focuses on the synthesis of the superionic conductor $\text{Li}_7\text{P}_3\text{S}_{11}$ and investigation into new phases discovered in sulfide glass systems. **Chapter 4** explores the performance of all-solid-state Li/S batteries with different solid electrolytes and cathode compositions.

Chapter 2:

Characterization Methods and Techniques

2.1 Powder X-Ray Diffraction

X-Ray Diffraction (XRD) has become the most common technique to analyze crystal structures, and it is the primary analytical method used in this thesis to identify synthesized materials. Laue et al. discovered in 1912 that X-ray radiation can be diffracted by crystals because their wavelength is of the same order of magnitude as interatomic distances ($10 \text{ nm} < \lambda < 0.01 \text{ nm}$). In 1913 Sir William Bragg discovered a more simple law to express the necessary conditions for diffraction of X-rays by crystal planes. This law, known as “Bragg’s Law”, can explain the appearance of a unique diffraction pattern which identifies a specific structure.

$$n\lambda = 2d \sin\theta$$

The law is schematically illustrated in **Figure 7**. If we consider incoming parallel X-ray beams of wavelength λ , forming an angle θ with a set of parallel lattice planes separated by a distance d , then the beam going into a deeper plane travels an extra distance of $2d \sin\theta$. Then, if it is a multiple of the incident wavelength, the two waves interfere constructively, and due to Bragg’s law, each diffracted peak can be associated to a d -spacing if θ is fixed.

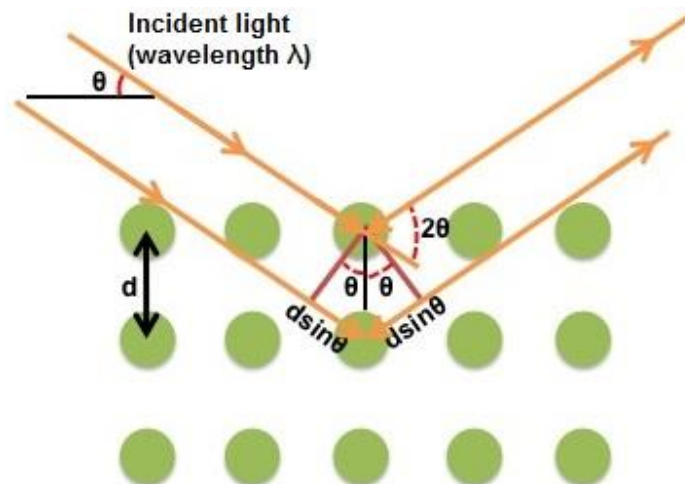


Figure 7: schematic illustration of Bragg's law

In an X-ray diffractometer, the sample is rotated with regards to the incident beam and scanned over a range of θ (or 2θ) and the intensity of diffracted X-rays are measured as a function of the angle. Any possible crystal orientation gives rise to diffraction corresponding to each d spacing present, thus powder samples are likely to give all the information about the material's structure. The obtained pattern is affected by various properties. First, the overall area under all peaks belonging to one phase on the XRD pattern is proportional to the weight fraction of this phase in the sample. Secondly, the crystallinity of the sample is proportional to the peaks intensity. Lastly, the peaks widen as crystallite size decreases (if they are typically less than $1 \mu\text{m}$) due to diffraction by grain boundaries.

XRD patterns in this thesis were collected using a Bruker D8-Advance powder X-ray diffractometer operating at 40 kV and 30 mA and using Cu-K α radiation ($\lambda=0.15405 \text{ nm}$) unless otherwise stated. Air-sensitive samples were applied on a silicon zero-background holder and a protective Kapton film was sealed with vacuum grease on top to allow X-ray penetration while avoiding any exposure to air during measurements. For long scans (more than 7h), the powdered samples were transferred into glass capillary tubes (0.5 mm diameter) sealed with an acetylene-oxygen torch.

Structure determination and refinement of the XRD patterns were performed using the software TOPAS. First, the unknown peaks were indexed and fitted with the best solutions of space group and lattice parameters (proposed by a random-based LeBail algorithm). Once a few potential candidates are selected, charge flipping is carried out with TOPAS to determine the structure and the

atom sites in the unit cell. This method basically fits the reflection intensities of the peaks using an iterative algorithm based on the distribution of electron density.

2.2 Differential Scanning Calorimetry

Differential scanning calorimetry (DSC) is a widely used thermoanalytical technique which can provide qualitative and quantitative information about chemical, physical and heat capacity changes that involve endothermic or exothermic processes. As much as XRD analysis, this method has been crucial to the synthesis of the materials in this thesis. The sample to be analyzed (typically 3-15 mg) and a reference sample are placed on heaters inside the analytical chamber, as illustrated by **Figure 8**.

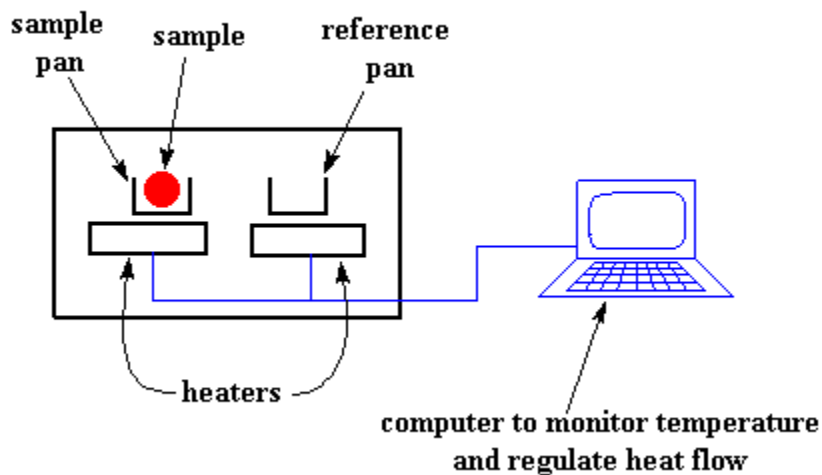


Figure 8: Schematic of a DSC instrument.

Both heaters impose the same heating ramp to the reference and the sample and the temperature is kept the same in both pans. When the sample undergoes a physical transformation, such as a phase transition, more (or less) heat will need to flow to it than to the reference so as to maintain both at the same temperature. As a result, the difference of heat flow provided to the sample and the reference is measured as a function of temperature. Typically exothermic changes such as crystallization require an increase in heat flow, and endothermic processes like melting a decrease of the heat needed by the sample. **Figure 9** shows the most common features obtained by DSC.

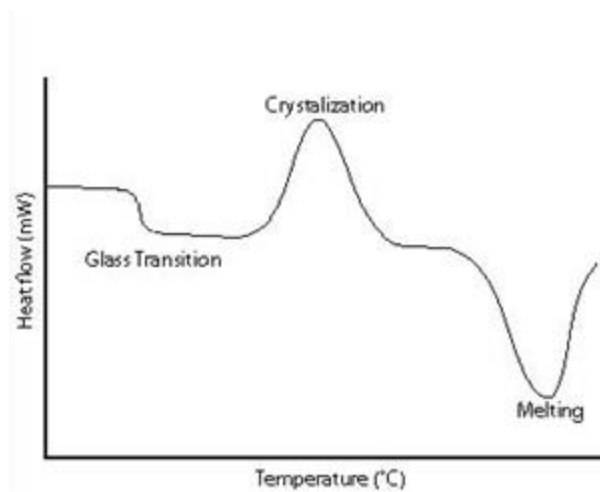


Figure 9: Features of a DSC curve.

Other information can be obtained from a DSC measurement. The area of a peak is directly proportional to the heat absorbed or released by the reaction, thus it is also proportional to the number of nuclei in the sample that undergoes the thermal transformation. It is thus possible to determine the degree of crystallinity of a heat-treated sample, which was initially amorphous material, with several measurements.

$$\Delta H = K \cdot A$$

Where ΔH is the enthalpy of transition, K is the calorimetric constant (specific to the instrument), and A the peak area.

DSC measurements for this thesis were conducted using a TA Instruments DSC Q2000 under constant nitrogen flow. The air-sensitive samples, as well as the reference (Ar) were sealed beforehand in hermetic aluminium pans in an argon-filled glovebox with a Tzero sample press.

Thermogravimetric Analysis (TGA) was also occasionally performed under nitrogen flow on a TA Instruments SDT Q600 analyzer. TGA is very similar to DSC in that both the sample and reference are heated at the same rate, but TGA measures the difference in mass between the sample and the reference as the temperature is increased, rather than heat flow. This method is more adapted for phase or chemical reaction analyses.

2.3 Surface area/pore size characterization

Surface area and pore size characterization rely on physisorption or Van der Waals interactions between the adsorbate (N_2) and the solid surface of a material. N_2 adsorption/desorption isotherms are collected at a constant temperature (77K in a liquid nitrogen bath) while the gas pressure is periodically increased. The ability of a material to adsorb the gas molecules is directly correlated to its surface area and pore characteristics and it is measured by the relative pressure in the sample chamber compared with the reference chamber. Prior to the measurement, the sample is outgassed at an appropriate temperature (60-90°C for sulfur-composites) to ensure that the surface is free of gas molecules. In this thesis, surface area and pore volume were determined on a Quantachrome Autosorb-1 instrument and calculated respectively from Brunauer-Emmett-Teller (BET) theory and from the amount of N_2 adsorbed at a relative pressure P/P_0 of 0.99 (P is the pressure inside the tube and P_0 the standard pressure).

2.4 Raman Spectroscopy

Raman spectroscopy is a technique that provides information about vibrational and rotational modes in a molecule, and thus generates spectral lines that are inherent (fingerprints) to a specific grouping of atoms within a structure. When monochromatic light (e.g. from a laser) is shone on a material, the photons will either be elastically scattered back (Rayleigh scattering) or, more infrequently interact with the molecule and be inelastically emitted back, changing the energy and frequency of the photons (Stokes-Raman scattering). Each molecule has a unique set of vibrational energy levels, so measuring the shift in energy of the reemitted photons can help to identify different structures in a sample. In a Raman Spectrometer, a laser is used to illuminate the sample, the photons of the same wavelength as the incident laser beam (elastic scattering) are filtered, while all other photons are amplified, resulting in a Raman spectrum.

In this thesis a RAMAN HORIBA HR800 was used. As all the materials are air-sensitive, they were put on an optical microscope slide and sealed with a cover slip with epoxy glue.

2.5 Scanning Electron Microscopy and Energy Dispersive X-Ray Spectroscopy

Scanning Electron Microscopy (SEM) is a technique for high-resolution imaging of the morphology and topography of solid samples. In an SEM instrument, the surface of the sample is bombarded by high-energy electrons, which generates a variety of signals - secondary electrons, back-scattered electrons, transmitted electrons, and X-rays characteristic to the elements in the sample – that are collected by specific detectors. Different information is provided by the different types of electrons: secondary electrons give information on topography and back-scattered electrons are characteristic of the distribution of elements. A secondary electron is generated if upon bombardment, a low-energy shell electron is hit and excited enough to leave a hole behind. The hole is then filled by an outer higher-energy shell electron, generating an x-ray from the lowering in its energy, which is characteristic of the emitting element and of the difference in energy. The collection of these x-rays by Energy X-ray Spectroscopy (EDX) can provide an element distribution mapping of the sample area.

SEM and EDX measurements in this thesis were performed on a LEO 1530 field emission SEM equipped with an EDX Zeiss attachment.

2.6 Electrochemical measurements

2.6.1 Solid-state cell design

Starting an all-solid-state battery project in our lab required a significant change in the design of the batteries, which cannot be run in regular coin cells. The issues involved with solid-state batteries are very different from traditional lithium sulfur liquid-based electrolyte batteries. Special attention had to be given to the solid-solid interfaces between the three components in the design of the solid-state cell. **Figure 10** presents a schematic view of an all-solid-state battery. The positive electrode is a mixture of active material (sulfur in most cases), ionic conductor (solid electrolyte), and electronic conductor (typically carbon). Then comes a layer of solid electrolyte, and since the electrolyte is often reactive against the reducing surface of lithium metal, a lithium-indium alloy is used as a counter-electrode to protect the electrolyte.

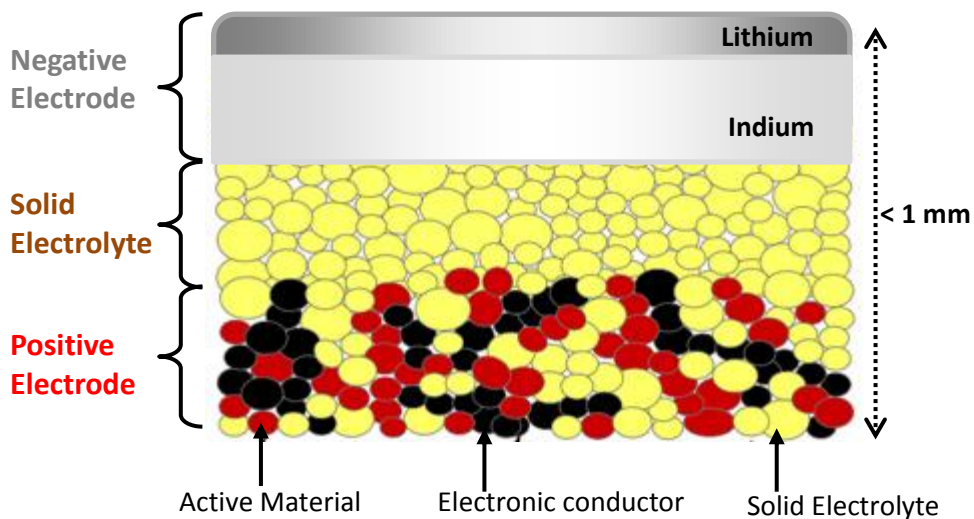


Figure 10: Schematic illustration of an all-solid-state battery

To prepare a battery, generally about 80 mg of solid electrolyte is placed in a polycarbonate cylinder and pressed between two stainless steel current collectors at 160 MPa. Then the composite cathode powder (about 10-15 mg) is added, and the two layered pellet is pressed at 360 MPa. Finally, indium foil and lithium foil are applied on the opposite side and the cell is pressed at 200 MPa. The cylinder is then placed in a holder, tightened by screws to maintain the pressure on the pellet, and current is flowed through two screws in the center of the current collectors.

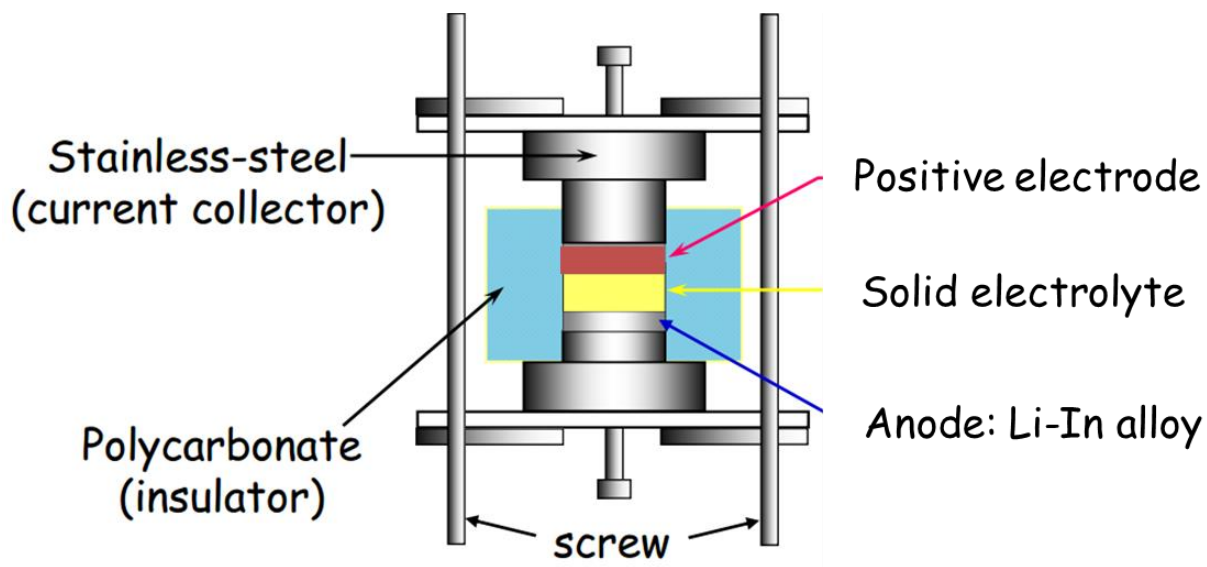


Figure 11: Illustration of an all-solid-state battery cell.

Assembly of the cell is carried out in an argon filled glovebox, and as the glovebox is not equipped with VMP3 channels yet, the cell is placed in a glass jar sealed by a rubber stopcock, wrapped with Parafilm for better protection against air-contamination, and run on a lab bench.

2.6.2 Galvanostatic cycling

This protocol is the most standard technique to study battery performance. In this mode, a window of voltage is defined (according to the open circuit voltage, electrochemical stability of the materials, etc) and a constant current is applied to the cell until discharge ends at the lower cut-off voltage. The current is then reversed and the battery charges until the upper cut-off voltage is reached. The voltage of the cell is measured as a function of step time or capacity delivered. Long-term performance is evaluated by the retained specific capacity values as a function of cycle numbers. Finally rate capability studies can be performed by increasing the current applied for a number of cycles and then returning to the initial current to see the difference in terms of capacity and general behavior. Galvanostatic measurements were carried out on a VMP3 potentiostat/galvanostat station with Electrochemical Impedance Spectroscopy (EIS) capabilities (BioLogic Science Instruments).

2.6.3 Cyclic Voltammetry

For cyclic voltammetry measurements, the current is recorded as a function of the potential applied. The cell is cycled by applying typically a voltage ramp linear over time and once the voltage reaches its upper or lower limit, it is reversed. This technique provides clear information about the redox reactions occurring with cycling. From the area and the width of the peaks can be inferred information about the amount of material involved and the kinetics in the transformation. CV measurements in this thesis were carried out on a VMP3 potentiostat/galvanostat station with EIS/Z capabilities (BioLogic Science Instruments).

2.6.4 Electrochemical Impedance Spectroscopy

The impedance of a circuit characterizes its ability to resist the flow of electrical current. Electrochemical impedance is measured by applying an alternating current (AC) potential within a wide range of frequencies to an electrochemical cell. The generated current signal is measured and can be analyzed as a sum of sinusoidal functions. The amplitude of the potential applied is typically low to just enable a linear response from the cell which is a non-linear electric element.

In this thesis, impedance is described by a complex value consisting of a real and an imaginary part, and displayed as a Nyquist plot (the imaginary part plotted as a function of the real part). Generally, for impedance measurements on a solid electrolyte, the Nyquist plot is composed of three semi-circles on the left in the high frequency range, and an inclined line on the right at low frequencies. The three semi-circles correspond to resistance and capacitance of the bulk, the grain boundaries of the electrolyte, and the electrolyte/current collector interface. At room temperature the three semi-circles often form a single semi-circle, and the total impedance of the solid electrolyte is the sum of the three resistances previously listed. The straight line relates to the overall electrolyte resistance. **Figure 12** below illustrates a typical Nyquist plot for a solid ionic conductor. When the semi-circle is not well defined in the measurements, we can obtain the value of the resistance by extrapolation of the linear part to the x-axis.

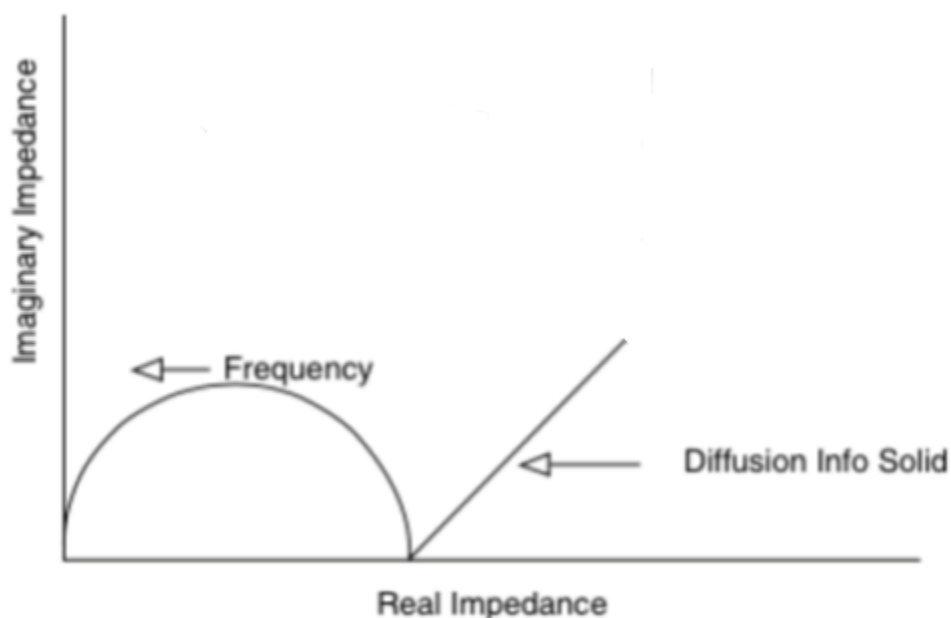


Figure 12: Typical Nyquist plot of impedance measurement on a solid electrolyte.

In this thesis, EIS measurements were carried out on a BioLogic Science Instrument VMP3 potentiostat/galvanostat station with EIS/Z capabilities. The DC voltage was kept at open-circuit, and the AC voltage was applied with a frequency range from 1 MHz to 0.1 Hz.

Chapter 3:

Synthesis and characterization of sulfide-based solid electrolytes

3.1 Introduction

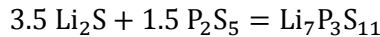
In the Li/S battery field, all-solid-state batteries draw a lot of attention, because despite significant improvement of cathode architecture, the polysulfide shuttle has not been completely inhibited in liquid-based cells. Two major goals in all-solid-state battery research is to develop suitable solid electrolytes, with high ionic conductivity, and to create a favourable interface between all the solid components. Sulfide-based solid electrolytes are among the most promising candidates thanks to their high ionic conductivity and remarkable mechanical and electrochemical properties. In this chapter, we first study synthesis methods of the well-known superionic conductor $\text{Li}_7\text{P}_3\text{S}_{11}$. Then, two unknown phases are identified in the $\text{Na}_2\text{S-P}_2\text{S}_5$ glasses system. Finally, a new phase, Li_2NaPS_4 is reported in the third section.

3.2 $\text{Li}_2\text{S-P}_2\text{S}_5$ glasses

Among solid-state sulfide electrolytes, the $\text{Li}_2\text{S-P}_2\text{S}_5$ glasses have attracted a lot of attention due to their particular high ionic conductivity (over 10^{-3} S/cm). Many efforts have especially been made to form the superionic conductor $\text{Li}_7\text{P}_3\text{S}_{11}$, which was reported to have an ionic conductivity of about 5.0×10^{-3} S/cm⁵⁴ in most literature, and of 1.1×10^{-2} S/cm in a more recent paper by Hayashi et al.⁵⁵. The goal at the beginning of this project was to synthesize this promising solid electrolyte and to apply it to Li-S all-solid-state batteries. We have attempted to develop a more systematic method to synthesize this metastable phase at a larger scale (more than a few hundred milligrams) and to optimize all of the experimental parameters to enhance its conductivity for use in all-solid-state batteries.

3.2.1 Synthesis of $\text{Li}_7\text{P}_3\text{S}_{11}$

The synthesis of $\text{Li}_7\text{P}_3\text{S}_{11}$ is traditionally composed of two steps. The first step is the preparation of the amorphous glasses which are then heat-treated in the second step to form the glass-ceramics. The precursors Li_2S and P_2S_5 are mixed in a 70:30 molar ratio, following the equation below:



Two different routes of synthesis of the 70. Li_2S -30. P_2S_5 glasses are typically used ⁵⁴: the quenching route (from the melt) and the milling route (solid-state reaction). In the quenching method, the precursors, Li_2S and P_2S_5 , are milled for an hour, heated to 750°C (above melting point), then slowly cooled down at around 700°C. After maintaining this temperature for several hours, the mixture is quenched in an ice bath. In the milling method, the precursors are only milled in a planetary ball mill apparatus (FRITSCH PULVERISETTE 7 Premium) until the precursor materials have reacted and are no longer present in a crystalline form.

Variations in the milling parameters (speed, milling time, material and size of the balls and jars) have been used to evaluate their influence on the quality of the obtained material. Subsequently, the obtained glasses are analyzed by DSC and heat-treated at temperatures corresponding to exothermic peaks in the DSC measurements.

Different heating parameters have also been studied to obtain the best material. The temperature of the heat-treatment, holding time, heating rate, cooling rate, material form (powder or compressed pellet), material of the crucible (alumina, Inconel, carbon, gold, platinum, glass, quartz), atmosphere (flow or static atmosphere, argon, nitrogen, vacuum...) all affect the quality of the final product. The influence of all of the different synthesis parameters have been studied and discussed at length in the literature, so this section will mainly focus on the conclusions drawn from our own experiments to determine the best systematic method to purely synthesize the $\text{Li}_7\text{P}_3\text{S}_{11}$ phase with improved conductivity.

3.2.2 Influence of synthesis parameters

3.2.2.1 Milling parameters

There are several milling parameters that can influence the quality of the obtained glasses:

- the milling speed
- the milling time
- the material and size of the grinding balls and milling jars

All parameters are correlated, as milling consists of mechanical shocks that break the structures, reduce the particle sizes of the materials, and generate thermal energy, thus favouring thermally-controlled reactions.

Material and size of grinding jars and balls

It has been shown that the best glasses (finely ground and homogeneous) were obtained using ZrO₂ jars and balls. A large number of small balls was more efficient at breaking the structures in a consistent and homogeneous way than a small number of large grinding balls. In this work, for 45 mL ZrO₂ jars, 300 balls of 5 mm in diameter were typically used.

Milling speed and milling time

Two rounds of glasses are compared in this section. One has been milled at 400 rpm for 22 hrs (“low-speed” milling) and the other at 900 rpm for 30 min (“high-speed” milling). **Figure 13** shows the XRD patterns of both rounds. The glasses milled at 400 rpm exhibit an amorphous pattern after 22 hours of milling (the precursors Li₂S and P₂S₅ have reacted and are no longer present). After milling the glasses at 900 rpm for 30 min, Li₂S and P₂S₅ are not only no longer present, but some crystallization of the Li₇P₃S₁₁ phase has occurred.

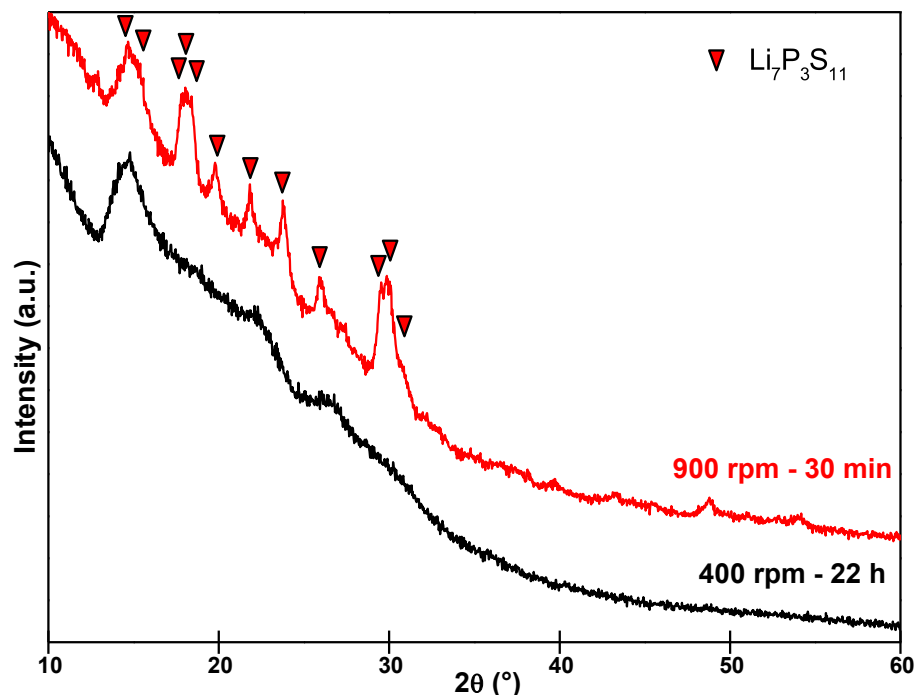


Figure 13: XRD patterns of glasses milled at 400 rpm for 22 hours and of glasses milled at 900 rpm for 30 min.

The DSC (**Figure 14**) of the glasses milled at 900 rpm only exhibits two very small exothermic peaks at 216°C (peak **A**) and 320°C (peak **B**), respectively, representing no major crystallization events. However, for the amorphous glasses, significant phase change occurs at 250°C (peak **A'**) and 345°C (peak **B'**). These results agree with the XRD features of the two glasses presented in **Figure 13**. The sample milled at 900 rpm is already partially crystalline, resulting in less amorphous material that can crystallize and thus less intense crystallization peaks on the DSC. Additionally, there are significant shifts in the crystallization temperatures observed for the amorphous glass and the already semi-crystalline glass. This can be attributed to the presence of $\text{Li}_7\text{P}_3\text{S}_{11}$ crystals in the amorphous matrix, indicating that the formation of this phase is favored via nucleation for high-speed milling. Hence, lower crystallization temperatures are required because the crystal growth process requires less energy than the nucleation process.

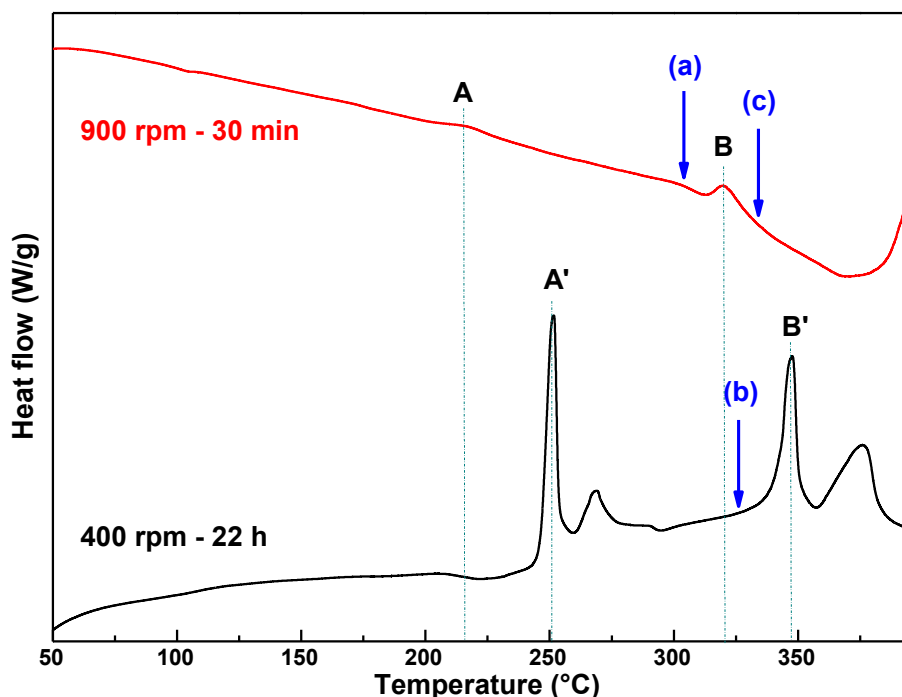


Figure 14: DSCs of $\text{Li}_2\text{S}-\text{P}_2\text{S}_5$ glasses after milling at 900 rpm for 30 min and at 400 rpm for 22 h respectively.

Both rounds of glasses were heat-treated following their DSC results (before and beyond each exothermic peak) and the results are later compared (see 3.2.2.2 Temperature of Heat-Treatment) to see which milling program leads to more crystalline $\text{Li}_7\text{P}_3\text{S}_{11}$.

Amount of milled material

It is crucial to begin with homogeneous glasses to obtain uniform crystallization when the glasses are heat-treated. Attempts have been made to upscale the synthesis of $\text{Li}_7\text{P}_3\text{S}_{11}$, however, having more than 3 g in a ball milling jar (even big 500 mL jars) results in systematic agglomeration of the material after that the particles reach a specific size. Heat-treatments of the glasses showed irreproducible results, with a tendency to develop poorly crystalline $\text{Li}_7\text{P}_3\text{S}_{11}$ along with other impurity phases. **Figure 15** shows the XRD patterns of the same round of glasses (a 6g batch) after identical heat-treatments with identical conditions. After 16 to 18 h of milling, the glasses systematically agglomerated in the bottom of the jar and crushing the build-up of materials by hand after every two hours of milling was necessary to obtain amorphous glasses (≥ 30 h total required). After the heat-treatment, glass (1) exhibited significantly more of the Li_3PS_4 impurity phase than

glass (2). The overall crystallinity of the products was also very low. Starting with inhomogeneous glasses results in unpredictable quality of $\text{Li}_7\text{P}_3\text{S}_{11}$ for two identical heat-treatments.

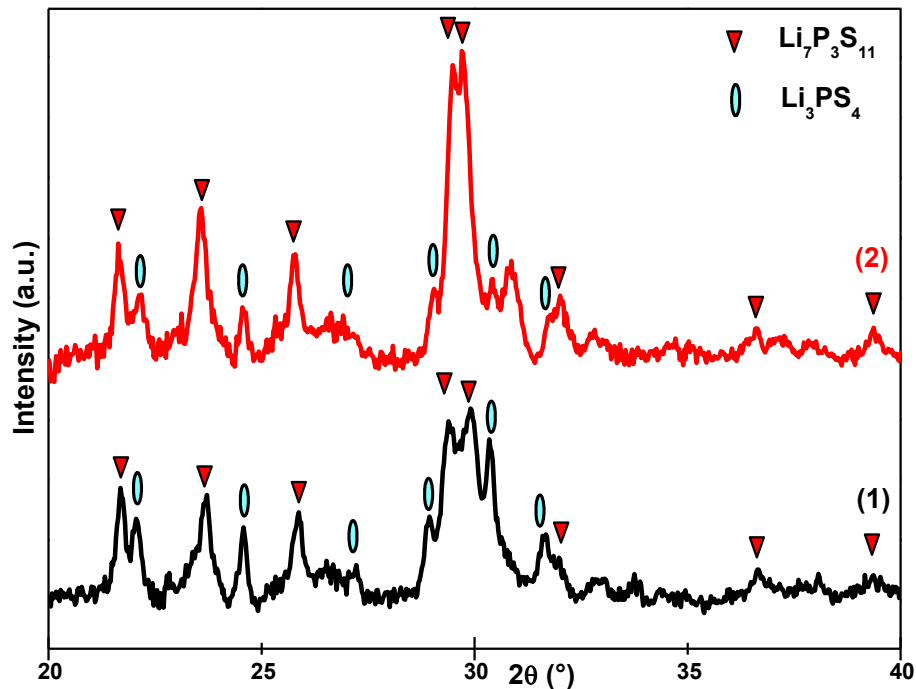


Figure 15: XRD patterns of 70-30 Li_2S - P_2S_5 glasses after heat-treatment at 250°C , performed with identical conditions.

3.2.2.2 Temperature of heat-treatments

Heat-treatments have been performed at the temperatures corresponding to thermal changes in the DSC measurements of the low- and high-speed milled glasses presented in the previous section. All other heat-treatment parameters were held constant so that the effect of the temperature of the heat-treatment and of the milling speed on the quality of the $\text{Li}_7\text{P}_3\text{S}_{11}$ obtained can be observed.

From the observations made of various heat-treatments performed on both rounds, it appears that the peaks **A** and **A'** correspond to crystallization of $\text{Li}_7\text{P}_3\text{S}_{11}$, and the peaks **B** and **B'** to decomposition of $\text{Li}_7\text{P}_3\text{S}_{11}$ into Li_3PS_4 and $\text{Li}_4\text{P}_2\text{S}_6$. Furthermore, the best crystallization of $\text{Li}_7\text{P}_3\text{S}_{11}$ is achieved when heat-treating at a temperature just before the thermal changes **B** and **B'**. **Figure 16** below shows the XRD patterns of the high-speed milled glasses after heat-treatment at temperatures just before peak **B** (**Figure 15(a)**) and just after peak **B** (**Figure 15(c)**), and of the low-speed milled

glasses after heat-treatment at a temperature just before peak **B'** (**Figure 15(b)**). These temperatures are correspondingly marked by arrows (a), (b) and (c) on the DSC curves in **Figure 13**. Both (a) and (b) exhibit a pure $\text{Li}_7\text{P}_3\text{S}_{11}$ pattern, but the sample analyzed after heat-treatment of the high-speed milled glasses is significantly more crystalline, suggesting that it is a better way of milling. Heat-treatment (c), performed after the decomposition peak **B**, shows very crystalline $\text{Li}_4\text{P}_2\text{S}_6$ mixed with some Li_3PS_4 .

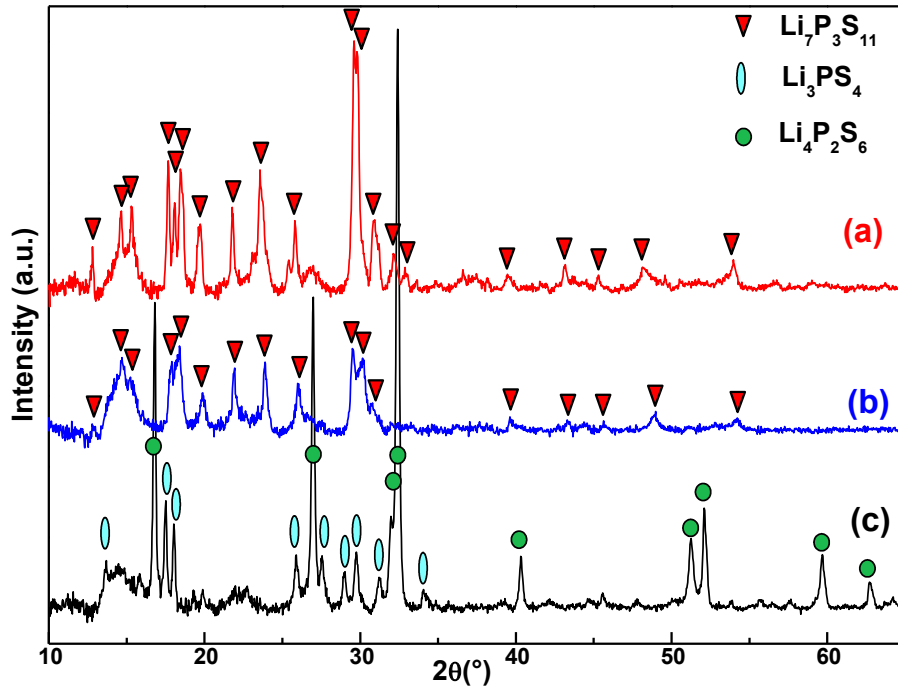


Figure 16: XRD patterns of high-speed milled glasses after heat-treatment at 300°C (a) and at 330°C(c), and on low-speed milled glasses after heat-treatment at 325°C (b).

3.2.2.3 Holding time

To determine the influence of holding time, three samples of the same mass and round of milled glasses were heat-treated at the same temperature (250°C) for 1, 2, and 3 hours. All other parameters were held constant. **Figure 17** shows the XRD patterns of the resulting materials after heat-treatment. After 1 hour of heat-treatment, a fairly low crystallization of $\text{Li}_7\text{P}_3\text{S}_{11}$ is obtained. After 2 hours, the amount of $\text{Li}_7\text{P}_3\text{S}_{11}$ has increased, however a few new peaks corresponding to $\text{Li}_4\text{P}_2\text{S}_6$ are also present. Lastly, after 3 hours the crystallinity of $\text{Li}_7\text{P}_3\text{S}_{11}$ has decreased compared to the 2-hour heat-treatment, and the peaks of $\text{Li}_4\text{P}_2\text{S}_6$ have increased in intensity. This seems to indicate

that after formation of the first nuclei of $\text{Li}_7\text{P}_3\text{S}_{11}$, longer holding time increases the crystallinity up to a critical time after which the phase begins to decompose into $\text{Li}_4\text{P}_2\text{S}_6$. These results show that the material is very sensitive to heat-treatment holding time.

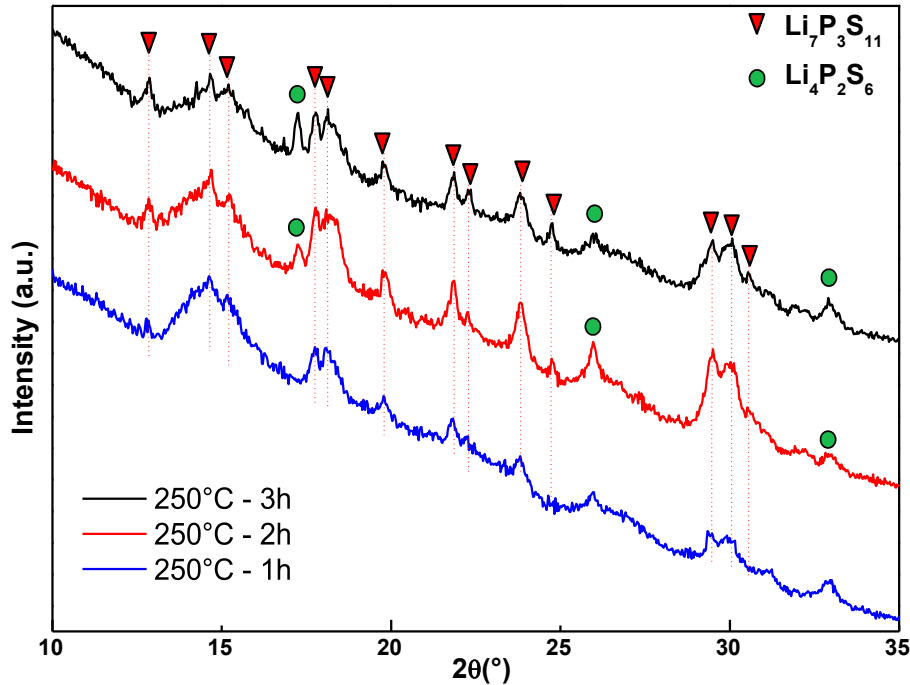


Figure 17: XRD patterns of identical samples that have been heat-treated at 250°C for different holding times.

3.2.2.4 Heating and cooling rates

Figure 18 compares the XRD patterns of glasses heat-treated with different heating and cooling rates. The first (**sample 1**) was heat-treated at a 5°C/min rate to 300°C, held for 1 h, and then rapidly cooled to room temperature by removing the sample from the furnace. The second (**sample 2**) was heat-treated quickly by placing in a furnace that was stabilized at the set temperature, held for 1 h, and then cooled slowly (about 3°C/min) in the furnace. The third (**sample 3**) was heat-treated with fast heating and cooling by placing the sample in an already hot furnace and removing it after 1 h of heat-treatment. The fast heating rate was calculated to be about 200°C/min, and the fast cooling rate to be about 30°C/min. The heating and cooling rates are directly related to the holding time parameter. For an equivalent holding time, a faster heating rate gives less exposure to heat, so the material will not crystallize or decompose as much as if a slow heating rate was used. **Figure 18**

shows that the heating rate has to be considered in addition with the holding time (a slow heating rate with a short holding time might be equivalent to a fast heating rate and a longer holding time). The most crystalline $\text{Li}_7\text{P}_3\text{S}_{11}$ was obtained with **Sample 3** (fast rates) which formed without any impurities. **Sample 1** (slow heating rate) exhibits fairly crystalline $\text{Li}_7\text{P}_3\text{S}_{11}$ as well but with some extra peaks as a result of decomposition. **Sample 2** (slow cooling rate) shows considerable decomposition of $\text{Li}_7\text{P}_3\text{S}_{11}$ into Li_3PS_4 , which indicates that the cooling rate has a major impact on the crystallization process. This is not surprising as $\text{Li}_7\text{P}_3\text{S}_{11}$ is a metastable high temperature phase. This phase needs to be stabilized kinetically in order to achieve high degrees of crystallization. In theory, better samples can usually be obtained by decreasing the cooling rate further by quenching in an ice bath, however this requires more preparation as the material has to be compressed in pellets and sealed under vacuum in a quartz tube. In practice, this method is not more efficient to form good materials and is in addition more time- and effort- consuming than the fast cooling method used here (see sections on influence of form of material and of atmosphere type).

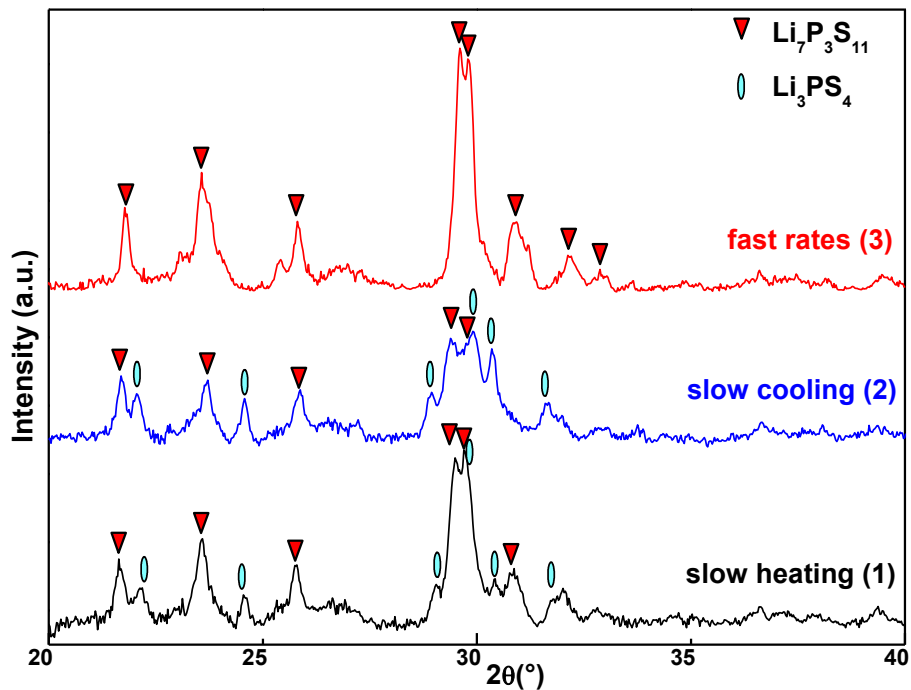


Figure 18: XRD patterns of heat-treated glasses with (1) a slow heating rate and fast cooling rate, (2) a fast heating rate and a slow cooling rate, and (3) fast heating and cooling rates.

3.2.2.6 Amount of material

Two samples of different quantities were heat-treated from the batch of glasses with the exact same conditions. The first sample has a mass of 50 mg and the second a mass of 200 mg. The XRD patterns of the two samples after heat-treatment are shown in **Figure 19**. As expected, the sample with a smaller mass crystallized significantly more than the sample with a larger mass. The amount of material has a huge impact on the heat-treatment results.

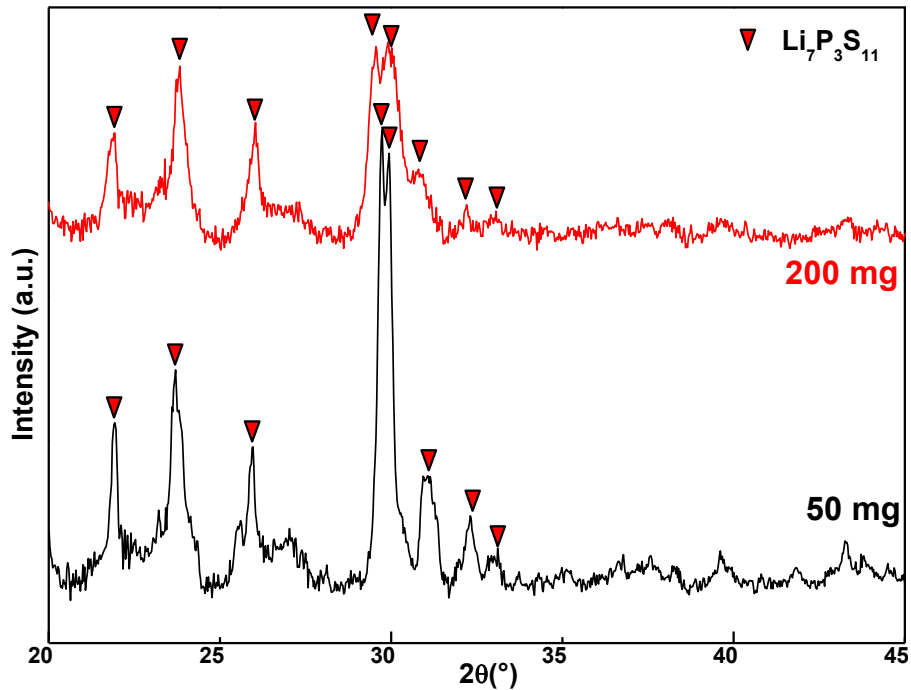


Figure 19: XRD patterns of samples after heat-treatment of 50 mg and 200 mg of glasses.

3.2.2.7 Form of the material

Two heat-treatments were performed on the same batch of glasses, one in powder form and the other with the powder pressed into a pellet. **Figure 20** shows the XRD patterns of the powders after heat-treatment. Slightly lower crystallinity is obtained for the heat-treated pellet. As it is more compact, it takes longer to reach the heat-treatment temperature, thus requiring a longer holding time to achieve the same crystallinity as the powdered sample.

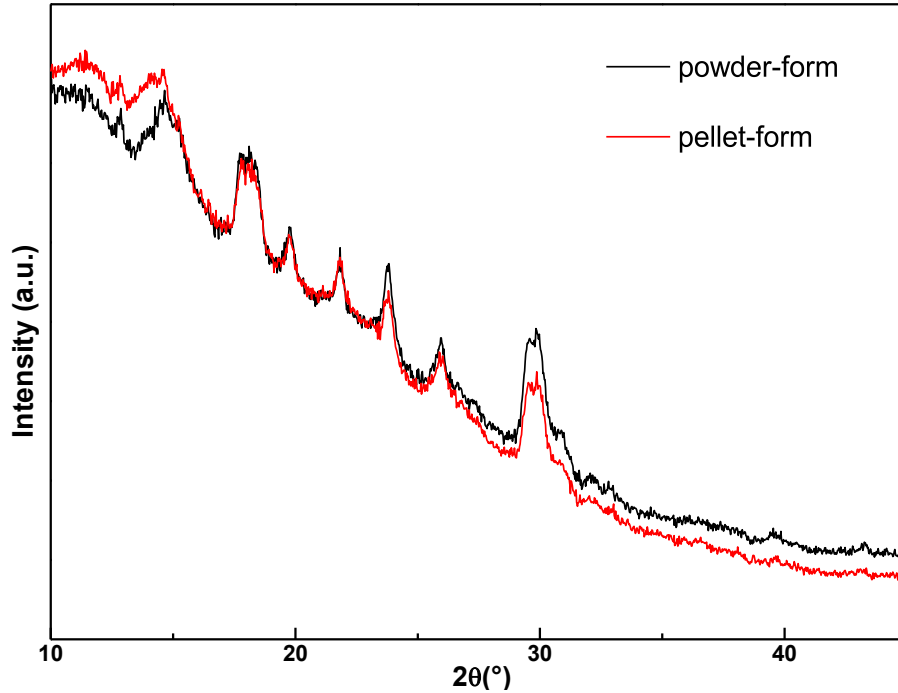


Figure 20: XRD patterns of heat-treatments performed on (a) a powder sample and (b) a pelletized sample.

3.2.2.8 Crucible material

Several crucible materials have been investigated, including alumina, gold, inconel, and quartz/glass. **Figure 21** presents the results of samples heat-treated in gold and inconel. All other parameters are identical. The highest crystallinity was obtained with the gold crucible and the lowest with the inconel. Alumina showed approximately the same results as gold, but as there is more diffusion of lithium into alumina than in gold, gold was chosen for all standard heat-treatments. Overall, the difference is not astonishingly significant, but still plays a role in the final quality of the glass-ceramics obtained, when considered in addition to the other factors.

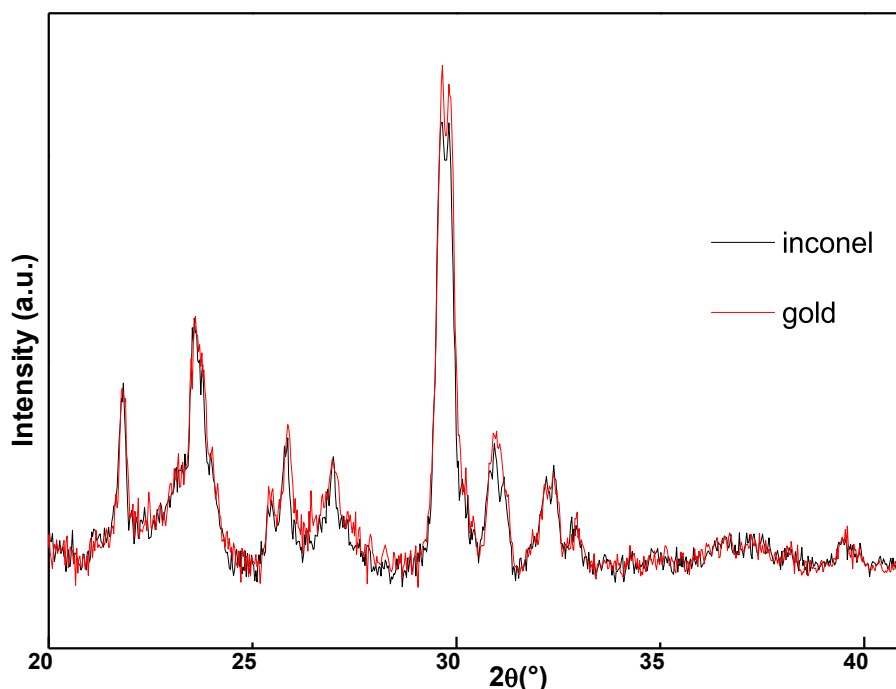


Figure 21: XRD patterns of heat-treated glasses in (a) an inconel crucible and (b) a gold crucible.

3.2.2.9 Atmosphere

The atmosphere in which the heat-treatment is performed also affects the crystallization of the material. Some heat-treatments were performed in an inert argon atmosphere, under an argon flow or under vacuum. Given its higher thermal conductivity coefficient, argon resulted in better crystallizations than vacuum. For the same reason, a static atmosphere was preferred to a flow of colder argon in the furnace.

3.2.2.10 Conclusions on the influence of synthesis parameters

From the various experiments and the study of the different parameters, a preferential method of synthesis has emerged. First, ball milling has proven to be simpler more efficient than quenching for the preparation of the 70.Li₂S-30.P₂S₅ glasses. All milling jars and balls were zirconium oxide. The best results were obtained using a large number of small grinding balls, and with higher milling speeds for shorter milling times (the round milled at 900 rpm for 30 min resulted in higher crystallization of Li₇P₃S₁₁ than the round milled at 400 rpm for 22 h). For the synthesis of Li₇P₃S₁₁

glass-ceramics, the highest degree of crystallization was obtained in an inert argon atmosphere, in gold crucibles, and at temperatures slightly below the decomposition temperature of $\text{Li}_7\text{P}_3\text{S}_{11}$ into $\text{Li}_4\text{P}_2\text{S}_6$ and Li_3PS_4 . To obtain pure $\text{Li}_7\text{P}_3\text{S}_{11}$ it is critical to rapidly cool the sample after heat-treatment to stabilize this metastable high-temperature phase. Compromises between the holding time, the heating rate, the amount of material and the material-form are needed in order to optimize the quality of the obtained $\text{Li}_7\text{P}_3\text{S}_{11}$.

3.2.3 Ionic conductivity measurements

To determine if an ionic conductor will be a good solid electrolyte, impedance analysis is performed. From impedance measurements, the ionic conductivity of the material can be calculated, and if measured at different temperatures, the activation energy can be determined as well. Other information (e.g. polarization) can be obtained if the analysis is conducted on full cells. A good solid electrolyte must have the ability to conduct Li^+ ions with a low activation energy and a low degree of polarization.

Three samples were prepared for impedance analysis. The first material was 70. Li_2S -30. P_2S_5 milled glass **(a)**. The second sample is $\text{Li}_7\text{P}_3\text{S}_{11}$ glass-ceramics powder (obtained by heat-treating glasses in a powder-form) **(b)**. These two powders were then pelletized and placed in a polycarbonate cylinder between two stainless steel blocking current collectors. The third sample is also a $\text{Li}_7\text{P}_3\text{S}_{11}$ glass-ceramic, but this sample was heat-treated in pellet-form in a ceramic cylinder, and the impedance measurement was carried out directly in the cylinder (the material kept its original pellet form) **(c)**. After impedance measurement, the three pellets were crushed and analyzed by XRD (**Figure 22**). The glasses showed a nearly amorphous pattern with very small nuclei of $\text{Li}_7\text{P}_3\text{S}_{11}$. The glass-ceramics exhibited the $\text{Li}_7\text{P}_3\text{S}_{11}$ phase pattern, but the glass-ceramic synthesized in a powder-form is about twice as crystalline as the sample prepared in a pellet-form. This result agrees with the results presented in the previous section (compressed samples need a longer holding time to achieve same degree of crystallization as a powdered sample).

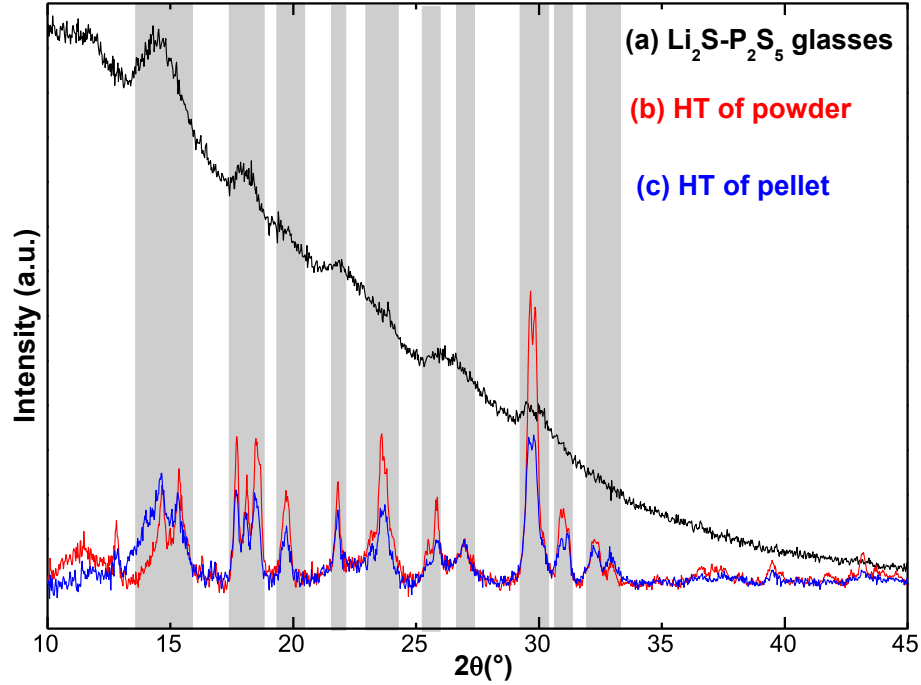


Figure 22: XRD patterns of (a) 70.Li₂S-30.P₂S₅ milled glasses, and of Li₇P₃S₁₁ crystallized in a (b) powder-form, and (c) pellet-form.

Figure 23 shows the Nyquist plots for the three samples. The data is not normalized by the thickness of the pellet so the resulting ionic conductivities are presented in

Table 2 (as we have $= \frac{\text{thickness}}{\text{Resistance} \cdot \text{Surface area}}$). Anyway, the pellets thicknesses are all in the range of 500-700 μm. The Li₂S-P₂S₅ glass shows a partial semi-circle at high frequencies, followed by a linear portion at low frequencies. The two glass-ceramics exhibit only the linear part. These results are typical for sulfide glasses, in which the grain boundary resistance is not high enough to appear in the plots at room temperature. When temperature is decreased, the resistances (bulk, grain boundary and interfaces) increase and three semi-circles would appear at high frequency for the glass-ceramics⁵⁵⁻⁵⁶. For the plot with a semicircle (as for the glasses presented in **Figure 23**), the data can be fitted by an equivalent circuit to calculate the overall resistance and the bulk-conductivity. For data without semi-circles, the overall resistance of the electrolyte can be extrapolated from the linear portion to the x-axis in the Nyquist plot or from the Bode plot (log(|Z|) as a function of log(frequency)). The values are presented in

Table 2.

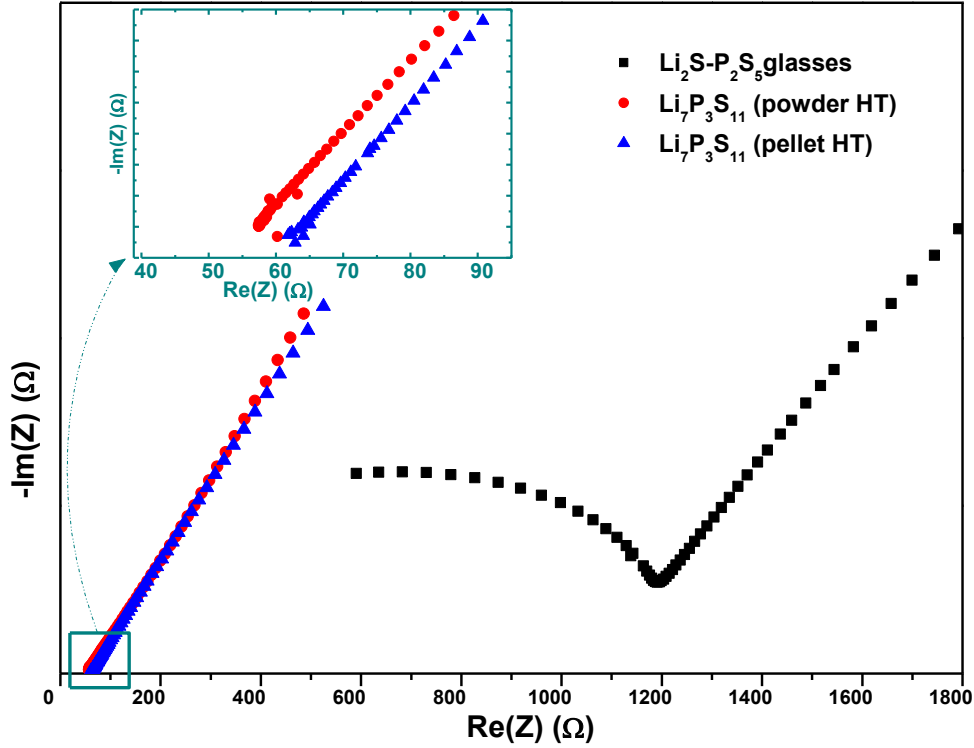


Figure 23: Nyquist plots of (a) $\text{Li}_2\text{S-P}_2\text{S}_5$ glasses, (b) $\text{Li}_7\text{P}_3\text{S}_{11}$ prepared in a powder-form and (c) $\text{Li}_7\text{P}_3\text{S}_{11}$ prepared in a pellet form, measured at room temperature.

Sample	Total electrolyte resistance (Ω)	Thickness of pellet (cm)	Ionic conductivity (S/cm)
$\text{Li}_2\text{S-P}_2\text{S}_5$ glasses	1200	0.064	$6.79 \cdot 10^{-5}$
$\text{Li}_7\text{P}_3\text{S}_{11}$ (powder HT)	57.5	0.054	$1.20 \cdot 10^{-3}$
$\text{Li}_7\text{P}_3\text{S}_{11}$ (pellet HT)	63.1	0.067	$1.35 \cdot 10^{-3}$

Table 2: Ionic conductivity of $\text{Li}_2\text{S-P}_2\text{S}_5$ glasses and glass-ceramics.

The glasses have an ionic conductivity of 10^{-5} - 10^{-4} S/cm, which is typical for sulfide glasses. Despite its lower degree of crystallinity, the sample heat-treated directly in the impedance cell as a pellet has a higher ionic conductivity than the glass-ceramics heat-treated in a powder-form and pelletized afterwards in the impedance cell. This is due to reduction in grain boundary resistance.

3.2.4 Conclusion and perspectives

The synthesis of $\text{Li}_7\text{P}_3\text{S}_{11}$ remains very difficult even after over a year of research. Every round of glasses and every heat-treatment is different and behaves in a different way. Treatments that would achieve the highest crystallinity and conductivity for one round would result in low crystallinity and poor performance for another one. Because of this, each round of glasses has to be analyzed by DSC, and multiple heat-treatments must be performed to determine the optimum $\text{Li}_7\text{P}_3\text{S}_{11}$ synthesis method for each batch. This is why upscaling is currently not an option. Despite this, a method has been created to produce satisfactory glass-ceramics for use in all-solid-state batteries. First, higher crystallinity is achieved when nuclei or crystals of $\text{Li}_7\text{P}_3\text{S}_{11}$ are already present in the glasses. This is done either by using high milling speeds, or by conducting an extensive study of nuclei and crystal growth rates followed by heat-treatments in several steps⁵⁷⁻⁵⁸. Furthermore, it has been shown that degree of crystallinity is not the only important factor when using $\text{Li}_7\text{P}_3\text{S}_{11}$ as a solid electrolyte, as was also shown in literature⁵⁹. The reduction of grain boundary resistance is just as important as degree of crystallinity, if not more so, as the impedance results showed. Significant progress has been made on the synthesis of $\text{Li}_7\text{P}_3\text{S}_{11}$, and a method to obtain a reasonably conductive solid electrolyte that can be used in batteries was determined.

3.3 Na₂S-P₂S₅ glasses

3.3.1 Introduction

The Na-P-S system has attracted special interest since the discovery of the Li₇P₃S₁₁ phase in 2008⁵⁹. In fact, as the X₇P₃S₁₁ superionic conducting phase is present in both the Ag-P-S (discovered in the 1980's⁶⁰) and the Li-P-S systems, there is a chance that the Na₇P₃S₁₁ phase exists as well. The hunt for it has been unsuccessful so far despite investigations and publications made by Martin and Hayashi's groups in particular. Other sodium ionic conductors were discovered in the process: for instance a cubic form of Na₃PS₄, which has an ionic conductivity two orders of magnitude higher than its tetragonal counterpart⁶¹.

In this section, attempts to synthesize Na₇P₃S₁₁ from 70.Na₂S-30.P₂S₅ glasses are presented. Investigation of the phases forming in the 67.Na₂S-33.P₂S₅ glasses gave rise to the discovery of two "new unknown" structures.

3.3.2 70-30 Na₂S-P₂S₅ glasses

We first tried to synthesize Na₇P₃S₁₁ in the traditional way used for Li₇P₃S₁₁. Similar to Li₂S-P₂S₅ glasses, reagent grade Na₂S and P₂S₅ were mixed in a 70:30 molar ratio, and ball milled in a ZrO₂ jar at 400 rpm. Two different experiments are presented here. In the first, the mixture was milled for 10 h (in literature the milling time is typically at least 20 h) and the second experiment for 30 min. The resulting materials were analyzed by XRD and DSC techniques.

Figure 24 compares X-ray diffraction patterns of the two glass samples. The sample milled for 10 hours shows small peaks of Na₃PS₄ while the sample milled for 30 min is completely amorphous. This demonstrates that the Na-P-S system is considerably more sensitive to heating from the ball milling step, compared to the Li-P-S system. Na₃PS₄ tends to form very easily from the glasses compared with its cousin (Li₃PS₄) in the Li-P-S system.

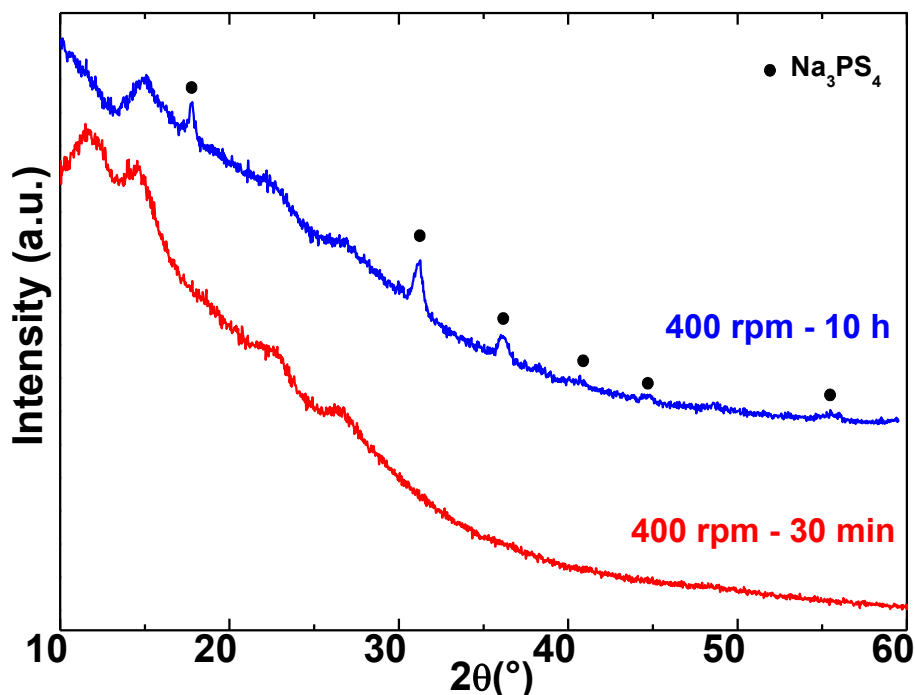


Figure 24: XRD patterns of 70-30 Na₂S-P₂S₅ glasses milled at 400 rpm for 10 hours and 30 min respectively.

Following these results, DSC analysis was carried out on the round of glasses milled for 30 min, which were amorphous. The heat-flow curve is displayed in **Figure 25**. The material was heated in the DSC up to 500 °C at a heating rate of 10 °C/min. The curve exhibits two exothermic peaks at 211°C and 235°C, an endothermic peak at 350°C, and a barely visible exothermic peak at 384°C. In our type of materials, exothermic peaks are usually characteristic of crystallization and endothermic peaks of melting. The glasses were consequently heat-treated according to those thermal changes. Heat-treatments of the other round of glasses milled for 10 h only resulted in further crystallization of Na₃PS₄ so no further investigation was conducted.

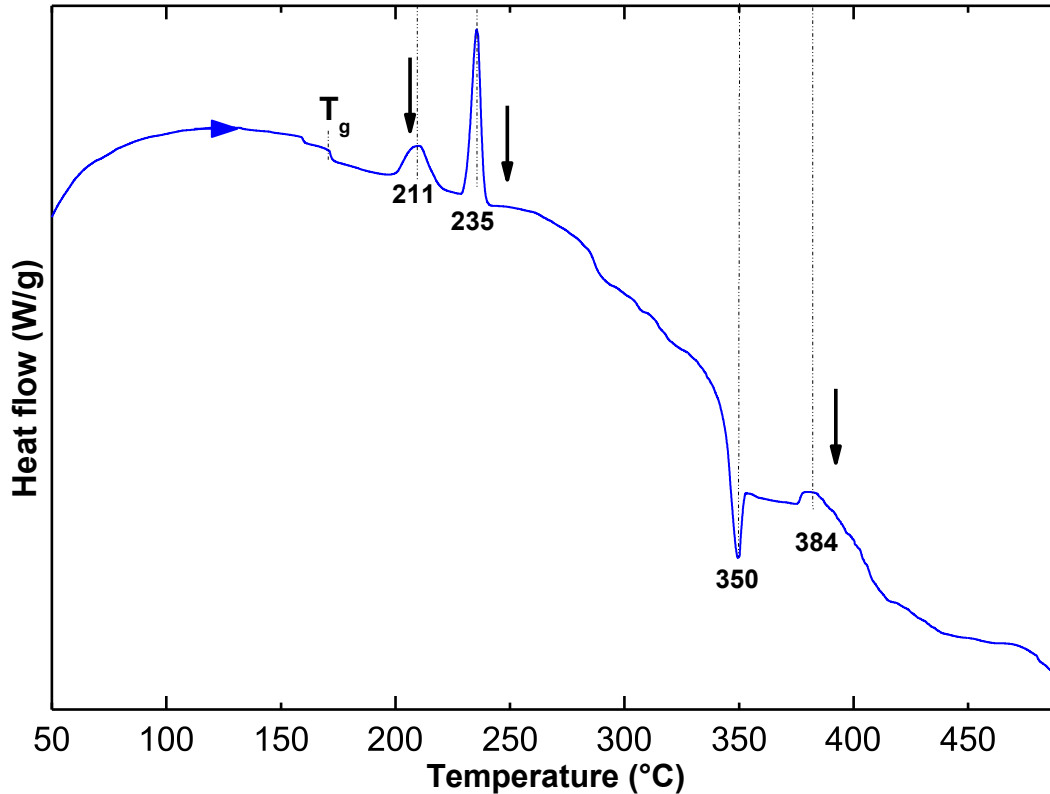


Figure 25: DSC curve of the 70-30 Na₂S-P₂S₅ glasses milled at 400 rpm for 30 min.

The glasses were heat-treated at 210, 250, and 390°C respectively (as indicated by the arrows in **Figure 25**). The samples were placed into quartz tubes, sealed under vacuum, heated up to the different temperatures, held for 1 h, and then quenched in an ice bath to stabilize the composition obtained at the different temperatures. **Figure 26** shows the XRD patterns of the heat-treatments. The heat-treatment at 210°C, corresponding to the first exothermic peak, exhibits only small peaks of Na₃PS₄. At 250°C (after the second exothermic peak), the Na₃PS₄ peaks are more intense than for the 210°C heat-treatment, and an unknown phase appears. After heat-treatment at 390°C (after the melting point), XRD results show only Na₃PS₄ remains with a higher degree of crystallinity. These results strongly suggest that at 211°C, Na₃PS₄ crystallizes from the amorphous glasses; at 235°C, the unknown phase crystallizes as well from the remaining amorphous glasses; and at 350°C, the unknown phase melts, leaving Na₃PS₄ crystals and an amorphous melt composition in the sample.

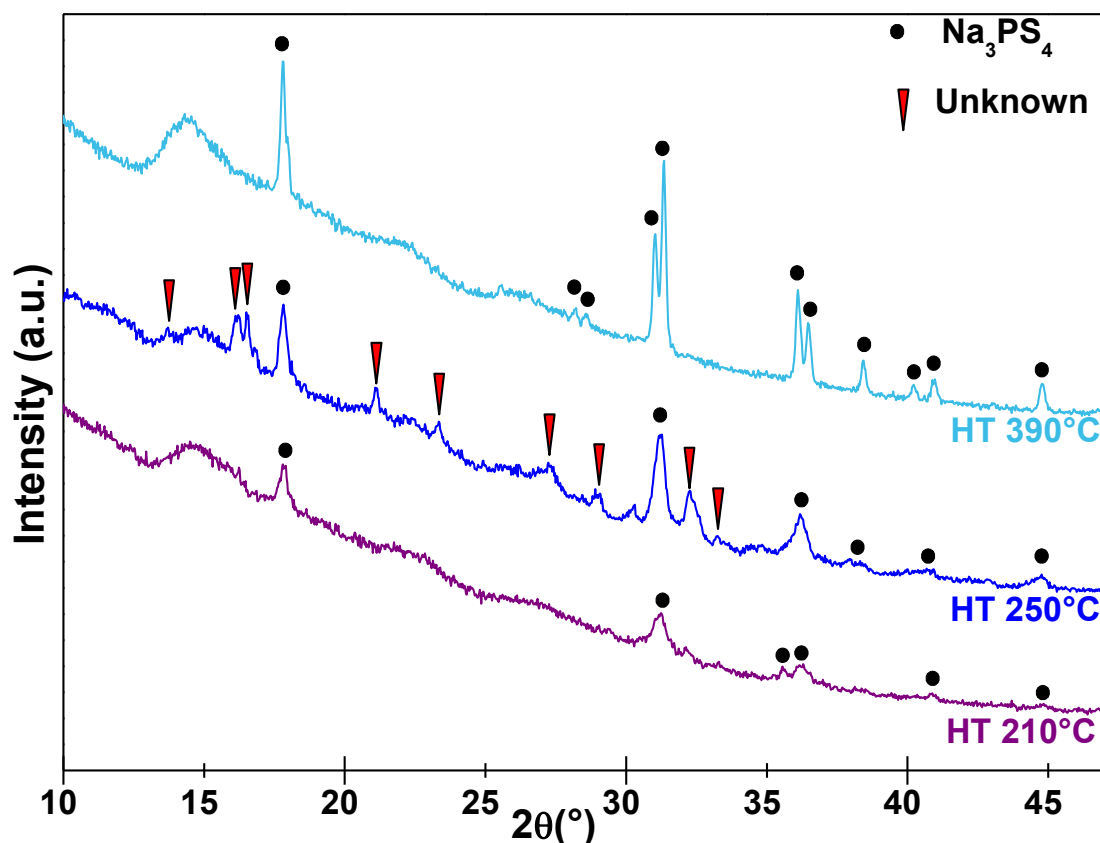


Figure 26: XRD patterns of 70. Na₂S-30.P₂S₅ glasses heat-treated and quenched at 210°C, 250°C and 390°C respectively.

The unknown phase is not reported in any XRD database, but further investigation into literature suggests that it could be crystalline Na₄P₂S₇. In particular, Hayashi et al. published very similar XRD patterns of this phase in 2014, which was attributed to crystalline Na₄P₂S₇, but this was never verified⁶². Thus, glasses in the molar ratio 67-33 (stoichiometry of Na₄P₂S₇) were prepared.

3.3.3 67.Na₂S-33.P₂S₅ glasses

To synthesize the 67.Na₂S-33.P₂S₅ glasses, Na₂S and P₂S₅ were mixed in a 67:33 molar ratio, placed into ZrO₂ jars and mechanically milled at 400 rpm for 30 min. XRD was used to verify that the material was amorphous. **Figure 27** shows the DSC curve of the 67.Na₂S-33.P₂S₅ glass, which exhibits an exothermic peak at 226°C, two endothermic peaks at 350°C (the same as for the 70-30 glasses) and at 423°C upon heating to just below 500°C, and an exothermic peak at 315°C upon cooling down.

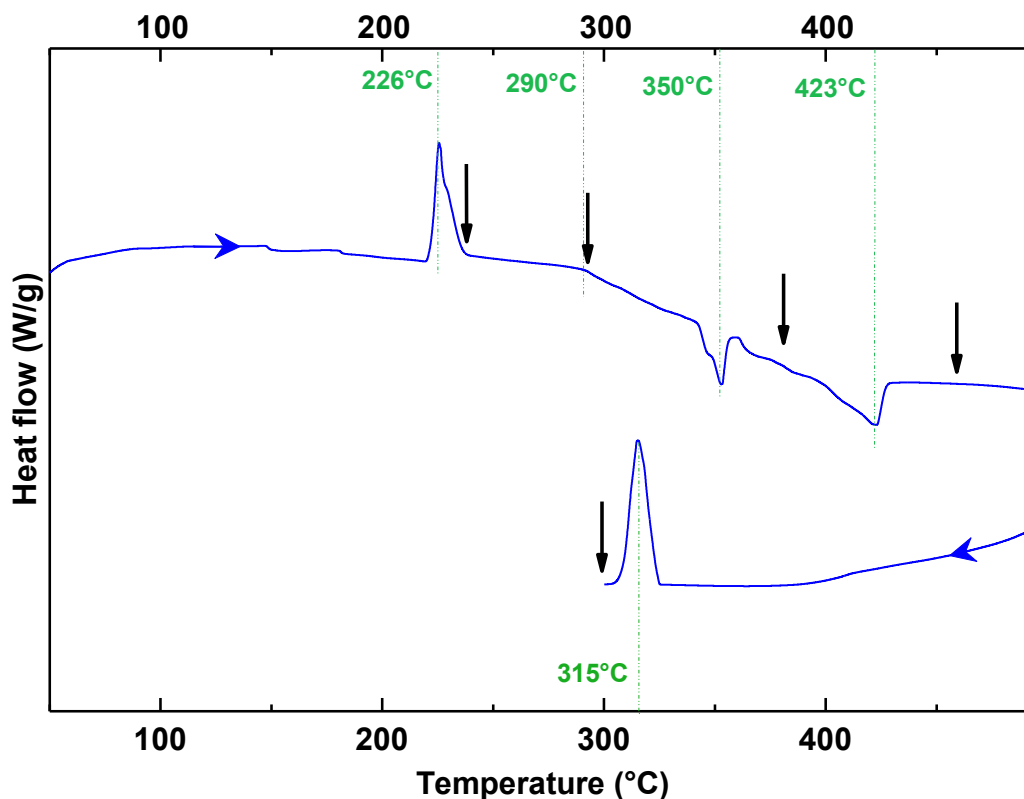


Figure 27: DSC curves of 67.Na₂S-33.P₂S₅ glasses milled at 400 rpm.

Heat-treatments were performed at the temperatures denoted by black arrows in **Figure 27**, which are just beyond the exo- or endo-thermic features. The glasses were placed in a powder form in a gold crucible and placed in a hot furnace set at the selected temperature, held for 1 h, and then cooled to room temperature (under argon) external to the furnace. **Figure 28** shows the XRD patterns of the heat-treated samples at 230, 290, 375, and 455°C, as well as a sample heated up at 470°C, cooled down and held at 300°C (arrow in the cooling curve). The sample heat-treated at 230°C exhibits peaks corresponding to Na₃PS₄ and the unknown phase previously observed in the 70-30 system (unknown 1). Heat-treatment at 290°C resulted in further crystallization of the unknown phase 1, where the ratio of Na₃PS₄ to unknown 1 is decreased. At 375°C, after the melting point, the unknown phase 1 did not disappear as expected (according to previous studies on the 70-30 system, the unknown phase 1 crystallizes around 230°C and melts at 350°C). This could be because the sample was not quenched at the end of the heat-treatment but simply cooled down at room temperature. Thus, unknown 1 had time to recrystallize. At 455°C, after the second melting point, the sample became amorphous, which suggests that both the Na₃PS₄ and unknown phase 1 have melted.

Finally, the glasses heated up to 470°C (to the melt) and then held at 300°C, exhibited a second unknown (unknown 2) in the diffraction pattern.

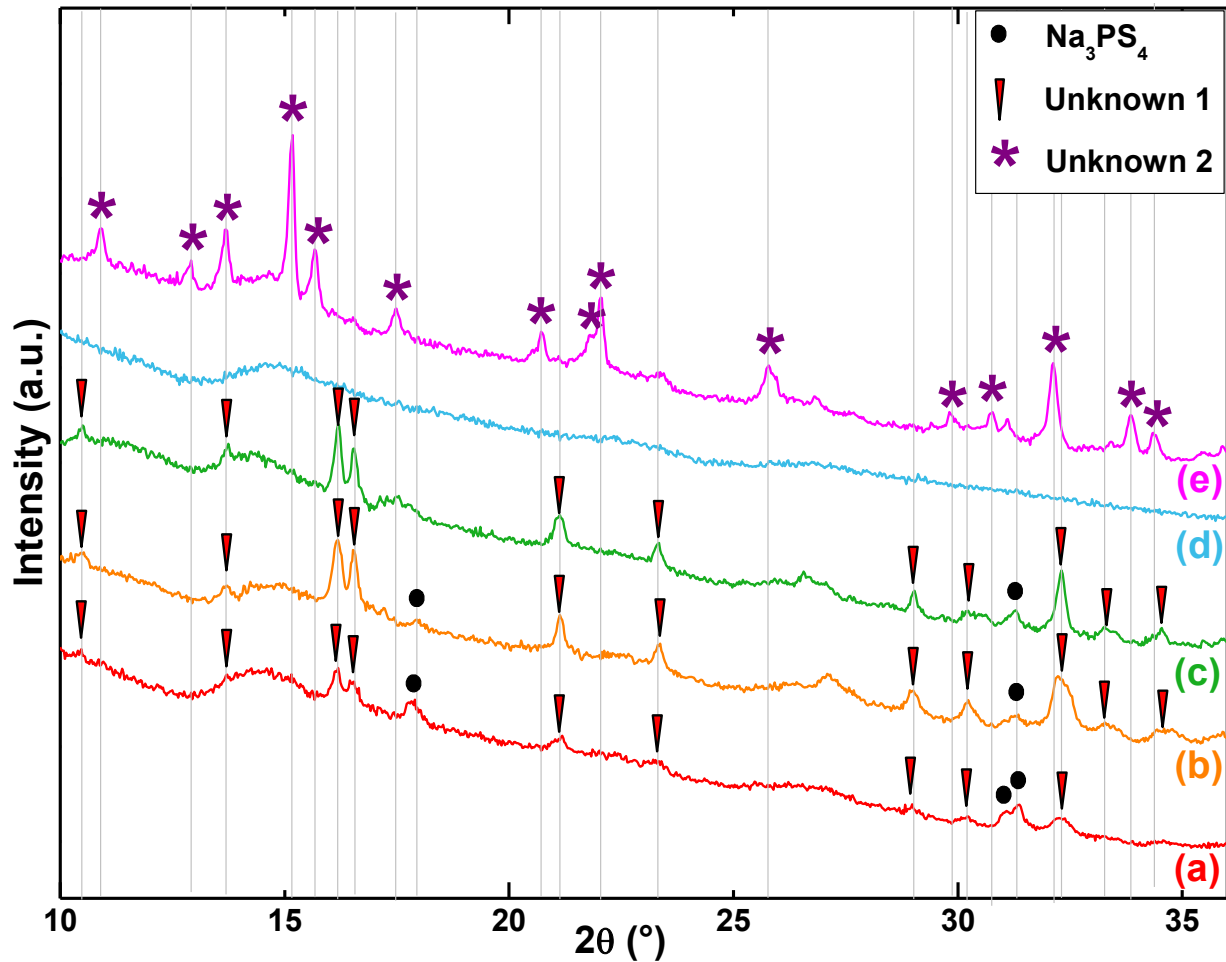


Figure 28: XRD patterns of 67-33 glasses after heat-treatment at (a) 230°C, (b) 290°C, (c) 375°C, (d) 455°C, and (e) 470-300°C.

Figure 29 shows the Raman spectra of the materials (c) heat-treated at 375°C (i.e. of the unknown phase 1), (d) heat-treated at 455°C (i.e. of the composition of the melt), and (e) heat-treated at 470°C and then cooled and held at 300°C (HT 470-300°C) (i.e., unknown phase 2). The spectra exhibit identical features but with differing intensities. The higher the temperature of the heat-treatment, the more intense are the Raman peaks. The most identifiable peaks are the main band at 400 cm^{-1} and a very low intensity band at 380 cm^{-1} , which can be assigned to $\text{P}_2\text{S}_7^{4-}$ and $\text{P}_2\text{S}_6^{4-}$ ions respectively, according to the literature about Raman studies of the lithium thiophosphates. **Table 3** below summarizes all the Raman peaks frequencies and intensities, comparing them with data from the literature. The peaks matching perfectly are highlighted in yellow. The peaks that were not

comparable are highlighted in grey, and the peaks that were missing or extra are in red. Finally very weak peaks that are not present in our spectra are left in white, as they could be present. Overall, the spectra of the heat-treated materials match almost perfectly the referenced spectra of $\text{Na}_4\text{P}_2\text{S}_7$, confirming our previous hypothesis. Although the unknown phases 1 and 2 have very distinct diffraction patterns, the Raman results suggest that they might be $\text{Na}_4\text{P}_2\text{S}_7$ polymorphs.

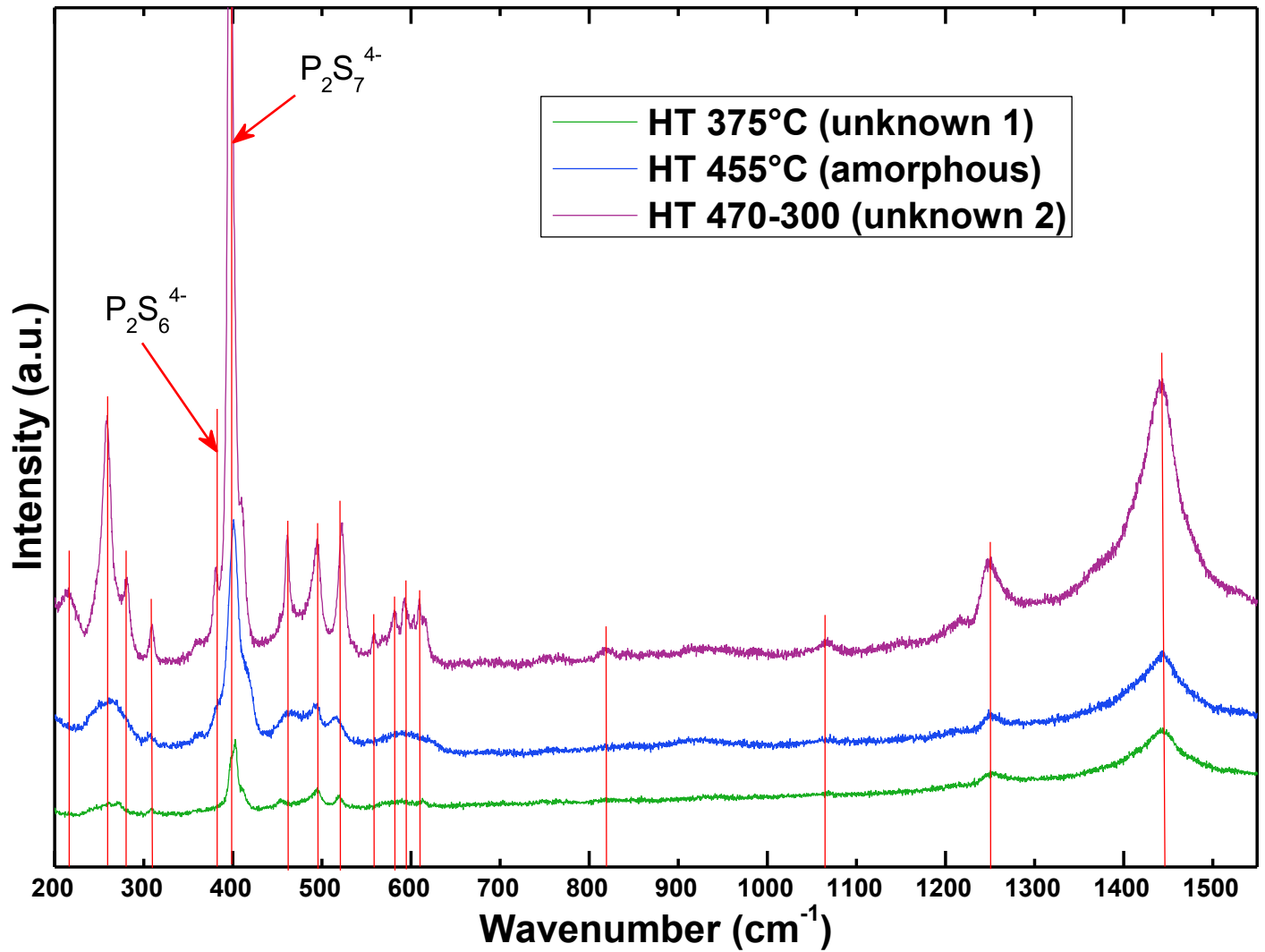


Figure 29: Raman spectra of the 67-33 Na glasses after heat-treatment at 375°C, 455°C, and 470-300°C.

Peak frequency for HTs (cm ⁻¹)	Peak frequency for Na ₄ P ₂ S ₇ (literature) ⁶³ (cm ⁻¹)
	183 m
215 w	215 vw
	230 vw
249 wsh	248 wsh
259 s	260 s
281 m	280 m
310 w	310 vw
380 wsh	n.p.
398 vs	398 vs
410 msh	410 msh
n.p.	435 s
462 s	462 s
495 s	n.p.
523 s	524 s
	540 vw
582 w	583 w
594 w	595 w
610 w	610 w
n.p.	650 m
819 vw	
1065 vw	
1251 m	
1443 sb	

Table 3: Comparison of peaks frequencies and intensities of the Raman spectra of the heat-treated materials. w weak, m: medium, s: strong, v: very, b: broad, sh: shoulder, n.p. : not present

3.3.4 Characterization of the unknown phases

Impedance measurements were performed on (a) the precursor 70-30 Na glasses, (b) a mixture of Na₃PS₄ and unknown phase 1 (heat-treatment of the 70-30 glasses at 250°C), (c) the precursor 67-33 Na glasses, (d) the unknown phase 1 (heat-treatment at 375°C was the most crystalline), and (e) the unknown phase 2 (heat-treatment at 470 and then 300°C). The different ionic conductivities at room temperature are reported in **Table 4**.

Material	Ionic conductivity at room temperature (S/cm)
(a) 70.Na ₂ S-30.P ₂ S ₅ glasses	7.35 10 ⁻⁷
(b) Na ₃ PS ₄ + unknown 1	1.01 10 ⁻⁵
(c) 67-33 Na ₂ S-P ₂ S ₅ glasses	1.10 10 ⁻⁶
(d) Unknown 1 (HT 375°C)	5.30 10 ⁻⁷
(e) Unknown 2 (HT 470-300°C)	6.50 10 ⁻⁷

Table 4: Comparison of the ionic conductivity of different sodium glasses and glass-ceramics

The XRD patterns of both unknown phases were indexed in the P-1 space group.

For unknown phase 1, the lattice parameters are a=5.48 Å, b=6.54 Å, c=8.65 Å, α=96.2°, β=80.5°, and γ=84.8°.

For unknown phase 2, the best matches were for a=5.88 Å, b=5.00 Å, c=8.13 Å, α=86.6°, β=97.8°, and γ=92.4°.

These lattice parameters are somewhat similar, which comforts the hypothesis of polymorph materials. **Figure 30** and **Figure 31** show LeBail fits of the patterns.

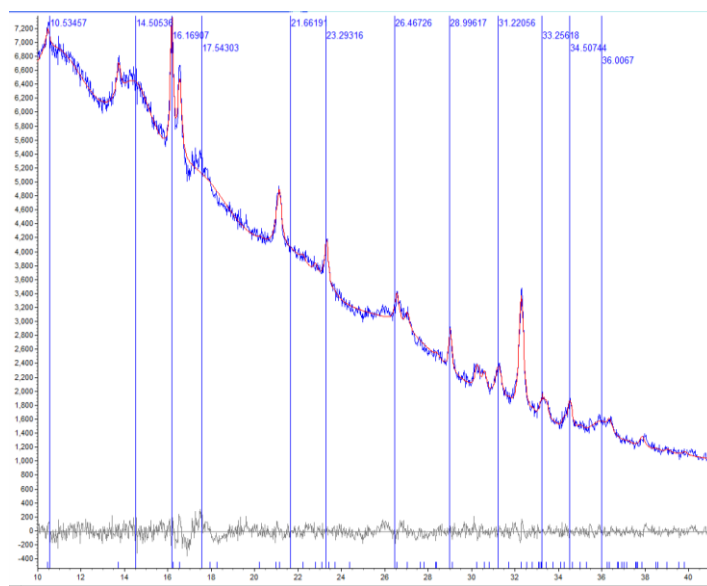


Figure 30: LeBail fit of the XRD pattern of the unknown phase 1.

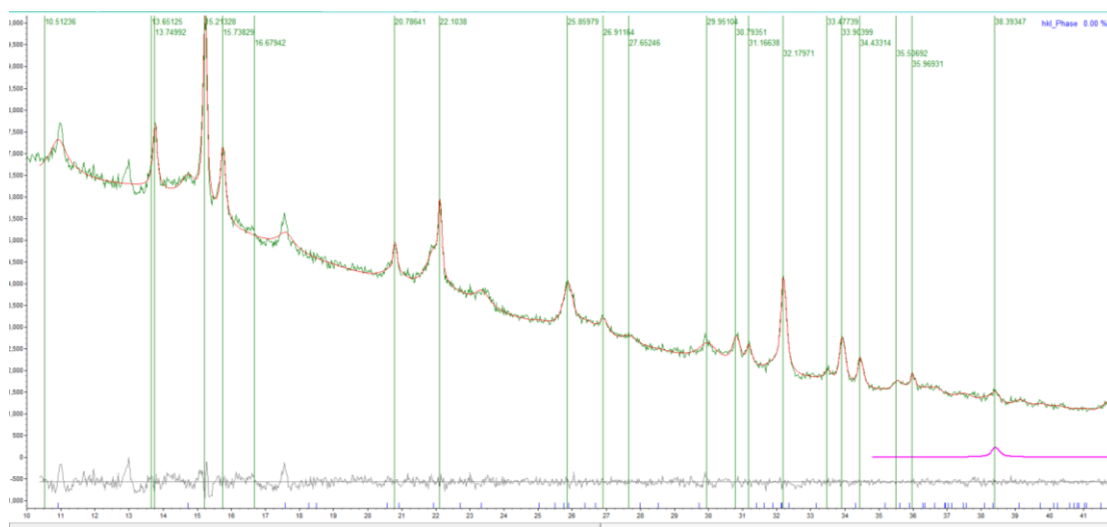


Figure 31: LeBail fit of the XRD pattern of the unknown phase 2.

3.3.5 Conclusion and future studies:

The investigation in the 70-30 and 67-33 $\text{Na}_2\text{S-P}_2\text{S}_5$ glasses uncovered two never reported crystalline structures. Although the crystalline structures were never published, DSC and Raman analyses support our hypothesis that these phases are in fact polymorphs of the structurally undefined

$\text{Na}_4\text{P}_2\text{S}_7$ phase. The two materials exhibited low ionic conductivities of about 5×10^{-7} S/cm. More characterization must be performed to verify this hypothesis. The materials need to be synthesized in a more pure form to definitely establish their structure.

3.4 Na-Li hybrid glasses

As reported in the previous section we did not succeed in synthesizing the $\text{Na}_7\text{P}_3\text{S}_{11}$ phase via solid-state route by planetary ball milling. However, we observed that for the Li-P-S system, once some nuclei of the $\text{Li}_7\text{P}_3\text{S}_{11}$ phase are present, the formation of the “7-11” structure with high purity and high degree of crystallization is favored (cf section 3.1). In this perspective, we have attempted to mix amorphous 70. Na_2S -30. P_2S_5 glasses with partially crystalline $\text{Li}_7\text{P}_3\text{S}_{11}$ glass-ceramics, in different weight ratios. As a result, a new hybrid Na-Li phase was formed, then determined by *ab initio* structure solution using Topas™, and characterized by impedance spectroscopy, SEM/EDX and Raman spectroscopy.

3.4.1 Experimental

Synthesis of the 70. Na_2S -30. P_2S_5 glasses and of the 70. Li_2S -30. P_2S_5 glass-ceramics

Reagent grade Na_2S (Alfa, purity 99%) and P_2S_5 (Aldrich, purity 99.9%) in a molar ratio of 70:30 were used as starting materials. The Na glasses were prepared by a mechanochemical method using a planetary ball mill apparatus (PULVERISETTE 7 Premium, Germany). The materials were milled together in a 45 mL Zirconia jar at 500 rpm for 30 min (section 3.2.1). Similarly, the mechanochemical treatment was performed for a 70:30 molar ratio mixture of Li_2S (Alfa, purity 99.9%) and P_2S_5 , and glass-ceramics were obtained after milling at 900 rpm for 1 h (see section 3.1). X-Ray diffraction (XRD) was performed to verify the crystallinity of the obtained glasses and DSC to determine the crystallization temperatures and other thermal behaviors.

Preparation of the hybrid Na-Li glasses

The precursors, the Na glasses and the Li glass-ceramics were weighed in different weight ratios (90:10, 60:40, 50:50, and 40:60) and ground together in a mortar. Each mixture was put into a 13 mm die and a pressure of 3 tons was applied at 25°C for 30s using a hydraulic press. The pellets were then heat-treated at 170°C (softening temperature of the Na glasses) for 3 h. The 60:40 ratio material was further heat-treated at 260°C, 330°C and 375°C. Again, XRD and DSC were performed to investigate the structure and thermostability of the obtained materials.

3.4.2 Results and discussion

Figure 32 shows the XRD patterns of the Na glasses, the $\text{Li}_7\text{P}_3\text{S}_{11}$ glass-ceramics, and the different hybrids. The structures change after pre-heat-treatment at 170°C . The 90:10 ratio of Na glasses/ $\text{Li}_7\text{P}_3\text{S}_{11}$ glass-ceramics has crystallized into the thermodynamically stable phase Na_3PS_4 . However, for the 60:40 ratio, a completely new phase is observed that does not match any phase from the database. The 50:50 and 40:60 ratios gave the same result as for the 60:40 phase, but in less crystalline.

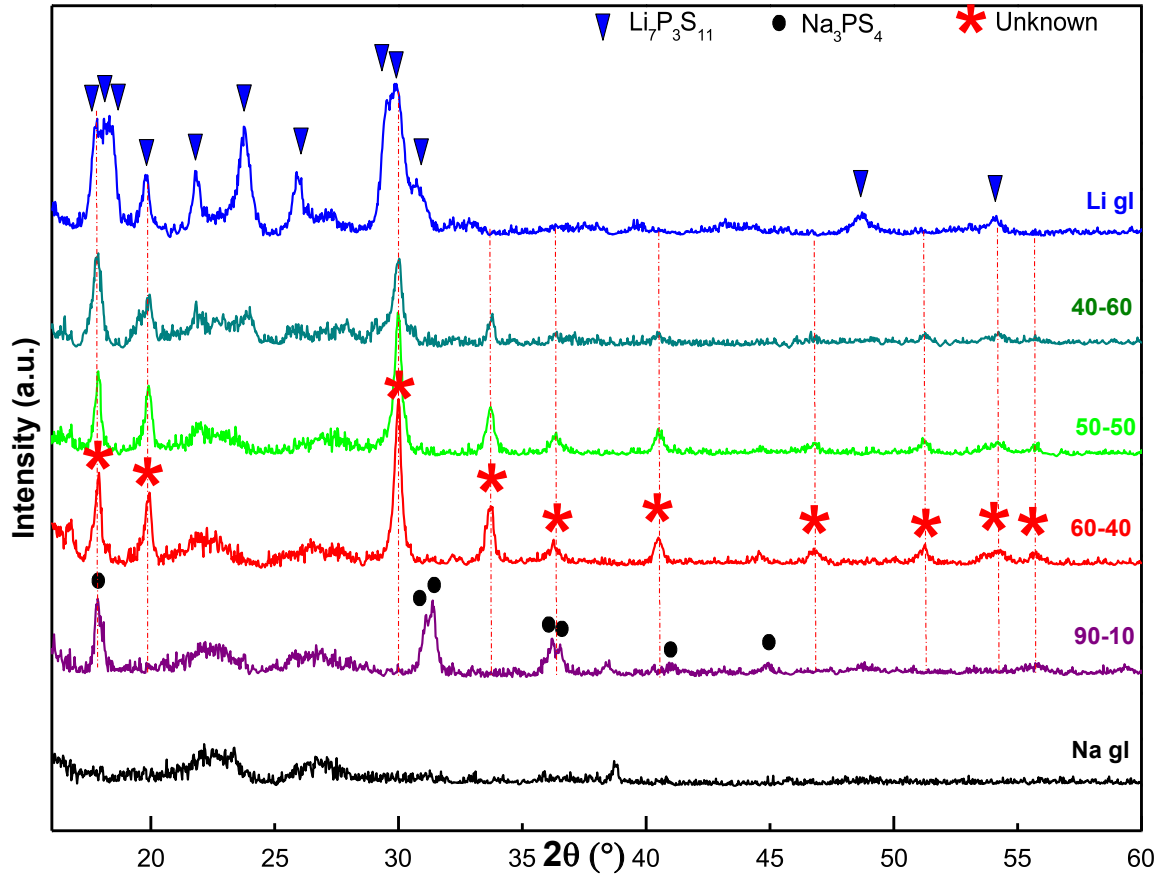


Figure 32 : XRD patterns of $\text{Li}_7\text{P}_3\text{S}_{11}$ glass-ceramics (Li gl), $70.\text{Na}_2\text{S}-30.\text{P}_2\text{S}_5$ glasses (Na gl), and mixtures of both in 90:10, 60:40, 50:50, and 40:60 weight ratios.

Following these results, DSC was performed on the different samples, in order to crystallize more of the unknown phase and to enable the identification of its structure. The results are presented in **Figure 33**. The Na glasses present the same features of crystallization of Na_3PS_4 and the unknown phase 1 around 223°C as presented in section 3.2. Similarly the Li glass-ceramics show exothermic peaks at 313°C and 390°C , corresponding to the crystallization of Li_3PS_4 and $\text{Li}_4\text{P}_2\text{S}_6$, respectively. The hybrid samples have very different features from the precursors. Despite the 60:40 and 50:50

ratios having almost identical XRD patterns, their DSCs are very different. The 60-40 ratio has two small exothermic peaks at 258 and 329°C, and an endothermic peak at 374°C. The 50-50 wt% ratio shows exothermal change at 236°C and two endothermic peaks at 315°C and 321°C. The 50-50 wt% ratio shows exothermal change at 236°C and two endothermic peaks at 315°C and 321°C.

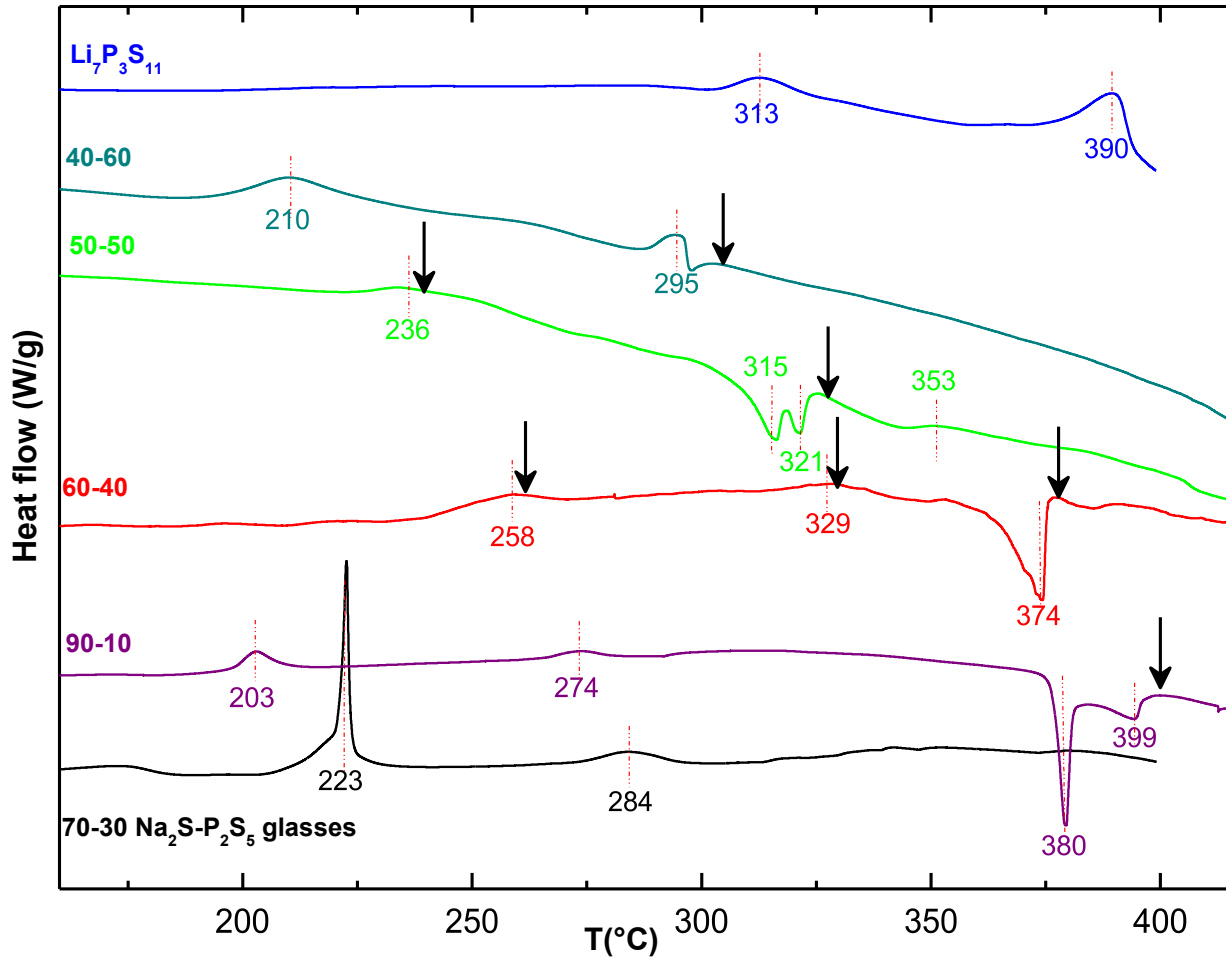


Figure 33 DSC of $\text{Li}_7\text{P}_3\text{S}_{11}$ glass-ceramics, 70. Na_2S -30. P_2S_5 glasses (Na gl), and mixtures of both in 90:10, 60:40, 50:50, and 40:60 weight ratios.

Given that the 60:40 ratio was the most promising in terms of obtaining a single phase, some preliminary heat-treatments were performed at 260°C, 330°C, and 375°C (labeled with arrows in **Figure 33** showing the DSC features). The XRD patterns of the obtained materials are presented in **Figure 34** below.

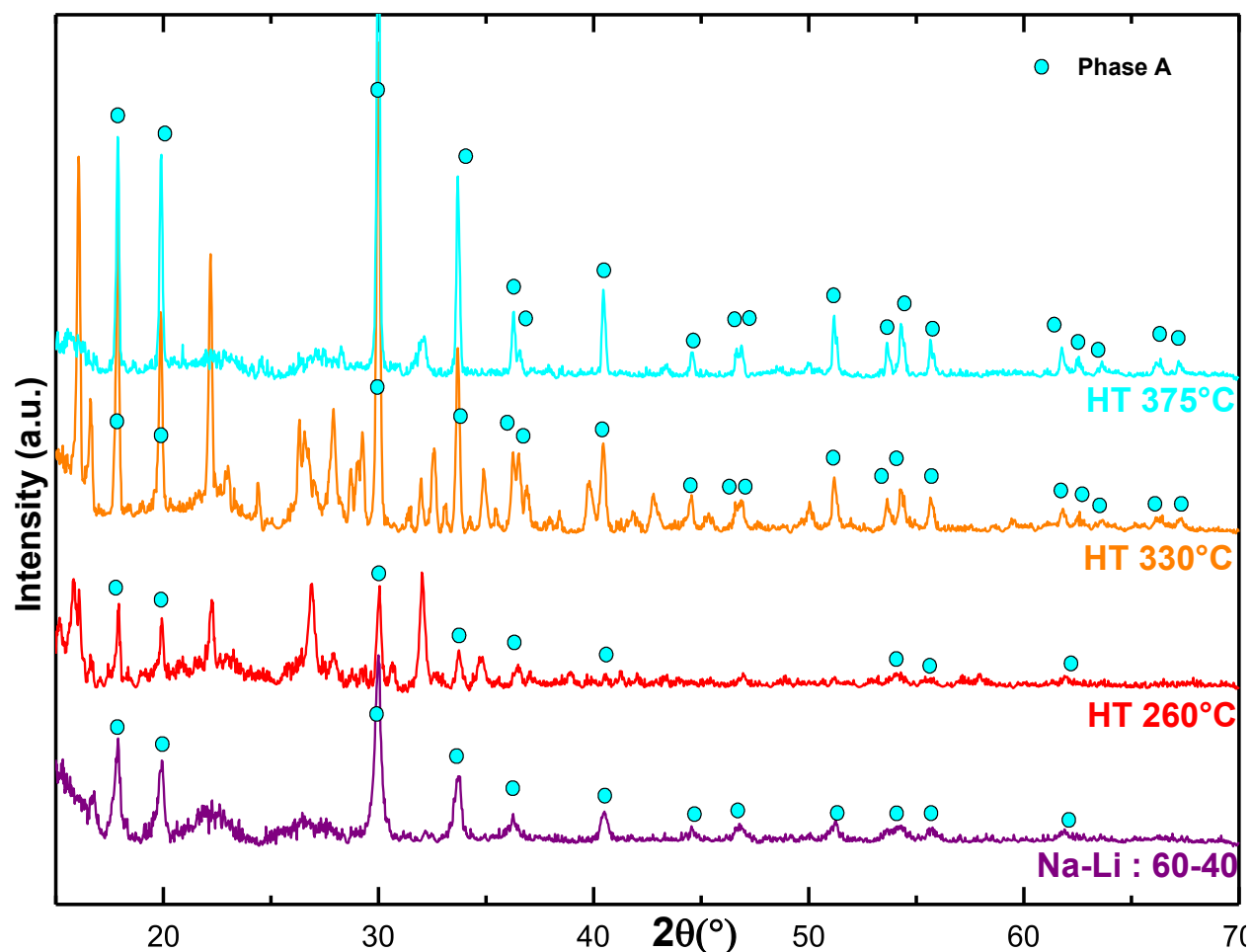


Figure 34 XRD patterns of the hybrid 60:40 Na-Li glasses heat-treated at 260°C, 330°C, and 375°C.

The “Phase A”, present in the pre-heat-treated sample (Na-Li : 60-40 weight %), is found in each sample but is obtained almost pure-phase and highly crystalline in the heat-treatment at 375°C. The other two heat-treatments show multiple unknown peaks, and their number makes it difficult to analyze and determine the single phases among them. The other ratios were also heat-treated at different temperatures, following the arrows on the DSC curves. All heat-treatments resulted in a mixture of the phase A with additional unknown peaks, similarly to the heat-treatments at 260°C and 330°C for the 60-40 wt%, but with no obvious correlation between them.

3.4.3 Characterization of the unknown “phase A”

3.4.3.1 Structure determination

The Phase A was successfully, and definitively indexed to a tetragonal structure in the space group I-42m with the following lattice parameters: $a = 6.3007 \text{ \AA}$ and $c = 8.0026 \text{ \AA}$. After indexing and fitting of the pattern, the structure was determined and the material was found to be Li_2NaPS_4 , which exhibits corner-sharing tetrahedra of PS_4 , NaS_4 and LiS_4 ions (shown in **Figure 35**). The Li^+ ions (in the green tetrahedra) are segregated into 2D layers in the structure as depicted, whereas the Na^+ ions (in the yellow tetrahedra) are in 2a sites that should present little mobility owing to the presence of P^{5+} (as PS_4) in the 2b sites (see **Figure 36**).

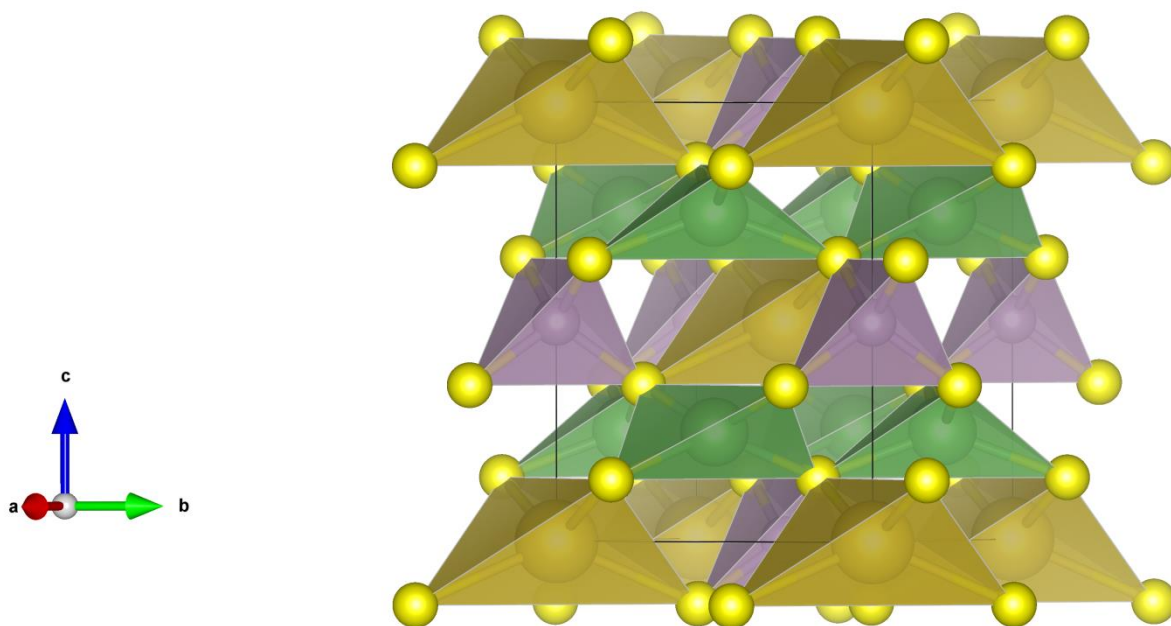


Figure 35: Polyhedral depiction of the unit cell of the Li_2NaPS_4 structure. Purple tetrahedra: PS_4 , yellow tetrahedra: NaS_4 , green tetrahedra: LiS_4 .

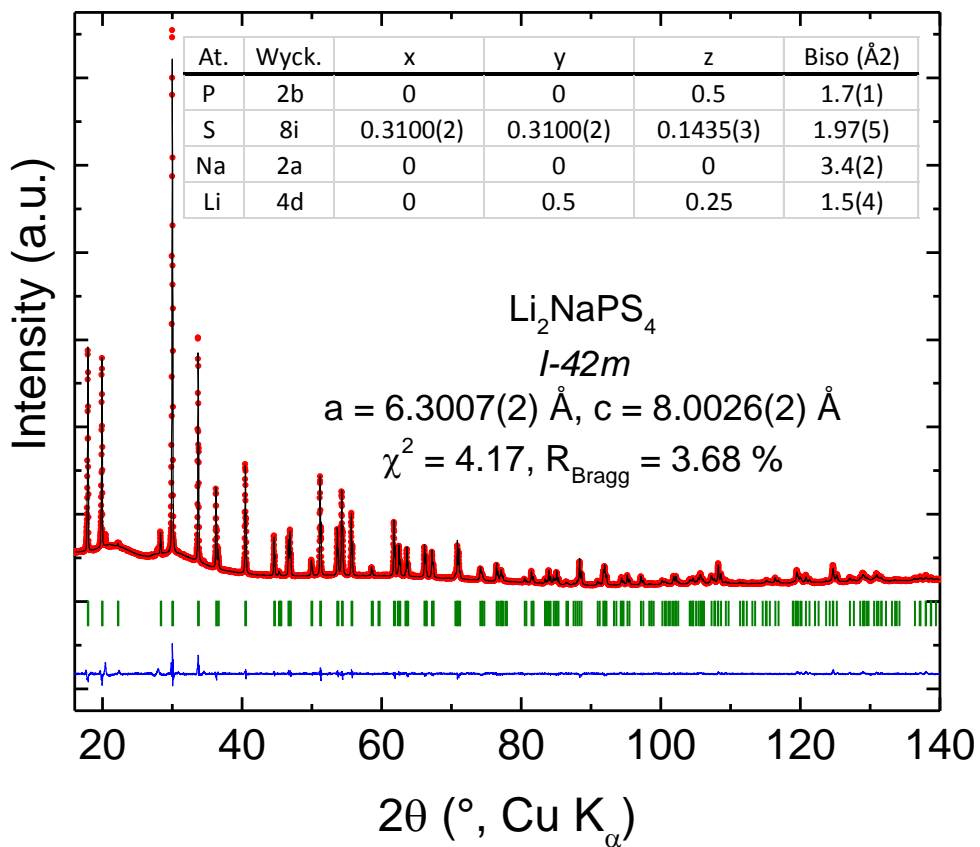


Figure 36: Space group and cell parameters of the Li₂NaPS₄ structure.

3.4.3.2 Impedance measurements

Impedance measurements were performed on Li₂NaPS₄. The Nyquist plot is shown in **Figure 37**.

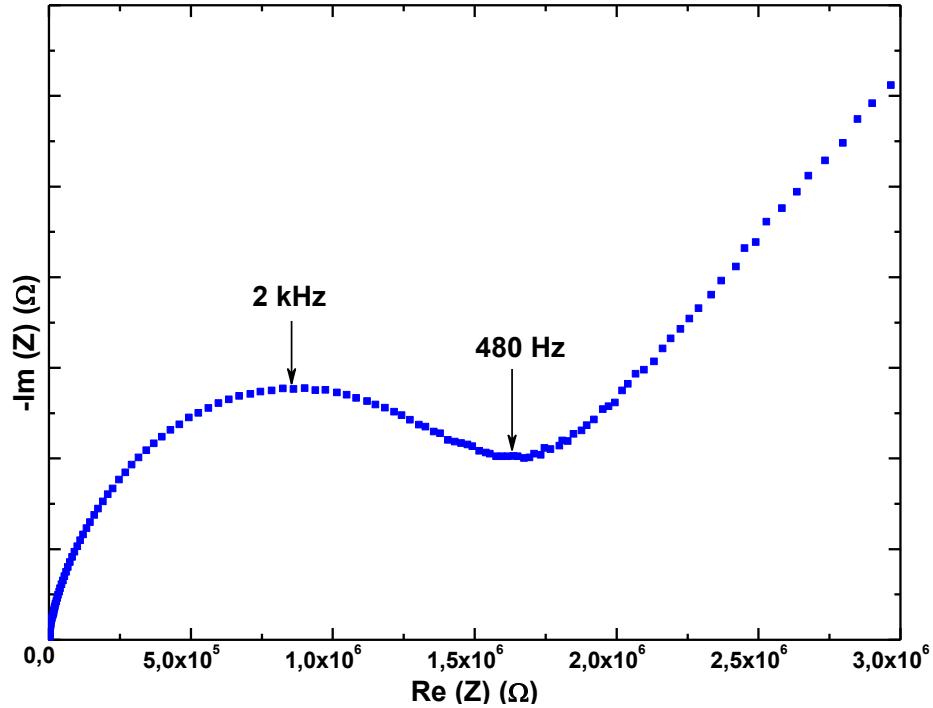


Figure 37: Nyquist plot of Li_2NaPS_4 .

The data was fit by an equivalent circuit of the form: $\frac{Q_1}{R_1 + \frac{Q_2}{R_2} + Q_3}$ (**Table 5**). R_1 corresponds to the bulk, and R_2 corresponds to the grain boundary resistance. The bulk resistance from the z-fit is $5.4 \times 10^5 \Omega$, which gives an ionic conductivity of $1.2 \times 10^{-7} \text{ S/cm}$.

R_1 (Ω) (bulk)	R_2 (Ω) (gb)	Q_1 (F)	Q_2 (F)	Q_3 (F)	χ^2
5.4×10^5	8.8×10^5	1.2×10^{-10}	2.3×10^{-9}	1.9×10^{-7}	9.0×10^{-2}

Table 5: Fitting parameters of the equivalent circuit.

3.4.3.3 SEM/EDX characterization

The sample was also analyzed by SEM and EDX. **Figure 38** below shows an SEM image of the material. Small polygons were observed, but they seemed covered in an amorphous material, and the degree of crystallinity did not seem very high. However, as the sample reacts with air, and given that the process of introducing the sample into the SEM chamber takes a couple of minutes, it had time to degrade partially, as shown in the EDX results. As sulfides react with H_2O to form H_2S we

have a deficit of sulfur and additional oxygen atoms in the structure. The Na/P atom ratio is approximately one, as expected. The experiment needs to be redone with an SEM equipped with an air-lock.

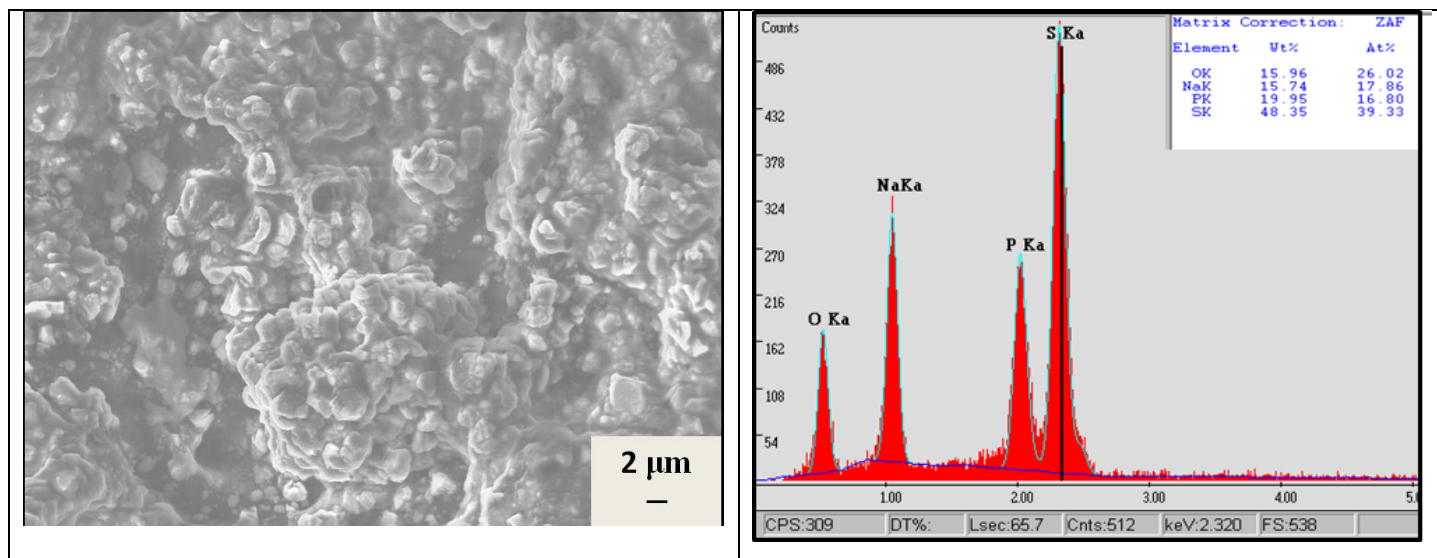


Figure 38: SEM image and EDX analysis of Li_2NaPS_4 .

3.4.3.4 Raman analysis

Finally, the material was analyzed by Raman spectroscopy to check if the tetrahedra present in the structure are detectable by Raman. **Figure 39** shows the Raman spectrum of Li_2NaPS_4 . A main band was observed at 420 cm^{-1} , corresponding to PS_4^{3-} ions. The spectrum exhibits two other weak peaks at 250 and 280 cm^{-1} respectively. Investigation into characteristic NaS_4 and LiS_4 tetrahedral vibrational frequencies in other known compounds did not give rise to any possible match to these two peaks.

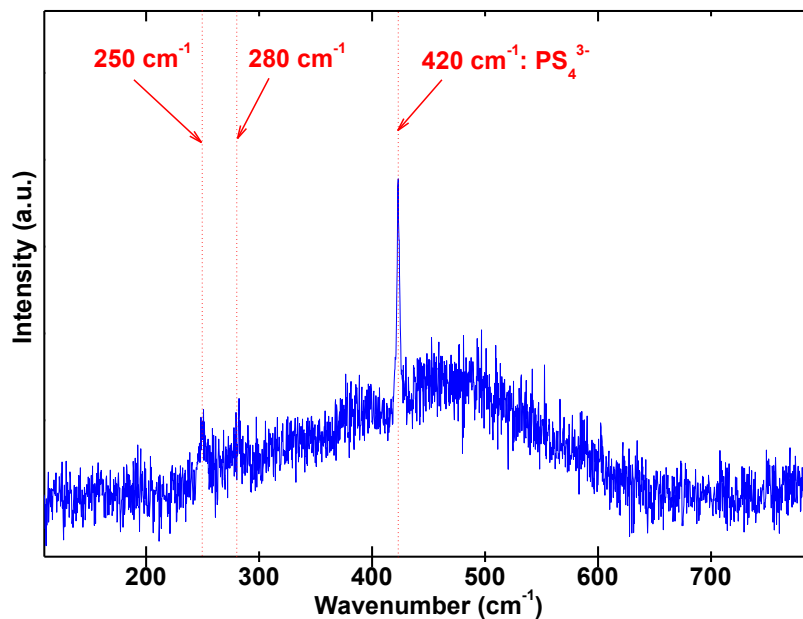


Figure 39: Raman spectrum of Li_2NaPS_4 .

3.4.4 Conclusion and future work

A new phase, Li_2NaPS_4 , was discovered. It was analyzed by XRD, SEM, EDX, Raman and impedance spectroscopy. Although this material seemed at first promising, its poor ionic conductivity of 10^{-7} S/cm compromises its application to all-solid-state batteries. More studies should be done to investigate the reasons of such poor conductivity, the nature of the actual charge carriers (Li^+ or Na^+ ions), and possible element and vacancy substitutions to improve its conductivity and reactivity.

3.5 Conclusions and perspectives

In this chapter, we have first done a summary of $\text{Li}_7\text{P}_3\text{S}_{11}$ way of synthesis by describing the influence of the different parameters. From experimental observations, it seems difficult to upscale the synthesis of this superionic conductor, however its study has enabled us to improve its crystallinity and ionic conductivity and to fabricate all-solid-state batteries.

In the second section, pursuit of the theoretical $\text{Na}_7\text{P}_3\text{S}_{11}$ phase led to the discovery of two unknown structures, which, after further analysis, seemed to be polymorphs of the $\text{Na}_4\text{P}_2\text{S}_7$ phase.

Finally, a new sulfide-based material, Li_2NaPS_4 , was discovered and characterized. However, it exhibited a low ionic conductivity of about 4×10^{-8} S/cm, perhaps due to the mixture of charge carriers in its structure (Na^+ and Li^+ cations). Although it is not promising for applications to all-solid-state batteries, more analyses and attempts to improve its conductivity (by substitution or insertion of other elements) can be done.

Chapter 4:

Applications to Lithium-Sulfur All-Solid-State Batteries

4.1 Introduction

In this section, charge-discharge performance of different batteries is investigated at room temperature. First, the influence of two different solid electrolytes - $\text{Li}_7\text{P}_3\text{S}_{11}$ and $\text{Li}_{10}\text{GeP}_2\text{S}_{12}$ - on specific capacity, capacity retention and rate capability is examined. The all-solid-state cells achieved a high specific capacity but showed poor capacity retention and rate capability. In particular, the $\text{Li}_{10}\text{GeP}_2\text{S}_{12}$ -based cell had an initial higher-than-theoretical capacity, likely due to irreversible decomposition reactions of $\text{Li}_{10}\text{GeP}_2\text{S}_{12}$ (LGPS).

Second, different compositions of the composite cathode are studied to enhance the overall performance of the batteries. Two different electronic conductors -Ketjenblack (KB) and Activated Carbon (AC)- as well as two ionic conductors -LGPS and $\text{Li}_{1.5}\text{PS}_{3.25}$ - are compared.

All the cathodes had a sulfur loading of 51 weight % and the capacities were normalized by the weight of sulfur in the cathodes. The charge-discharge curves are presented versus Li-In potential (left-hand vertical axis in figures) and versus Li^+/Li (right-hand vertical axis), which is calculated based on the potential difference between Li and Li-In electrodes (0.6 V for Li-In alloys with a Li/In molar ratio < 1) ⁶⁴. The cells show typically an average operating voltage of 2.1 V vs Li^+/Li (1.5 V vs Li-In), which corresponds to traditional potential in liquid electrolyte batteries. This result suggests that the same electrochemical reaction occurs in all-solid-state batteries: $\text{S} + 2\text{Li}^+ + 2\text{e}^- = \text{Li}_2\text{S}$. Thus, just as for the liquid cells, one of the main issues encountered in all-solid-state cells will be related to the volumetric expansion in the transformation of sulfur into lithium sulfide. This should further

increase the risk of poor solid-solid contact at the interfaces, which is already inherent to all-solid-state cells.

4.2 Experimental

4.2.1 Solid electrolytes

Three sulfide solid ionic conductors, $\text{Li}_7\text{P}_3\text{S}_{11}$, $\text{Li}_{10}\text{GeP}_2\text{S}_{12}$, and $\text{Li}_{1.5}\text{PS}_{3.25}$, were synthesized in order to compare their performance in all-solid-state cells. Both solid electrolytes $\text{Li}_7\text{P}_3\text{S}_{11}$ and $\text{Li}_{10}\text{GeP}_2\text{S}_{12}$ were prepared by using a high energy ball milling method followed by a heat-treatment. For $\text{Li}_7\text{P}_3\text{S}_{11}$ (see section 3.1), Li_2S and P_2S_5 in a 70:30 molar ratio were weighed, placed into a zirconia jar with 300 balls under argon atmosphere, and then ball milled at 900 rpm for 2 h. Partially crystalline $\text{Li}_7\text{P}_3\text{S}_{11}$ was obtained, and after heat-treatment at 300°C for 1 h, the sample was highly crystalline. For $\text{Li}_{10}\text{GeP}_2\text{S}_{12}$, Li_2S , GeS_2 and P_2S_5 were weighed in a 5:1:1 molar ratio, milled at 300 rpm for 12 h, and then heat-treated in a quartz tube sealed under vacuum at 550°C for 8 h³¹. $\text{Li}_{1.5}\text{PS}_{3.25}$, used as an ionic conductor in the cathode, was prepared by ball milling Li_2S and P_2S_5 in a 60:40 molar ratio at 200 rpm for 14 h until it became amorphous³¹. The structure and the ionic conductivity of the solid electrolytes were analyzed by XRD and EIS respectively.

4.2.2 Positive composite electrodes

Three different composite cathodes were prepared. Sulfur was used as the active material, KetjenBlack (KB) or Activated Carbon (AC MAXSORB ®), as the electronic conductor, and $\text{Li}_{1.5}\text{PS}_{3.25}$ or LGPS, as the ionic conductor. The three cathodes were **KB/S/Li_{1.5}PS_{3.25}**, **AC/S/Li_{1.5}PS_{3.25}** and **AC/S/LGPS** with a Carbon-Sulfur-Solid Electrolyte weight ratio of 9-51-40 %. The carbon-sulfur mixtures were weighed in a 10-90 wt%, and then wet milled in acetone in a stainless steel jar at 370 rpm for 10 hours. After drying, the materials were annealed at 160°C overnight. Subsequently, the C-S composites were mixed with the solid electrolyte ($\text{Li}_{1.5}\text{PS}_{3.25}$ or LGPS) in a 60:40 weight ratio, and dry milled at 370 rpm for 15 hrs. XRD, TGA, DTA and BET analyses were performed on the materials at each step of the synthesis to evaluate the impact of each treatment on the morphology of the three electrodes.

4.2.3 Negative electrode

Li-In was used as the counter-electrode in all of the batteries. An indium foil disk was applied on top of a lithium foil disk (with a Li/In molar ratio of 0.79). The resulting alloy disk was attached on a stainless steel current collector, and applied against the bi-layered pellet contained in the cell cylinder (see section 2.5.1). In all-solid-state batteries, the irregular lithium deposition and lithium dissolution processes cause the formation of lithium dendrites at the anode over cycling, similar to liquid batteries. The propagation of the dendrites is directly correlated with the density of the solid electrolyte layer of the cell. In the case of soft sulfide-based solid electrolytes, cold pressing can easily achieve densities of 90%, and hot pressing at low temperatures (in the range of 60°C to 100°C) is an efficient method to obtain densities of over 99%. However, even when the solid electrolyte pellet has a very high density (> 95 %), the lithium dendrites are still able to grow through the micro-cracks generated after several cycles, and as a result, the cells show short cycle life. A single defect in the electrolyte pellet will be an opened path to dendrite growth. One way to limit the dendrite growth is to apply an indium protective layer on top of the lithium. Additionally, as the electrode potential of the Li-In alloy is constant and equal to 0.6 V vs Li⁺/Li (for Li/In molar ratios below 1) ⁶⁴, the potentials, and thus the reactions occurring at these potentials can easily be compared with reactions taking place in traditional liquid Li-S systems.

4.3 Results and discussion

4.3.1 Comparison of solid electrolytes

4.3.1.1 Galvanostatic cycling

In this section, performance of Li₇P₃S₁₁ and LGPS as solid electrolytes are compared. **Table 6** below summarizes the ionic conductivities of both materials.

Material	Ionic conductivity (reported in literature)	Ionic conductivity of the materials used in the batteries
Li ₇ P ₃ S ₁₁	5.0 x 10 ⁻³ S/cm	1.2 x 10 ⁻³ S/cm
Li ₁₀ GeP ₂ S ₁₂	1.1 x 10 ⁻² S/cm	7.0 x 10 ⁻³ S/cm

Table 6: Ionic conductivities at room temperature of $\text{Li}_7\text{P}_3\text{S}_{11}$ and LGPS, in literature and as-used in all-solid-state cells.

Galvanostatic measurements were performed on two all-solid-state cells using respectively $\text{Li}_7\text{P}_3\text{S}_{11}$ (**Figure 40.a**) and LGPS (**Figure 40.b**), as the solid electrolyte. The composite cathode was **KB-S- $\text{Li}_{1.5}\text{PS}_{3.25}$** in both cells and the assembly process was identical (described in section 2.5.1). The two batteries were run at a C/50 charge rate at 25°C, and the first cycles are presented in **Figure 40**. The cut-off voltages are -0.5 V in discharge and 3.4 V in charge for the $\text{Li}_7\text{P}_3\text{S}_{11}$ -based battery, and 0 V in discharge and 3 V in charge for the LGPS-based battery (vs Li-In). The all-solid-state cell using $\text{Li}_7\text{P}_3\text{S}_{11}$ exhibits an initial discharge capacity of 800 mA.h/g. After the first discharge, the charge and discharge capacities drop to 600 mA.h/g (so 200 mA.h/g below the initial capacity), but remain relatively stable from there up to the 20th cycle (not shown here). The cell using LGPS shows overall higher capacity, which can be reasonably interpreted as a benefit from the superior ionic conductivity of the electrolyte (see **Table 7**). However, the first discharge capacity of the LGPS cell is of 1850 mA.h/g, which is above the maximum theoretical capacity of the Li/S couple (1672 mA.h/g). Investigation needs to be done to determine the side reaction generating this added capacity. As this phenomenon is not observed for the $\text{Li}_7\text{P}_3\text{S}_{11}$ -based cell, this is most likely due to some decomposition reaction of LGPS. After the 2nd cycle, the charge and discharge capacities stabilize around 1200 mA.h/g, more than 600 mA.h/g below the first discharge, which attests of irreversible reactions. In addition, contrary to the $\text{Li}_7\text{P}_3\text{S}_{11}$ all-solid-state cell, the discharge curve of the LGPS-based battery exhibits a change of slope, which is the sign of a second reaction (possibly LGPS decomposition) occurring after/during the transformation of sulfur in Li_2S upon discharge. Lastly, we can observe that the charge-discharge curves of the LGPS cell are not symmetrical: the side reaction seems to only occur during the discharge of the battery.

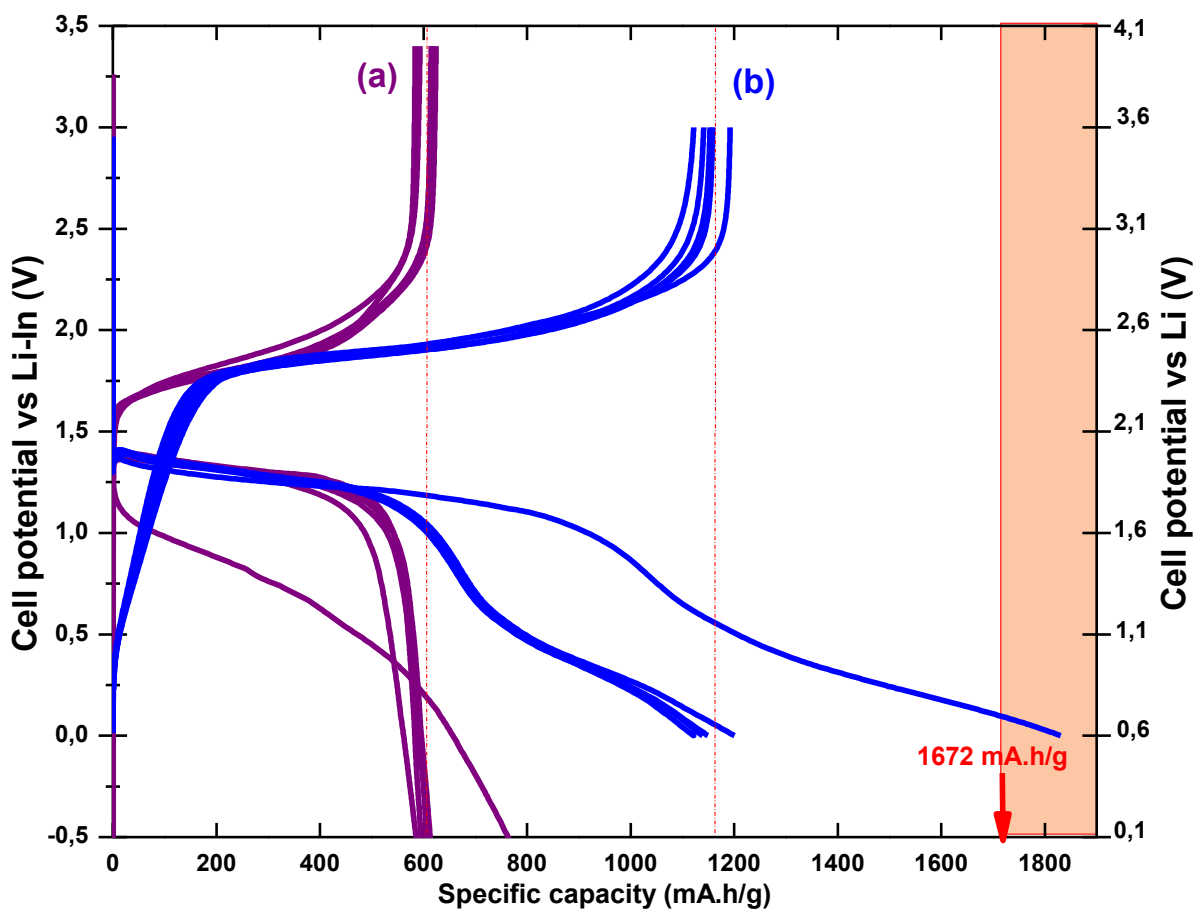


Figure 40: Charge-discharge curves of (a) $\text{Li}_7\text{P}_3\text{S}_{11}$ -based and (b) LGPS-based all-solid-state cells.

In conclusion, $\text{Li}_7\text{P}_3\text{S}_{11}$ shows relatively better stability upon cycling than LGPS, but poorer capacity values. Yet the LGPS cell seems to undergo an additional reaction while discharging, which results in an inflection in the curve and an irreversible extra-capacity. Finally, in all cells there is a huge drop in capacity (never recovered) after the first discharge, which appears to be inherent to the all-solid-state cells and could be solely due to the volumetric expansion upon formation of Li_2S within the cathode.

4.3.1.2 Investigation in extra-capacity

Cyclic Voltammetry was performed on LGPS and $\text{Li}_7\text{P}_3\text{S}_{11}$ versus Li-In. For both cells, a stainless steel rod and a lithium-indium foil as counter and reference electrodes were attached on each face of the pelletized electrolytes. The potential sweep was carried out between 0 V and 3 V for

LGPS, and between 0 V and 3.5 V for $\text{Li}_7\text{P}_3\text{S}_{11}$ (potentials are vs Li-In), with a voltage scan rate of 15 mV/s. The results are presented in **Figure 41**. The potential windows are actually 0.6-3.6 V vs Li, and 0.6-4.1 V vs Li, respectively. Overall, both electrolytes show reactivity, as the voltammograms are not completely flat. The $\text{Li}_7\text{P}_3\text{S}_{11}$ voltammogram exhibits a cathodic peak around 1.02 V vs Li^+/Li (0.62 V vs Li-In) with an intensity of about 0.075 mA, and an anodic peak around 1.93 V vs Li^+/Li (1.33 V vs Li-In) with an intensity of 0.025 mA. The CV of LGPS shows a significantly more intense peak (above 0.3 mA) at 1.14 V vs Li^+/Li (0.54 V vs Li-In), attesting of a redox reaction, and an overall higher reactivity (given by the intensity of the background profile) although no peak is clearly identifiable, which could be due to the presence of amorphous phase in the sample. These results show that LGPS is considerably more reactive than $\text{Li}_7\text{P}_3\text{S}_{11}$, and undergoes redox reactions against Li-In in the cycling voltage window. This corroborates with the electrochemistry data shown in the previous section.

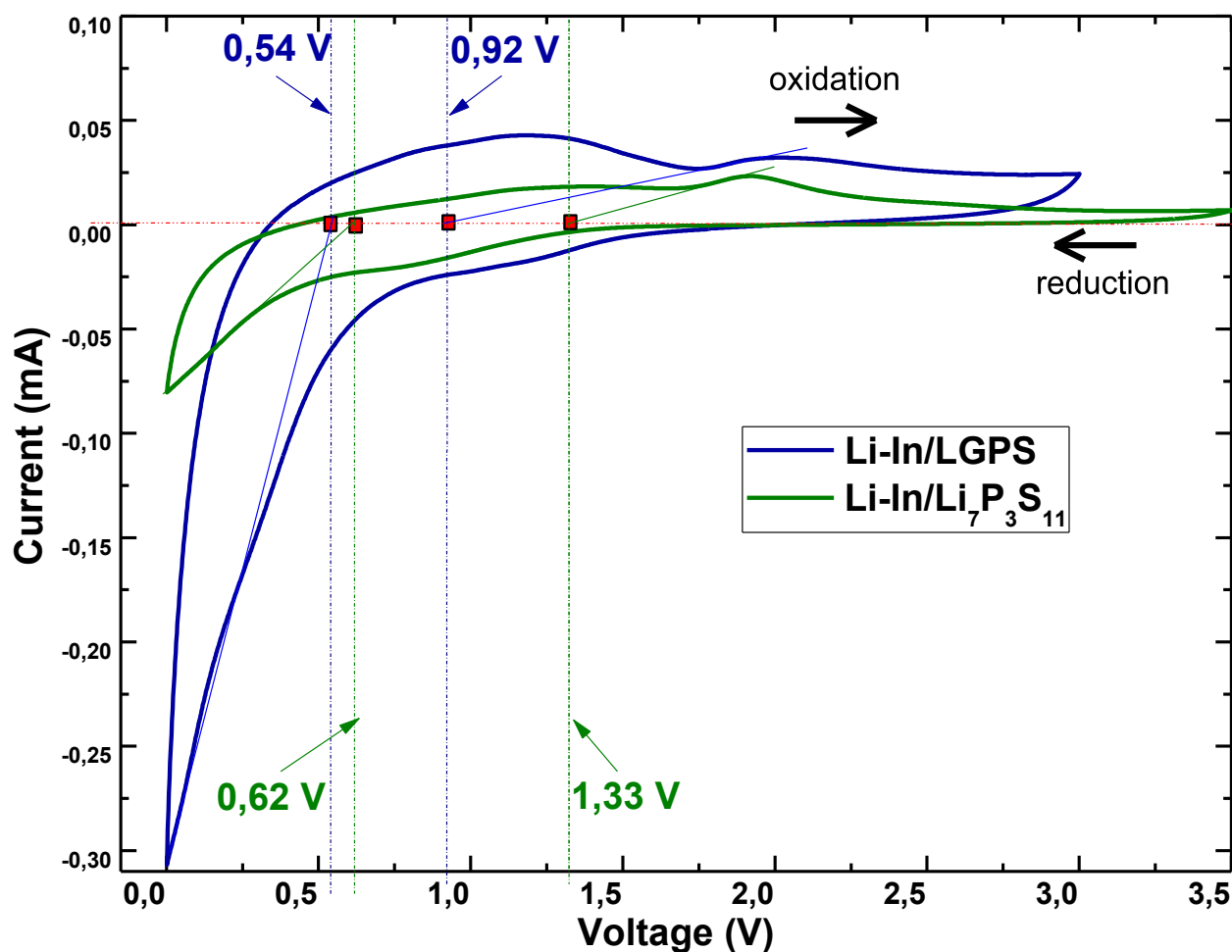


Figure 41: Cyclic voltammogram of (a) LGPS and (b) $\text{Li}_7\text{P}_3\text{S}_{11}$ against Li-In at the first cycle.

The new study aims at determining if the ionic conductor ($\text{Li}_{1.5}\text{PS}_{3.25}$) from the cathode, which is sulfide-based, does not behave as an active material (upon cycling or upon contact with LGPS). For this purpose, a cell without sulfur (regular active material) was assembled and cycled at the same rate and with the same cut-off voltages as the LGPS-based cell presented previously. **Figure 42** shows the charge-discharge curves of a (**SuperP-Li_{1.5}PS_{3.25}**)/(**Li₁₀GeP₂S₁₂**)/(**Li-In**) battery. The mass of $\text{Li}_{1.5}\text{PS}_{3.25}$ solid electrolyte was the same as in the LGPS-based battery so that the specific capacity was directly comparable to the cell with active material (sulfur). SuperP (SP) was chosen to be the electronically conductive host as it has poor surface area and is unable to retain Li ions in its matrix. The galvanostatic measurements show an initial discharge capacity of about 50 mA.h/g, which deteriorates very quickly: after 5 cycles, the discharge capacity is cut in half to only 25 mA.h/g. The charge capacities are lower than the discharge capacities (below 20 mA.h/g), which suggests that the charge and discharge redox reactions are not reversible. Overall, these results demonstrate that the capacity generated from the cell without active material is negligible and fades very quickly, so it can be disregarded in the analysis of battery performance. Thus, we can safely say that the added capacity in the LGPS cell is solely due to electrochemical decomposition reactions of LGPS.

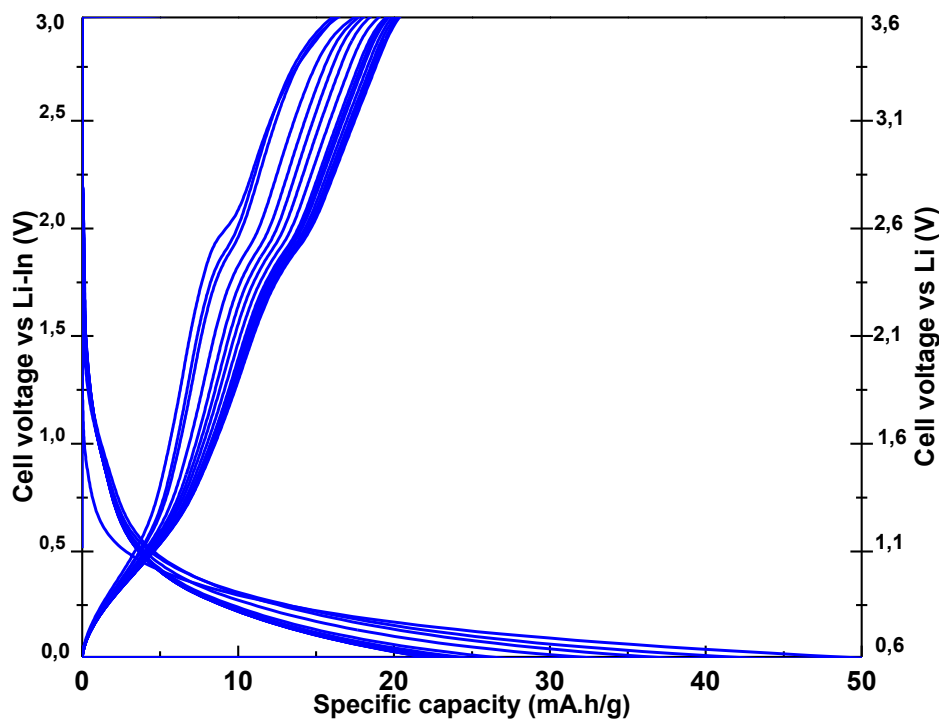


Figure 42: Charge-discharge curves of a (**SP-Li_{1.5}PS_{3.25}**)/(**Li₁₀GeP₂S₁₂**)/(**Li-In**) cell.

4.3.1.3 Conclusion

In conclusion, although we have used the two most promising solid electrolytes up-to-date, $\text{Li}_7\text{P}_3\text{S}_{11}$ and $\text{Li}_{10}\text{GeP}_2\text{S}_{12}$, the batteries showed quick fading of capacity. In particular, LGPS seems to undergo side reactions that give added capacity in the initial cycles, but as they are irreversible, fast decay of capacity is observed. $\text{Li}_7\text{P}_3\text{S}_{11}$ is more stable but has a significantly lower capacity.

Following these results, the search for chemically and electrochemically stable solid electrolytes needs to be pursued. The literature is mitigated about LGPS stability against Li and Li-In. Some papers have reported stable LGPS material, in others it is not.

In our case, the fast degradation of the cells might come from air contamination as well. Our batteries are sealed in glass jars and as a battery takes weeks to run a couple of cycles, there is a reasonable chance that the materials degrade with time. Channels are in the process of being set up in an inert dry atmosphere in a glovebox. Still, the need for more chemically and electrochemically stable solid electrolytes is more and more important. Cycling at higher temperatures ($\sim 100^\circ\text{C}$) is another approach to reduce cycling time and thus time of the exposure and degradation due to contamination. However, the design of the cells has to be adapted to higher working temperatures, and currently no design has given entire satisfaction.

In the next section, different cathode compositions are studied and characterized electrochemically.

4.3.2 Study of the cathode composition

An intimate contact between all solid components in the composite cathode is crucial for good performance and rate capability. A combination of thermomechanical milling and thermal treatments has shown to be one of the easiest ways to achieve good solid-solid contact within the cathode³¹. Other methods such as Pulsed Laser Deposition (PLD) have proven to be even more efficient³¹ but are consequently more expensive and time-consuming and we don't dispose of the appropriate air-free instrumentation in our lab. One of the goals for our batteries was to use cells with a minimum sulfur loading of 50 wt %, as we want to achieve sufficient energy density for practical applications.

Two different carbons with high surface area (KB and AC) were used, as surface area is a very important factor to enable intimate contact of the electronically conductive host with the other materials³¹. In the first section, we compare the performance of two Li-S, one having a KB-based cathode and the other an AC-based cathode.

As far as the ionic conductor is concerned, many studies have been carried out to determine the key requirements to achieve the highest performance. Chikusa and Nagata claimed that the use of the amorphous $\text{Li}_{1.5}\text{PS}_{3.25}$ enables a better activation of sulfur within a solid-state electrode, due to its ductility and amorphous structure (and despite its poor conductivity)⁶⁵. Thus, in the second section, we compare the charge-discharge curves of two cells, one prepared using $\text{Li}_{1.5}\text{PS}_{3.25}$ (amorphous and poorly conductive) and the other one using LGPS (crystalline and highly conductive) in the composite cathode.

4.3.2.1 Comparison of two electronic conductors: AC and KB

Figure 43 below shows the XRD patterns of **Ketjenblack-sulfur** and **Activated Carbon-sulfur** composites after mechanical milling at room temperature. **Figure 44** displays the XRD patterns of the milled samples after subsequent annealing at 160°C. Both milled composites exhibit peaks attributable to α -sulfur, which is slightly more crystalline in the **KB-S** mixture (the peaks are sharper). The presence of sulfur at this stage is not surprising as we have a very high proportion of sulfur (90 wt %). The use of very high surface area carbons should allow the embedding of the sulfur in the carbon matrix upon further treatment, as demonstrated by the results in **Figure 44**, in comparison with **Figure 43**. Both figures are at the same scale and the XRD measurements were performed in the same conditions. Upon annealing, the peaks of α -sulfur in the **KB-S** mixture have significantly decreased by more than half, and in particular the milled-annealed **AC-S** composite exhibits an almost amorphous pattern, with a higher halo background and a few small peaks of α -sulfur. These results suggest that part of the crystalline sulfur changed into amorphous sulfur, and that the amorphization is favored in the AC carbon compared to KB.

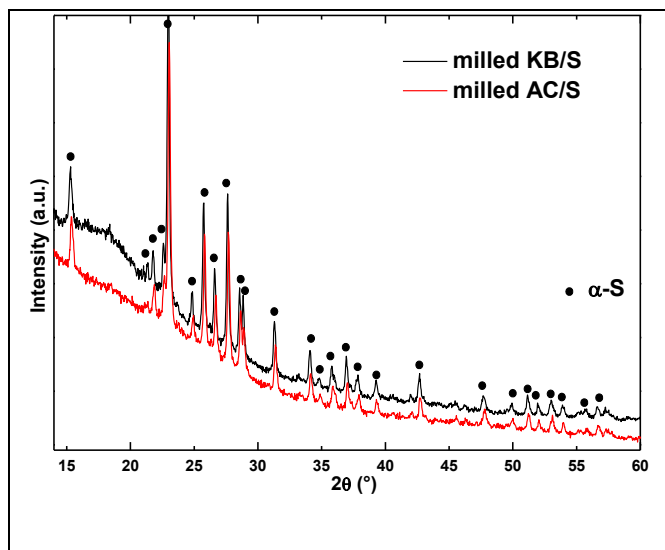


Figure 43: XRD patterns of mechanically milled Ketjenblack-sulfur (**KB-S**) and Activated Carbon-sulfur (**AC-S**) composites

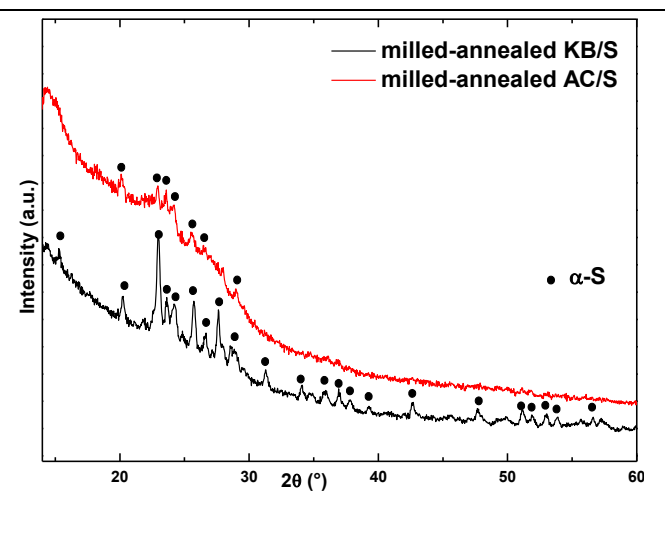


Figure 44: XRD patterns of milled and annealed Ketjenblack-sulfur (**KB-S**) and Activated Carbon-sulfur (**AC-S**) composites

The milled-annealed samples were then milled with $\text{Li}_{1.5}\text{PS}_{3.25}$ in a 60:40 weight ratio. **Figure 45** shows the XRD patterns of the milled composites **KB/S/Li_{1.5}PS_{3.25}** and **AC/S/Li_{1.5}PS_{3.25}**. Both are halo patterns and have no peaks of α -sulfur. Most likely, the amorphous solid electrolyte coats the carbon-sulfur composites and covers all the crystalline sulfur.

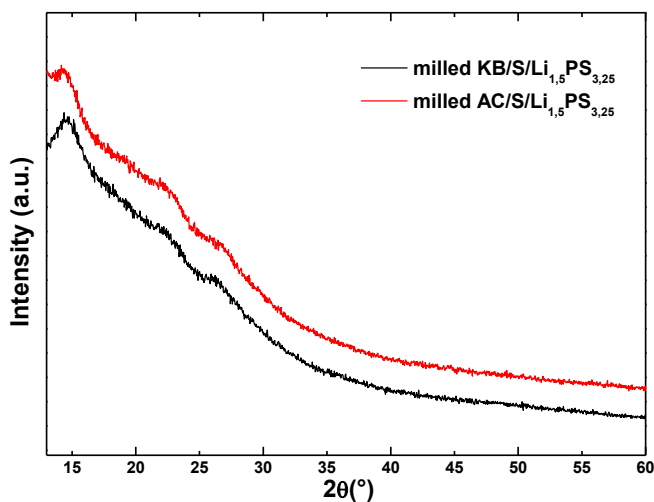


Figure 45: XRD patterns of mechanically milled **KB/S/Li_{1.5}PS_{3.25}** and **AC/S/Li_{1.5}PS_{3.25}** composites.

Figure 46 below shows the TGA curves of the (a) **KB-S** and (b) **AC-S** composites, after milling and after annealing. For the **KB-S** mixture (10:90 wt %), the weight decreases drastically (by 84.4 %) in the range of 200-350°C, which is characteristic of evaporation of sulfur in annealed cathode materials. After annealing at 160°C, the **KB-S** composite exhibits a shift in the temperature at which mass loss occurs (compared to the sample that has been milled only). Additionally, the total weight loss is of only 83.2% against 84.4% after milling. Similarly, upon annealing, the **AC-S** composites show an increase in the temperature characteristic of weight change, and a reduced percentage of weight loss from the milled to the milled-annealed sample. Furthermore, a change in the slope of the curve is observed around 250°C, which is characteristic of a two-step reaction. Upon annealing, the weight loss changes from 85.6% to 78.5%, so some sulfur might be too embedded in the pores of the carbon to evaporate. Overall, the change in ranges of temperature of mass loss is due to the different morphologies of sulfur and carbon, and to the contact area and adhesion between them. Thus, an increase in temperature of mass change indicates stronger bonding and better coating of the sulfur on the carbon. Each part of the curves corresponds to a different type of sulfur morphology, as supported by the XRD results.

Upon mixing with the binding solid electrolyte $\text{Li}_{1.5}\text{PS}_{3.25}$ (**Figure 47**), the **KB/S/Li_{1.5}PS_{3.2}** composite curve takes a two-steps shape, and exhibits a total weight loss of 61.1%. The **AC/S/Li_{1.5}PS_{3.25}** cathode shows evaporation of 51.4% of its weight and a several-step reaction curve. As sulfur consists of only 51 % of the total weight of each composite, it seems that some of the solid electrolyte evaporates as well, or that some reaction occurs. In any case, this data shows a change in morphology upon subsequent treatments and an increase in adhesion between the composites.

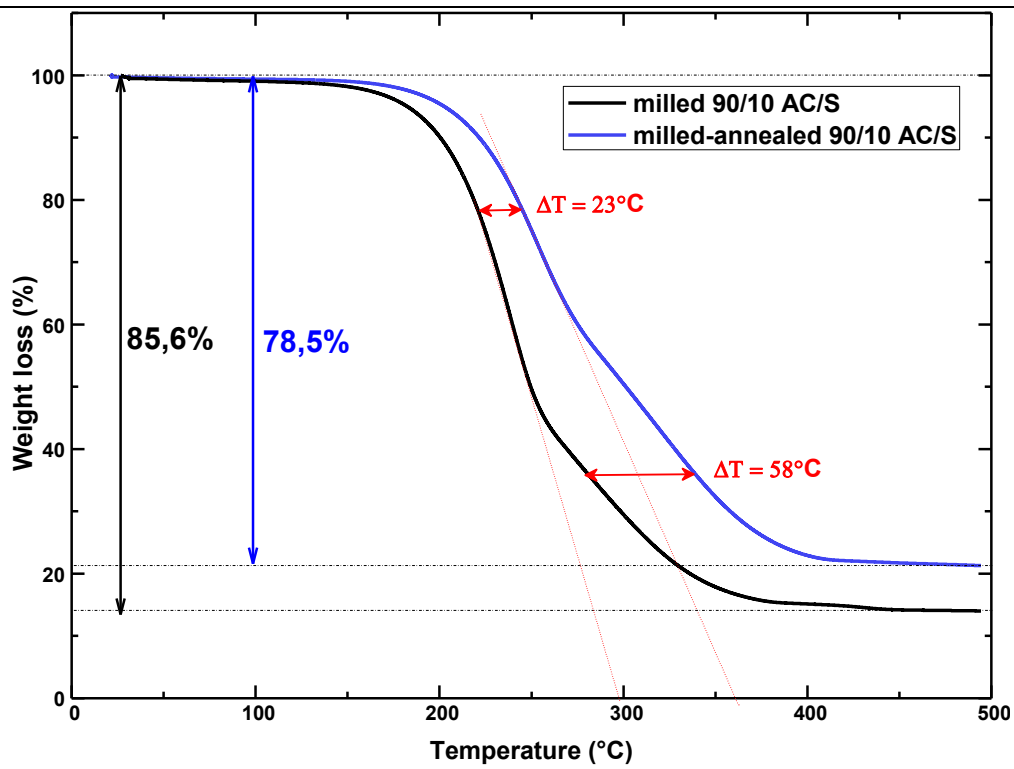
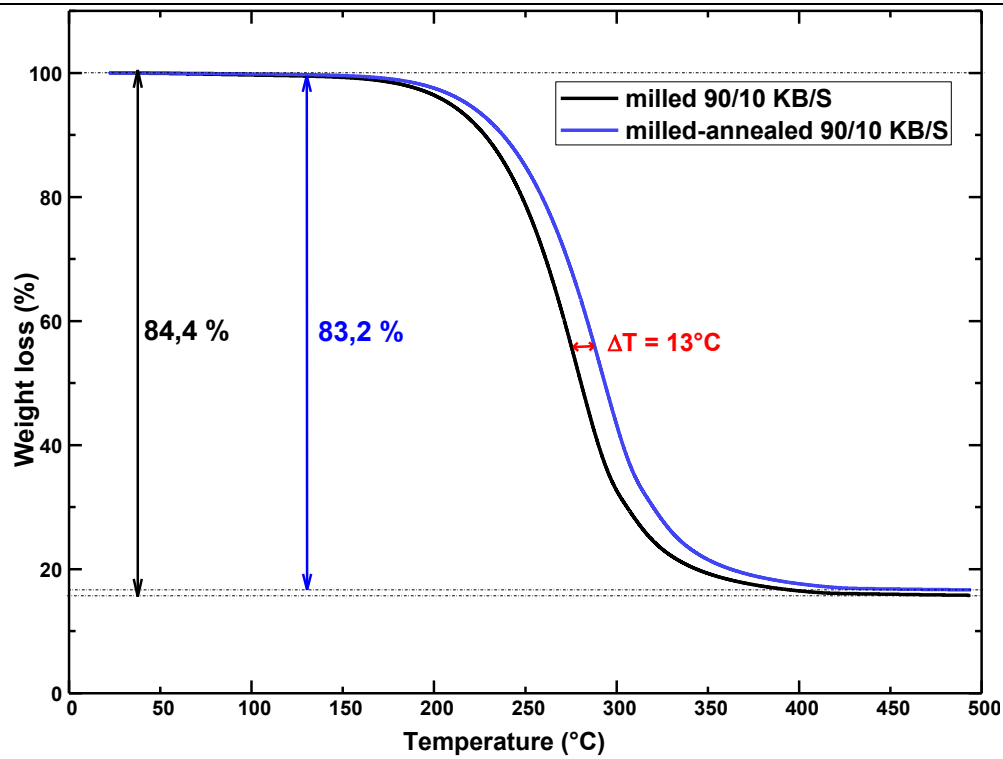


Figure 46: TG curves of (a) KB-S composites and (b) AC-S composites, prepared by mechanical milling, and milling-annealing respectively.

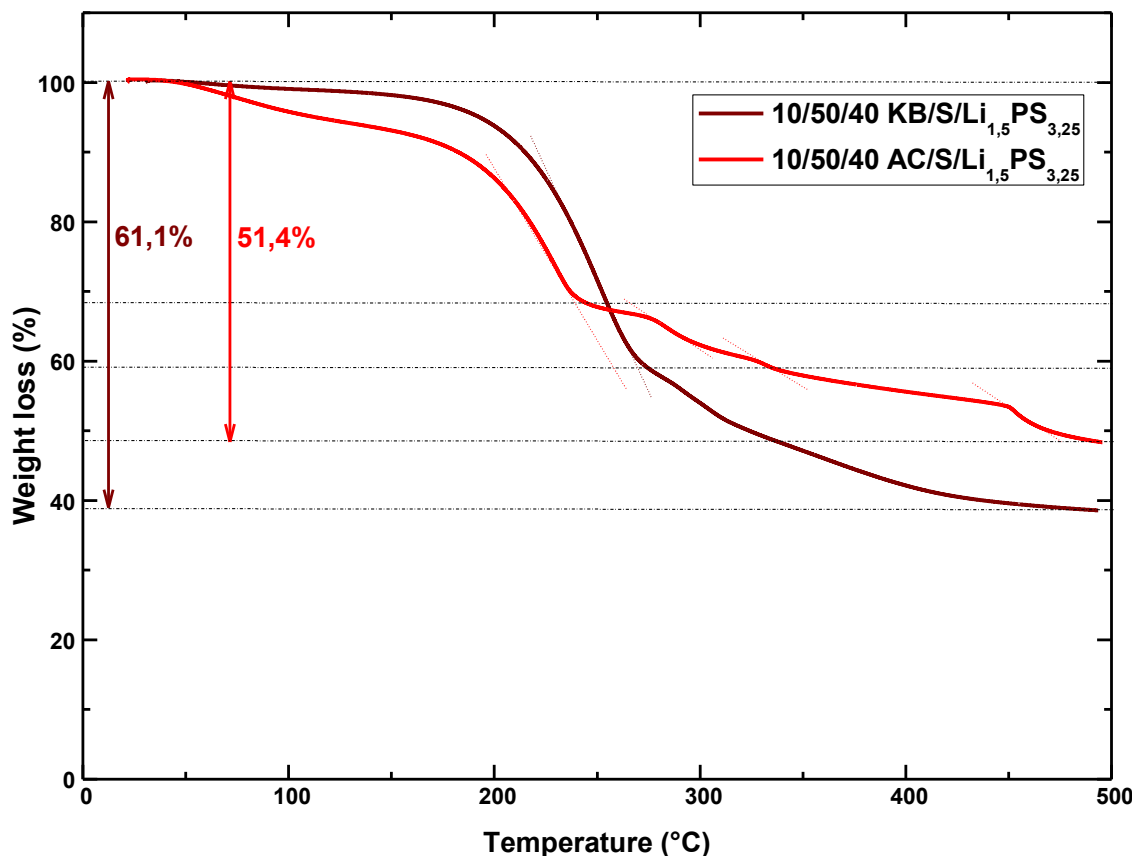


Figure 47: TG curves of **KB/S/Li_{1.5}PS_{3.25}** and **AC/S/Li_{1.5}PS_{3.25}** composite cathodes.

Differential Thermal Analysis (DTA) curves are shown in **Figure 48** for each prepared composite. The curves **(a)** (milled KB-S), **(b)** (milled-annealed KB-S), **(c)** (milled AC-S), and **(d)** (milled-annealed AC-S) exhibit endothermic features in the range of 100-125°C. The peaks are significantly smaller for the AC-based composites compared to the KB-composites, which indicates a smaller amount of material undergoes the transformation in the AC-based compounds. These peaks match the characteristic temperature of transformation of elemental sulfur (which melts at 115°C). Thus, as shown by XRD and TGA results, this DTA analysis demonstrates that upon treatments, the sulfur morphology changes and S₈ barely remains in the composites. Instead, another type of sulfur, which is amorphous and more strongly bound to the carbon host, is formed. Lastly, AC is more effective than KB, as it has a superior surface area. In the case of the **KB/S/Li_{1.5}PS_{3.25}** **(e)** and **AC/S/Li_{1.5}PS_{3.25}** **(f)** composite cathodes, no exo- or endo- thermic changes are observed in this range

of temperature, confirming the previous results. DTA of the solid electrolyte is shown for comparison to ensure that they do not undergo any thermal change.

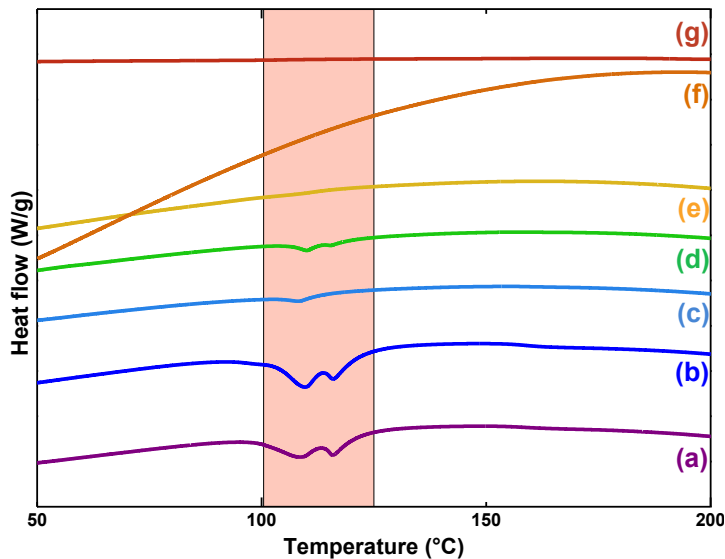


Figure 48: DTA curves of (a) milled KB-S, (b) milled-annealed KB-S, (c) milled AC-S, (d) milled-annealed AC-S, (e) KB/S/Li_{1.5}PS_{3.25}, (f) AC/S/Li_{1.5}PS_{3.25} composites, and (g) Li_{1.5}PS_{3.25}.

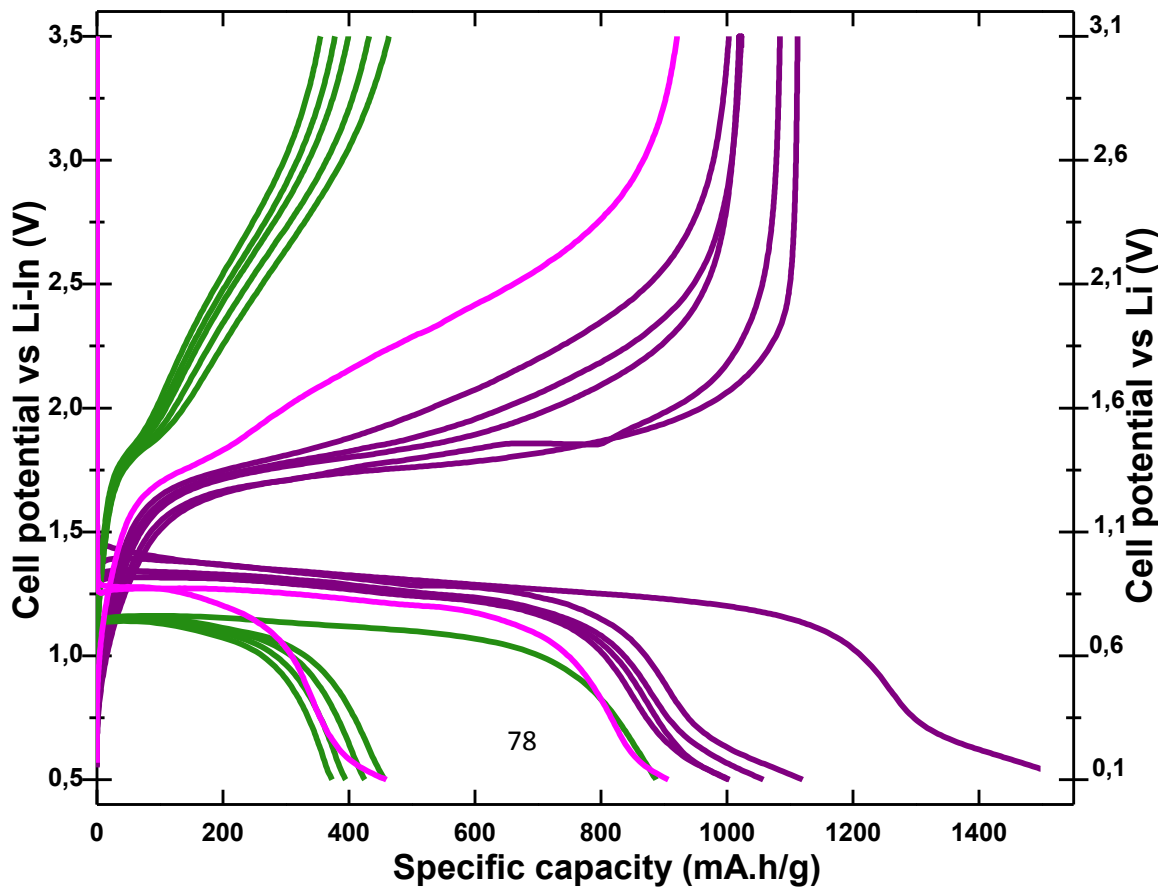
BET analysis was performed on the samples at every step, and the results are presented in **Table 8** below. The data, obtained by a multi-point analysis, is consistent with the XRD patterns presented in **Figure 44** and **Figure 45**. Mechanical milling results in smaller particle size of the materials, and the S₈ is uniformly scattered within the host's pores and surface. Upon annealing at 160 °C (minimum of viscosity of sulfur), elemental sulfur melts and diffuses more into the pores, which gives a significant decrease in total pore volume. Finally, when the solid electrolyte is added and milled with the carbon-sulfur composites, the pore volume is further reduced.

Material	Total surface area (m ² /g)	Total Pore volume (cm ³ /g)	Average pore diameter (Å)
KetjenBlack	1400	0.46 (for pores < 15.7 Å)	13.13
Activated Carbon (@MAXSORB)	4816	1.42 (for pores < 13.1 Å)	11.8
Milled-Annealed KB/S	0	4.95	
Milled-Annealed AC/S	6.6	1.81 x 10 ⁻³ (for pores < 13)	10.98

		Å)	
Milled KB/S/Li _{1,5} PS _{3,25}	1.3	5.53 (for pores < 13 Å)	
Milled AC/S/Li _{1,5} PS _{3,25}	0	1.7 x 10 ⁻⁶	

Table 8: BET analysis of the different carbon composites.

An all-solid-state cell was assembled using LGPS as the solid electrolyte, Li-In as the counter electrode, and an AC-based cathode. The charge-discharge voltage profile of the [AC/S/Li_{1,5}PS_{3,25}]/LGPS/Li-In cell is shown in **Figure 49**. The voltage window was set up from 0.5 V to 3.5 V vs Li-In, as LGPS decomposes below 0.5 V (see section 4.3.1). The cell was first run at C/50, then C/20 and then at C/50 again. After an initial specific discharge capacity of 1500 mA.h/g, the capacity drops and stabilizes around 1100 mA.h/g (73% of initial capacity). When cycled at C/20, the specific capacity drops to 400 mA.h/g (27% of initial capacity), after a cycle of adaptation. When the cell is cycled again at C/50, the capacity increases to 910 mA.h/g (which represents 61% of initial discharge capacity). We can first note that we do not have higher-than-theoretical capacity, so the reduction of the voltage window seems to be efficient to prevent LGPS decomposition. However, the cell exhibits a capacity loss of 400 mA.h/g (27%) between the first discharge and the first charge. This seems to be inherent to all solid cells and might come from physical degradation in the cathode and electrolyte after activation. Overall, the AC-based battery shows poor adaptability to rate change, and poor capacity at higher rate. This may come from the relatively low electronic conductivity of



AC.

Figure 49: Charge-discharge voltage profile of an all-solid-state cell with an **AC/S/Li_{1.5}PS_{3.25}** cathode.

We can compare the performance of the AC-based cell with the battery presented in the first section: **[KB/S/Li_{1.5}PS_{3.25}]/LGPS/Li-In**, although the voltage window is different (from 0 V to 3 V) and results in added capacity from LGPS reactivity. **Figure 50** compares at different rates the specific discharge capacity as a function of the number of cycles of the KB-based cell with the AC-based cell. The all-solid-state battery using KB has a larger irreversible drop of capacity after the 1st discharge (about 33% of the initial capacity against 27% for the AC-based cell). At C/20, the KB cell capacity decreases from 1100 to 700 mA.h/g (a 33% drop from 1100 mA.h/g) while the AC cell capacity deteriorates from 1000 to 400 mA.h/g (a 60% drop from 1000 mA.h/g). At C/20, the decay in capacity is comparable for both batteries. These results can be explained by the difference in electronic conductivity, which matters more at higher current densities (the charges need to be carried and transferred faster at the materials interfaces). When cycling at the lower rate of C/50, the KB cell recovers about 90% of the reversible capacity achieved at C/50 for its first cycles. The AC-based all-solid-state cell also recovers 90% although its capacity loss at C/20 was significantly larger. This shows that there was no or limited irreversible degradation of the cathode and of the solid-solid contacts after the 1st cycle.

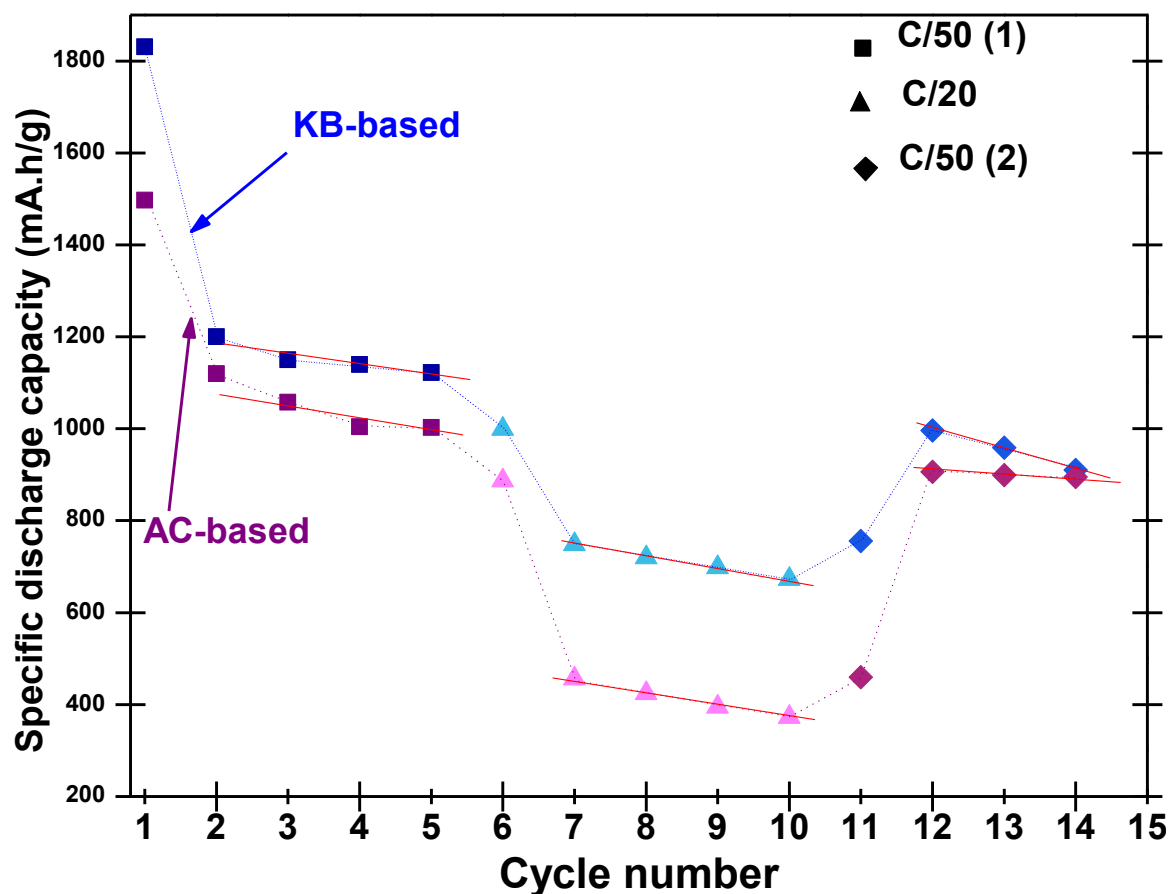


Figure 50: Specific discharge capacity in function of cycle number at different cycling rates for the KB-based cell and the AC-based cell.

Further studies and cycling are needed to really determine which carbon is best for battery application. The XRD, BET and TGA data tend to show that more intimate contact is achieved within the AC-based cathode, due to its higher surface area. However, the electrochemical data of the all-solid-state cells using both cathodes show that at high rates, the most conductive carbon (KB) results in smaller capacity loss. The cycling parameters were not the same and the two cells were run months from each other, but as cycling a battery takes several weeks, we are currently not able to produce two identical cells to get more conclusive results.

4.3.2.2 Comparison of two ionic conductors: LGPS and $\text{Li}_{1.5}\text{PS}_{3.25}$

In this section, two ionic conductors in the composite cathode are compared. **Table 9** below summarizes the important properties of the solid electrolytes $\text{Li}_{1.5}\text{PS}_{3.25}$ and LGPS.

Solid electrolyte	Ionic conductivity (S/cm)	Structure
$\text{Li}_{1.5}\text{PS}_{3.25}$	10^{-5}	Amorphous structure
LGPS	6×10^{-3}	Crystal

Table 9: Ionic conductivities of $\text{Li}_{1.5}\text{PS}_{3.25}$ and LGPS.

Figure 51 shows the XRD patterns of $\text{AC/S/Li}_{1.5}\text{PS}_{3.25}$ and $\text{AC/S/Li}_{10}\text{GeP}_2\text{S}_{12}$ composite cathodes. The $\text{Li}_{1.5}\text{PS}_{3.25}$ -based composite is completely amorphous whereas the pattern of the LGPS-based cathode has a few small unknown peaks, which do not correspond to LGPS nor sulfur.

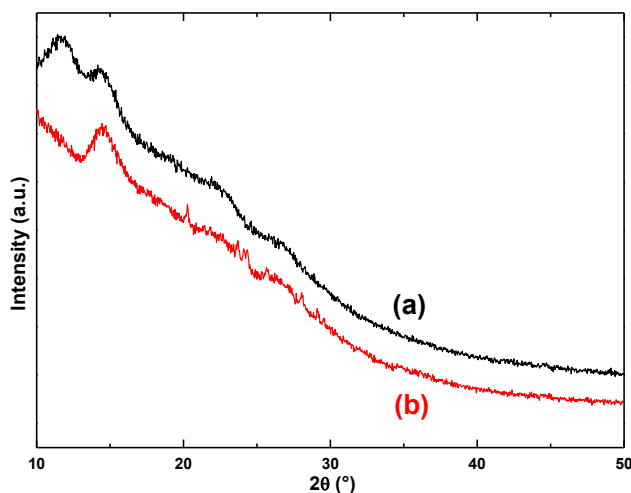


Figure 51: XRD patterns of $\text{AC/S/Li}_{1.5}\text{PS}_{3.25}$ and $\text{AC/S/Li}_{10}\text{GeP}_2\text{S}_{12}$ composite cathodes.

Two all-solid-state batteries were assembled using LGPS as the solid electrolyte, Li-In as the anode, and $\text{AC/S/Li}_{1.5}\text{PS}_{3.25}$ (a) or $\text{AC/S/Li}_{10}\text{GeP}_2\text{S}_{12}$ (b) as the cathode. The cells were cycled galvanostatically at C/50 for 5 cycles, then at C/20 for 5 cycles, and at C/50 again, in the voltage window [0.5 V – 3.5 V] against Li-In. The charge-discharge curves of both cells are presented in **Figure 52**. The cell using LGPS as the ionic conductor in the composite cathode exhibits an initial discharge capacity of 1200 mA.h/g, which then drops to 400 mA.h/g (by 33%). Upon cycling at C/50, the capacity decreases quickly, from 870 to 720 mA.h/g in 4 cycles (decay rate of 37.5 mA.h/g per cycle). Overall the performance of the LGPS-based cell is poorer than the $\text{Li}_{1.5}\text{PS}_{3.25}$ -based cell. This can be explained by the difference in ductility of both ionic conductors. $\text{Li}_{1.5}\text{PS}_{3.25}$ is amorphous and acts as a binder, which allows for a better solid-solid contact within the cathode. LGPS is a crystalline phase and thus, it is less likely to bind as well as $\text{Li}_{1.5}\text{PS}_{3.25}$ upon volume changes, hence poorer capacity despite its significantly higher conductivity. Interestingly, at higher rates (C/20),

performance of the $\text{Li}_{1,5}\text{PS}_{3,25}$ -based cell is much poorer than the LGPS-based cell performance, relatively to performance at C/50.

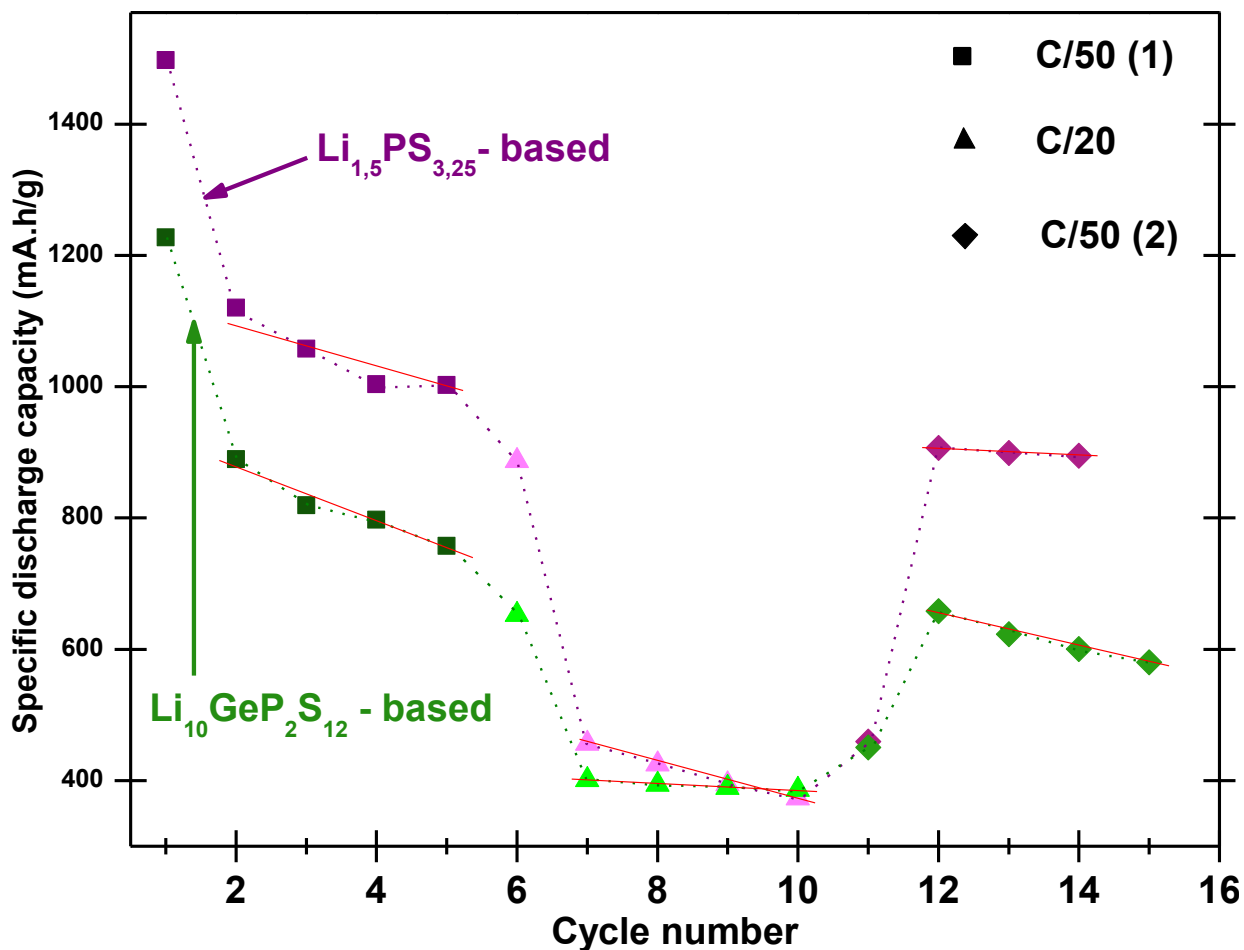


Figure 52: Charge-discharge curves of cells prepared with (a) $\text{Li}_{1,5}\text{PS}_{3,25}$ -based and (b) LGPS-based cathodes.

4.4 Conclusion and perspective

In this chapter, cycling measurements of our first all-solid-state batteries are presented. This provides insight on the performance of our old and new sulfide-based ionic conductors as solid electrolytes, besides just crystallinity and ionic conductivity characterizations.

First, two of the most promising solid electrolytes were compared. The $\text{Li}_7\text{P}_3\text{S}_{11}$ -based cell showed relatively good stability but a low capacity of about 500 mA.h/g after 10 cycles, and the

$\text{Li}_{10}\text{GeP}_2\text{S}_{12}$ -based cell exhibited extra-added capacity (1850 mAh/g for the initial discharge) owing to secondary irreversible reactions which lead to faster decay of capacity.

Then two carbons were used in the composite cathode and compared. For favorable solid/solid contact and cycling at low rates, it seems that surface area is the key to obtain good performance. However, for a high rate capability (cycling at very different rates for short times), higher electronic conductivity of the cathode is required in order to favor fast transfer of charges at the interfaces between active material and electrons and ions. That is why Activated Carbon (AC) (very high surface area, low electronic conductivity) demonstrated good performance in the first cycles at C/50, but poor rate capability. Ketjenblack (KB) (high surface area but not as high as AC, very good electronic conductivity) showed faster decay at low rates initially, but recovered capacities much better upon rate change. The optimal conductive host would be a combination of both carbons in appropriate ratios.

Finally two solid ionic conductors were compared for use in the composite cathode. Amorphous and ductile $\text{Li}_{1.5}\text{PS}_{3.25}$ showed better performance and capacity than crystalline $\text{Li}_{10}\text{GeP}_2\text{S}_{12}$ at low rates, due to better contact and coating of the sulfur, and reduction of grain boundary resistance within the cathode. However, there again, at high rates and high rate change, the $\text{Li}_{1.5}\text{PS}_{3.25}$ -based cell exhibited very fast decay due to the very low ionic conductivity of $\text{Li}_{1.5}\text{PS}_{3.25}$ and to the consequently low transfer of charges in the cathode compared with the LGPS-based cell.

In conclusion, for further tests and studies to characterize our materials, a distinction should be made in the type of cell performance: the performance of cells cycled at constant low rates and the performance of cells cycled at high rates and alternatively high and low rates.

Further investigation and optimization need to be done, in particular for physical processes and methods to form favorable interfaces in the composite cathode at low and high rates. Solubility experiments were carried out aiming at the development of thin membranes to improve contact between electrolyte layer and electrodes. These solubility results could also be used for a better and uniform coating of sulfur particles by solid electrolyte and electronic conductor in the cathode.

Lastly, the engineering aspect of all-solid-state batteries need to be further developed. First, batteries need to be cycled in a 100% air-free environment. Study of the influence of variable applied pressure on the performance of the cell could be carried out with a new design. The use of a hot press,

or a ball milling instrument equipped with a heater and a cooler could be extremely useful to fabricate high-quality interfaces in the materials as well.

References

-
- ¹ Goodenough J.B., Kim Y., Challenges for rechargeable Li batteries, *Chem Mater.*, **2010**, 22, 587-603.
- ² Goodenough, J.B., and Park, K-S., The Li-Ion Rechargeable Battery: A Perspective. *J. Am. Chem. Soc.*, **2013**, 135, 1167-1176.
- ³ Tarascon, J-M., Armand, M., Issues and Challenges Facing Rechargeable Lithium Batteries, *Nature*, **2001**, 414, 359-367.
- ⁴ Manthiram, A., Fu, Y., Chung, S-H., Zu, C., and Su Y-S., Rechargeable Lithium-Sulfur Batteries, *Chem. Rev.*, **2014**, 114, 11751.
- ⁵ Mizushima, K., Jones, P.C., Wiseman, P.J., and Goodenough, J.B., Li_xCoO_2 : A New Cathode Material for Batteries of High Energy Density, *Mat. Res. Bull.*, **1980**, 15, 783.
- ⁶ Bruce, P.G., Freunberger, S.A., Hardwick, L.J., and Tarascon, J-M., Li-O₂ and Li-S Batteries with High Energy Storage, *Nature Mater.*, **2012**, 11, 19.
- ⁷ Wang, D-W., Zhou, G., Li, F., Wu, K-H., Lu, G., Cheng, H-M., and Gentle, I., A Durable Cathode with Sub-Nanometer Confined Sulfur for High Energy Batteries, *Angew.*, DOI: 10.1002/anie.200, **2013**.
- ⁸ Knoxville, T.; Dean, J.; McGraw-Hill, New York: **1999**.
- ⁹ Guo, J., Yang, Z., Yu, Y., Abruna, H., and Archer, L., Lithium-Sulfur Battery Cathode Enabled by Lithium-Nitrile Interaction, *J. Am. Chem. Soc.*, **2013**, 135, 763.
- ¹⁰ J. Davison, J. Boyce, Chemical Engineering, Worcester Polytechnic Institute, Worcester, **2012**, p. 126.
- ¹¹ Gray F., Smith M., Secondary batteries - lithium rechargeable systems - Lithium polymer batteries, *Encyclopedia of Electrochemical Power Sources*, Elsevier, Amsterdam, **2009**, 169-176.
- ¹² Vincent C., Lithium batteries: a 50-year perspective, 1959-2009, *Solid State Ionics*, **2000**, 134, 159-167.
- ¹³ Takada K., Inada T., Kajiyama A., Kouguchi M., Sasaki H., Kondo S., Michiue Y., Nakano S., Tabuchi M., Watanabe M., Solid state batteries with sulfide-based solid electrolytes, *Solid State Ionics*, **2004**, 172, 25-30.

-
- ¹⁴ Whittingham M., Lithium Batteries and Cathode Materials, *Chem. Rev.*, **2004**, 104, 4271-4301.
- ¹⁵ Fergus J., Recent developments in cathode materials for lithium ion batteries, *J. Power Sources*, **2010**, 195, 939-954.
- ¹⁶ Thangadurai V., Weppner W., Recent progress in solid oxide and lithium ion conducting electrolytes research, *Ionics*, **2006**, 12, 81-92.
- ¹⁷ Ito M., Inaguma Y., Jung W.H., Chen L., and Nakamura T., High lithium ion conductivity in the perovskite-type compounds $\text{Ln}_{1/2}\text{Li}_{1/2}\text{TiO}_3$ (Ln = La, Pr, Nd, Sm), *Solid State Ionics*, **1994**, 70/71, 203–207.
- ¹⁸ Aono H., Sugimono E., Sadaoka Y., Imanaka N., and Adachi G., Ionic conductivity of solid electrolytes based on lithium titanium phosphate, *J. Electrochem. Soc.*, **1990**, 137, 1023–1027.
- ¹⁹ Hong, H. Y.-P., Crystal structure and ionic conductivity of $\text{Li}_{14}\text{Zn}(\text{GeO}_4)_4$ and other new Li^+ superionic conductors., *Mater. Res. Bull.*, **1978**, 13, 117–124.
- ²⁰ Murayama M., Irie M., Ito S., Hata T., Sonoyama N., Kawamoto Y., Kanno R., Synthesis of new lithium ionic conductor thio-LISICON-Lithium silicon sulfides systems, *Journal of Solid State Chemistry*, **2002**, 168, 140-148.
- ²¹ Kanno R., and Murayama M., Lithium ionic conductor thio-LISICON: the $\text{Li}_2\text{S-GeS}_2\text{-P}_2\text{O}_5$, *J. Electrochem. Soc.*, **2001**, 1148, A742-A746.
- ²² Murugan R., Thangadurai V., and Weppner W., Fast lithium ion conduction in garnet-type $\text{Li}_7\text{La}_3\text{Zr}_2\text{O}_{12}$, *Angew. Chem. Int. Ed.*, **2007**, 46, 7778-7781.
- ²³ Fu J., Superionic conductivity of glass-ceramics in the system $\text{Li}_2\text{O-Al}_2\text{O}_3\text{-GeO}_2\text{-P}_2\text{O}_5$, *Solid State Ionics*, **1997**, 96, 195-200.
- ²⁴ Fu J., Fast Li^+ ion conducting glass-ceramics in the system $\text{Li}_2\text{O-Al}_2\text{O}_3\text{-GeO}_2\text{-P}_2\text{O}_5$, *Solid State Ionics*, **1997**, 104, 191-194.
- ²⁵ Seino Y., Ota T., Jyunke T., and Yanagi K., Extended Abstracts of the 36th Symposium on Solid State Ionics in Japan, **2010**, 116-117.
- ²⁶ K. Kanehori, K. Matsumoto, K. Miyauchi and T. Kudo, Thin film solid electrolyte and its application to secondary lithium cell, *Solid State Ionics*, **1983**, 9/10, 1445-1448.
- ²⁷ Inaguma Y., Chen LQ., Itoh M., Nakamura T., Candidate compounds with perovskite structure for high lithium ionic conductivity, *Solid State Ionics*, **1994**, 70, 196-202.
- ²⁸ Ito M., Inaguma Y., Jung W.H., Chen L., Nakamura T., *Solid State Ionics*, **1994**, 70-71, 203–207

-
- ²⁹ Aono H., Sugimono E., Sadaoka Y., Imanaka N., Adachi G., *J. Electrochem. Soc.*, **1990**, 137, 1023–1027
- ³⁰ Aono H., Sugimoto E., Sadaoka Y., Imanaka N., Adachi G., Ionic conductivity and sinterability of lithium titanium phosphate system, *Solid state Ionics*, **1990**, 40, 38–42.
- ³¹ Kamaya N., Homma K., Yamakawa Y., Hirayama M., Kanno R., Yonemura M., Kamiyama T., Kato Y., Hama S., Kawamoto K., Matsui A., *Nat. Mater.*, **2011**, 10, 682–686
- ³² Murugan R., Thangadural V., Weppner W., *Angew. Chem. Int. Ed.*, **2007**, 46, 7778–7781.
- ³³ Matsui M., Takahashi K., Sakamoto K., Hirano A., Takeda Y., Yamamoto O., Imanishi N., Phase stability of a garnet-type lithium ion conductor $\text{Li}_7\text{La}_3\text{Zr}_2\text{O}_{12}$, *Dalton Transactions*, **2014**, 43, 1019–1024.
- ³⁴ Yu X., Bates J.B., Jellison G.E., Hart F.X., A stable thin-film lithium electrolyte: Lithium phosphorus oxynitride, *J. Electrochem. Soc.*, **1997**, 144, 524–532.
- ³⁵ Julien C., Nazri G.A., *Solid State Batteries: Materials Design and Optimization*, Kluwer Academic Publishers, Boston, **1994**.
- ³⁶ Zhang Z., Kennedy J.H., Synthesis and characterization of the $\text{B}_2\text{S}_3\text{-Li}_2\text{S}$, the $\text{P}_2\text{S}_5\text{-Li}_2\text{S}$ and the $\text{B}_2\text{S}_3\text{-P}_2\text{S}_5\text{-Li}_2\text{S}$ glass systems, *Solid State Ionics*, **1990**, 38, 217–224.
- ³⁷ Ohtomo T., Hayashi A., Tatsumisago M., Kawamoto K., All-solid-state batteries with $\text{Li}_2\text{O-Li}_2\text{S-P}_2\text{S}_5$ glass electrolytes synthesized by two-step mechanical milling, *Journal of solid state electrochemistry*, **2013**, 17, 2551–2557.
- ³⁸ Wada H., Menetrier M., Levasseur A., Hagenmuller P., Preparation and ionic conductivity of new $\text{B}_2\text{S}_3\text{-Li}_2\text{S-LiI}$ glasses. *Mater. Res. Bull.*, **1983**, 18, 189–193
- ³⁹ Yamauchi A., Sakuda A., Hayashi A. and Tatsumisago M., Preparation and ionic conductivities of $(100 - x)(0.75\text{Li}_2\text{S} \cdot 0.25\text{P}_2\text{S}_5) \cdot x\text{LiBH}_4$ glass electrolytes, *J. Power Sources*, doi:10.1016/j.jpowsour, **2012**.
- ⁴⁰ Aotani N., Iwamoto K., Takada K., Kondo S., Synthesis and electrochemical properties of lithium ion conductive glass, $\text{Li}_3\text{PO}_4\text{-Li}_2\text{S-SiS}_2$, *Solid State Ionics*, **1994**, 68, 35–39.
- ⁴¹ Mizuno F., Hayashi A., Tadanaga K., Tatsumisago M., High lithium ion conducting glass-ceramics in the system $\text{Li}_2\text{S-P}_2\text{S}_5$, *Solid State Ionics*, **2006**, 177, 2721–2725.
- ⁴² Mizuno F., Hayashi A., Tadanaga K., Tatsumisago M., New, highly ion-conductive crystals precipitated from $\text{Li}_2\text{S-P}_2\text{S}_5$ glasses, *Adv. Mater.*, **2005**, 17, 918–92.

-
- ⁴³ Ohtomo T., Hayashi A., Tatsumisago M. and Kawamoto K., Characteristics of the $\text{Li}_2\text{O-Li}_2\text{S-P}_2\text{S}_5$ glasses synthesized by the two-step mechanical milling, *J. Non-Cryst. Solids*, **2013**, 364, 57–61.
- ⁴⁴ Chiku M. et al., *Electrochemistry*, **2012**, 80, 740.
- ⁴⁵ Iwamoto K., Aotani N., Takada K., Kondo S., Rechargeable solid state battery with lithium conductive glass, $\text{Li}_3\text{PO}_4\text{-Li}_2\text{S-SiS}_2$, *Solid State Ionics*, **1994**, 70/71, 658–661.
- ⁴⁶ Minami K., Hayashi A., Ujiie S., Tatsumisago M., Electrical and electrochemical properties of glass–ceramic electrolytes in the systems $\text{Li}_2\text{S-P}_2\text{S}_5\text{-P}_2\text{S}_3$ and $\text{Li}_2\text{S-P}_2\text{S}_5\text{-P}_2\text{O}_5$, *Solid State Ionics*, **2011**, 192, 122–125.
- ⁴⁷ Tatsumisago M., Nagao M., Hayashi A., Recent development of sulfide solid electrolytes and interfacial modification for all-solid-state rechargeable lithium batteries, *Journal of Asian ceramic societies*, **2013**, 1, 17-25.
- ⁴⁸ Nagao M., Hayashi A., Tatsumisago M., Sulfur–carbon composite electrode ... rechargeable lithium batteries, *J. Mater. Chem.*, **2012**, 22, 10015–10020.
- ⁴⁹ Sakuda A., Hayashi A., Ohtomo T., Hama S., Tatsumisago M., All-solid-state lithium secondary batteries using LiCoO_2 particles with pulsed laser deposition coatings of $\text{Li}_2\text{S-P}_2\text{S}_5$ solid electrolytes, *J. Power Sources*, **2011**, 196, 6735–6741.
- ⁵⁰ Nagao M., Hayashi A., Tatsumisago M., Electrochemical performance of all-solid-state Li/S batteries with sulfur-based composite electrodes prepared by mechanical milling at high temperature, *Energy Technology*, **2013**, 1, 196-192.
- ⁵¹ M. Nagao, A. Hayashi, M. Tatsumisago, Bulk-type lithium metal secondary battery with indium thin layer at interface between Li electrode and $\text{Li}_2\text{S-P}_2\text{S}_5$ solid electrolyte, *Electrochemistry*, **2012**, 80, 734–736.
- ⁵² M. R. G. Mendez, Effect of hot pressing temperature on the electrochemical stability Of $\text{Li}_2\text{S-P}_2\text{S}_5$ (75 – 25 % mole) as a solid electrolyte, MASC's Thesis, Michigan State University, **2015**.
- ⁵³ Sakuda S., Hayashi A., Tatsumisago M., Sulfide solid electrolyte with favorable mechanical property for all-solid-state lithium battery, *Scientific reports*, **2013**, 3, 226.

-
- ⁵⁴ Minami K., Hayashi A., Tatsumisago M., Preparation and characterization of superionic conducting $\text{Li}_7\text{P}_3\text{S}_{11}$ crystal from glassy liquids, *Journal of the Ceramic Society of Japan*, **2010**, 4, 305-308.
- ⁵⁵ Seino Y., Ota T., Takada K., Hayashi A., Tatsumisago M., A sulphide lithium super ion conductor is superior to liquid ion conductors for use in rechargeable batteries, *Energy Environ. Sci.*, **2014**, 7, 627.
- ⁵⁶ Huang B., Yao X., Huang Z., Guan Y., Jin Y., Xu X., Li_3PO_4 -doped $\text{Li}_7\text{P}_3\text{S}_{11}$ glass-ceramic electrolytes with enhanced lithium ion conductivities and application in all-solid-state-batteries, *Journal of Power Sources*, **2015**, 284, 206-211.
- ⁵⁷ Eom M., Kim J., Noh S., Shin D., Crystallization kinetics of $\text{Li}_2\text{S-P}_2\text{S}_5$ solid electrolyte and its effect on electrochemical performance, *Journal of Power Sources*, **2015**, 284, 44-48.
- ⁵⁸ Ranasinghe K., Ray C., Day D., A generalized method for determining the crystal nucleation and growth rates in glasses by thermal differential analysis, *Journal of Materials Science*, **2002**, 37, 547-555.
- ⁵⁹ Minami K., Mizuno F., Hayashi A., Lithium ion conductivity of the $\text{Li}_2\text{S-P}_2\text{S}_5$ glass-based electrolytes prepared by the melt quenching method, *Solid state ionics*, **2007**, 178, 837-841.
- ⁶⁰ Toffoli P., Khodadad P., *Comptes Rendus De L'Académie Des Sciences*, **1982**, 294, 87-90.
- ⁶¹ Hayashi A., Noi K., Sakuda A., Tatsumisago M., Superionic glass-ceramic electrolytes for room-temperature rechargeable sodium batteries, *Nature Communications*, **2012**, 3.
- ⁶² Kousuke Noi, Akitoshi Hayashi, Masahiro Tatsumisago, *Journal of Power Sciences*, **2014**, 269, 260-265.
- ⁶³ Menzel, F., Ohse, L. and Brockner, W., Vibration spectrum and normal coordinate analysis of the pyrothiophosphates $\text{Na}_4\text{P}_2\text{S}_7$, $\text{Na}_2\text{FeP}_2\text{S}_7$, and $\text{Ag}_4\text{P}_2\text{S}_7$. *Heteroatom Chem.*, **1990**, 1: 357–362.
- ⁶⁴ Takada K., Aotani N., Iwamoto K., Kondo S., *Solid State Ionics*, **1996**, 86, 877-882.
- ⁶⁵ Nagata H., Chikusa Y., Activation of sulfur active material in all-solid-state lithium-sulfur battery, *Journal of Power Sources*, **2014**, 263, 141-144.